Temperature-dependent Current-Voltage Characteristic of GaAsBi/GaAs Multiple Quantum Wells for Solar Cell Applications

By: Mohamad Riduwan MD Nawawi

Supervisor: Professor John PR David

A thesis submitted for the degree of Doctor of Philosophy

Semiconductor Materials and Devices Group Department of Electronic and Electrical Engineering The University of Sheffield

December 2022

Acknowledgements

In the name of Allah, "*Alhamdullilah*", I am most grateful to Allah, The Most Gracious and Most Merciful, for making this happen.

My sincerest gratitude to my supervisor, Professor Dr. John PR David, for his invaluable guidance during my research studies. I learn a lot from him, which will be very useful for my future. Thanks for understanding and patience in helping me face a lot of trouble during my studies.

A special thanks also to my co-supervisor Dr. Robert D Richards, for his unlimited support, motivation and encouragement along the way of my PhD studies. The MBE will always be in my best memory and the *game night* is super awesome.

I am most indebted to my beloved parents, *Mak* and *Abah*, who pour me with their priceless *doa* and advice. I am also grateful to my lovely wife *Sayang* for her patience, inspiration and endless love together on this journey. Without you, I may not be here, and I am still surviving because of you. To my *dukes*, *Ahmad* and *Ajin*, you are the best gift from Him to me. I love you so much, and thanks for keep cheering, *daddy*.

I am also grateful to the Islamic Development Bank (IDB) for granting me the scholarship and allowing me to explore the new world. Many thanks to my employer Universiti Teknikal Malaysia Melaka, for upholding my carrier and accepting me to become successful.

Last but not least special persona who constantly be part of this journey: *Musa, Aimie, Zamani, Kak Aishah, Rusdy, Fiza, Zul, Eddie, Huda, Nazim, Rohaida, Abe Sol, Kak Kira, Nick, Yu Chen, Faezah, Tom, Nada* and my entire friend in The University of Sheffield for the help and always be supportive of me. Your kindness is highly appreciated, and I highly honor having a friend like all of you.

Abstract

GaAsBi has the potential to become a 1eV solar cell for the multi-junction solar cell application. GaAsBi possessed a large band gap bowing coefficient in GaAs material. It reduces the band gap's energy by 70-90 meV per unit strain for each 1% incorporation of Bismuth (Bi) into the GaAs material and produces good electron mobility properties. Research has shown its capability to extend the absorption edge above 1000 nm, higher than InGaAs junction solar cell. The previous study mostly reported the characteristic of GaAsBi p-i-n at room temperature. However, the practical operating temperature of the solar cell during sunlight is more than 60°C. The solar cell temperatures are getting hotter as the devices are operated under concentrated sunlight. Therefore, the investigation of temperature-dependent properties for GaAsBi will contribute to providing the characteristic performance of GaAsBi solar cells at high temperatures.

The study comprises three main parts. Firstly, is to investigate the dark current performance of the GaAsBi in bulk and multiple quantum well structure devices. The dark current is important to verify the conventional current diode behaviour and quality of the growth devices. Growing the GaAsBi at optimum growth temperature is important to obtain good solar cell performance. Besides, MQW devices perform lower dark currents than bulk series devices. The second observation is to model and estimate the MQW GaAsBi under a monochromatic light source. Based on photocurrent measurement at different temperatures, several mathematical processes are conducted to produce solar cell parameters at different temperatures. The devices were also tested under a solar simulator to observe the overall performance. The third outcome is to study the carrier trapping thermal escape time of the hole carrier under the illumination of light bias at a lower temperature. The hole carrier has a longer thermal escape time than the electron carrier due to the increment of the valance band for bandgap reduction.

The results suggest many opportunities to improve the performance of GaAsBi multiple quantum. Obtaining optimum performance of GaAsBi at high temperatures, especially under solar contractor application, requires several areas of improvement, such as the growth process, number of optimum quantum well and temperature effect. GaAsBi can become a potential 1eV junction solar cell in future.

Table of contents

List of Figures

List of Tables

List of Symbols

TWh - Terawatt hour
CO_2 – Carbon Dioxide
SO_2 – Sulfur Dioxide
K- Kelvin
a_{ABC}- Lattice constant of the ternary alloy
E_{ABC}- Energy band gap of ternary alloy
E_{AC}- Band gap of compound material
E_{BC}- Band gap of host material
$E_v(GaAs)$- Energy of the valence band maximum (VBM) for GaAs
$E_g(GaAs)$ - energy band gap of GaAs is approximately 1.42 eV
h- Plank constant
k- Momentum
m^*- Effective mass of hole
$E_\pm(GaAsBi)$ - Eenergy of sub-bands split in the valence band
$E_v(GaAs)$ - Energy of the valence band maximum (VBM) for GaAs
x- bismide concentration (from 0 to 1)
F- Magnitude of misfit
$a_o(s)$- Lattice constant of substrate
$a_o(f)$- Relaxed lattice constant of the desired film material
e- Electron
I_{ph}- Current source solar cell
R_s- Series resistance in solar cell
R_{sh}- Shunt resistance in solar cell
q- Electron charge
k- Boltzmann constant
T- Temperature
n- Ideality factor
I_{MP}- Maximum point current
V_{MP}- Maximum point voltage
I_{SC}- Current short circuit
V_{OC}- voltage open circiot
FF- Fill factor

List of Abbreviations

AlAs - Aluminium Arsenide
AM – Air Mass
As - Arsenic
BAC - Band Anti Crossing
Bi - Bismuth
CBA- Conduction Band Minimum
CBM - Conduction Band Minima
Cd- Cadmium
CdTe - Cadmium Telluride
CIGS - Copper Indium Gallium Selenide
GaAs - Gallium Arsenide
GaAsBi - Gallium Arsenide Bismuth
GaAsN - Gallium Arsenide Nitride
GaAsP - Gallium Arsenide Phosphide
GaInP - Gallium Indium Phosphide
InGaAs - Indium Gallium Arsenide
InGaAsP - Indium Gallium Arsenide Phosphide
InGaP - Indium Gallium Phosphide
InSb - Indium Antimonide
ISO - International Organization for Standardization
IVBA - inter-valence band absorption
LED - Light Emitting Diodes
MBE - Molecular Beam Epitaxial
MQW – Multi Quantum Well
NREL - National Renewable Energy Laboratory
Pb - Lead
PV – Photovoltaic
QW - Quantum Well
RE - Renewable energy
RHEED - Reflection High Energy Electron Diffraction
Sb - Antimony
Te - Telluride
UNFCCC - United Nation Framework Convention on Climate Change
VBAC - Valence Band Anti Crossing
VBM - Valence Band Maximum
VCA -Virtual Crystal Approximation

List of Publications

Journal Papers

R.D. Richards, T.B.O. Rockett, **M.R.M Nawawi**, F. Harun, et al, "Light-biased IV characteristics of a GaAsBi/GaAs multiple quantum well pin diode at low temperature", Semiconductor Science Technology, Vol.33 (2018) 094008, IOP Publishing, doi: 10.1088/1361-6641/aad72a

R.D. Richards, F. Harun, **M.R.M Nawawi,** Liu Y., et al, "Temperature and bandgap dependence of GaAsBi p-i-n diode current-voltage behavior", Journal of physics. D, Applied physics, Vol.54(19) (2021) p.195102, IOP Publishing, doi: 10.1088/1361-6463/abe4ff

Oral and poster Presentations

Chapter 1

Introduction

1.0 Introduction

The demand for global electricity consumption increases rapidly by 2.1% per year. Based on the World Energy Outlook 2019, the world electricity demand recorded in 2018 was 23,031 TWh. It is projected to rise by almost 36,562 TWh in total usage by 2040 [1]. Several factors, such as the rapid expansion of industrialization and economic growth [2-5], the upsurge in population [6] and the effect of urbanization [7-8], have raised the energy demand every year.

As a result, a great burning of coal, fossil fuel, and natural gas is required to fulfil electricity generation. Almost 61% of electricity generation is from coal and natural gas, followed by 26% and 11% from renewable energy and nuclear power, respectively [1]. This scenario leads to environmental impact issues such as global warming and climate change. It is because harvesting energy from coal, gas and fossil fuel has become the main factor contributing to high greenhouse gas emissions such as carbon dioxide (CO_2) and sulphur dioxide (SO_2). For instance, energy from coal-related sources accounts for about 40% of sulphur dioxide emissions, which causes respiratory illness, and it is the primary substance in acid rain [1]. Moreover, these resources are limited and non-renewable.

Many efforts are being undertaken across the globe to reduce carbon dioxide emissions. In the Paris Agreement declaration under the United Nations Framework Convention on Climate Change (UNFCCC), 196 countries have committed to combat global greenhouse emissions by agreeing to ensure average global temperature escalation below 2 degrees centigrade [9]. Hence, numerous activities such as the establishment of energy policy [10-12], implementation of green technology [13-14] and development of renewable energy to reduce the global warming effect [15]. In the current stated policy scenario, renewable energy contribution is projected to grow from 26% in 2018 to 44% in 2040 [1].

Renewable energy (RE) is a clean energy generation to accommodate the demand for electric power and contribute to lowering the impact of greenhouse gas emissions. The RE converts energy from endless sources, such as the sun, wind, biomass, and hydro, to electrical energy for domestic and industrial usage [16]. Solar energy has drawn much interest between researchers and industry. Earth receives tremendous sunlight at about 85,000 TW [17], and its energy is limitless. According to the International Energy Report 2019, world electricity from solar energy will dominate about 35% among other renewable energy resources in 2050. It is higher than wind and hydroelectric generation [1]. Nowadays, numerous studies related to solar energy is being conducted, for instance, developing efficient solar cell [18], controlling the solar panel mechanism [19], electrical solar power system [20], energy storage module [21] and reducing solar energy losses [22]. However, the main challenge in harvesting higher solar energy is how the solar cell can maximally absorb as many spectrums of energy from solar irradiance and convert it to electrical power.

1.1 Solar Energy

Solar energy means energy from the sun. Earth receives a vast amount of solar energy every day. Using science and technology enables us to utilize this energy by converting it into electricity. The expected electric power generated from sunlight is about 85,000 TWh yearly [17]. Although on a cloudy day, some solar power can still be produced. Solar energy is a pollution-free and cheap source of energy. It does not produce harmful greenhouse gas effects such as carbon dioxide and methane [23]. Hence, solar power offers limitless energy capable of producing electricity without damaging the environment and is also available for a whole year.

The earth receives the sun’s energy in the form of sunlight. The sunlight propagates as a waveform, which is comprised of the amount of energy and wavelength. As the sunlight reaches the earth's atmosphere, it is attenuated because the gas particle, water vapours and dust particles in the atmosphere absorb some of the solar energy. All the sun’s energy arrives on the earth, described as a solar electromagnetic radiation spectrum. It is measured in power per unit area and is known as solar irradiance. The one-meter square area of the earth's atmosphere receives 1.4 KW/m^2 of energy.

In addition, the incident of sunlight spectrum entering the Earth involves a parameter named air mass (AM). Air Mass refers to the path length of the sunlight that travels through the Earth's atmosphere to reach the ground relative to the path length of the sun directly overhead. Figure 1.1 indicates the air mass condition for sunlight's direction travels to Earth [15]. Two distances can be measured when observing a solar cell on the ground. The first distance, "y", is the direct overhead or perpendicular distance from the sun to the Earth. The second distance, denoted as "h" is the length from the sun to the observation point. In this case, the angle between "h" and "y" is called theta. This creates a right triangle shape where the cosine of theta equals y over h. AM is defined as one over cosine theta.

$$\theta = \cos^{-1}(\frac{y}{h})$$

$$AM = \frac{1}{\cos\theta}$$

Solar spectra are measured at different air masses, representing the distance light must travel and attenuate as it passes through the atmosphere before reaching a solar panel. Hence, there are three classifications of air mass: AM0, AM1.0, and AM1.5. AM0 represents the absence of attenuation for sunlight travel outside the atmosphere. The AM1.0 is when the sun is directly overhead. Thus, the standard sunlight spectrum used to test solar cell performance is based on an air mass of 1.5, which represents typical sunny conditions when solar irradiance reaches the Earth's surface. At an air mass of 1.5 and an angle of 48.2°, the irradiance is approximately 1000 W/m2, which is closer to real-life conditions. This makes AM 1.5 the preferred standard spectrum for measuring solar cell efficiency. AM coefficient helps to portray the solar spectrum after the sunlight has travelled through the atmosphere. Figure 1.2 illustrates the standard solar spectra at AM0 for extra-terrestrial spectrum and AM1.5 for terrestrial use.

$$for\ \theta = 48.2°$$

$$AM\ 1.5 = \frac{1}{\cos 48.2°}$$

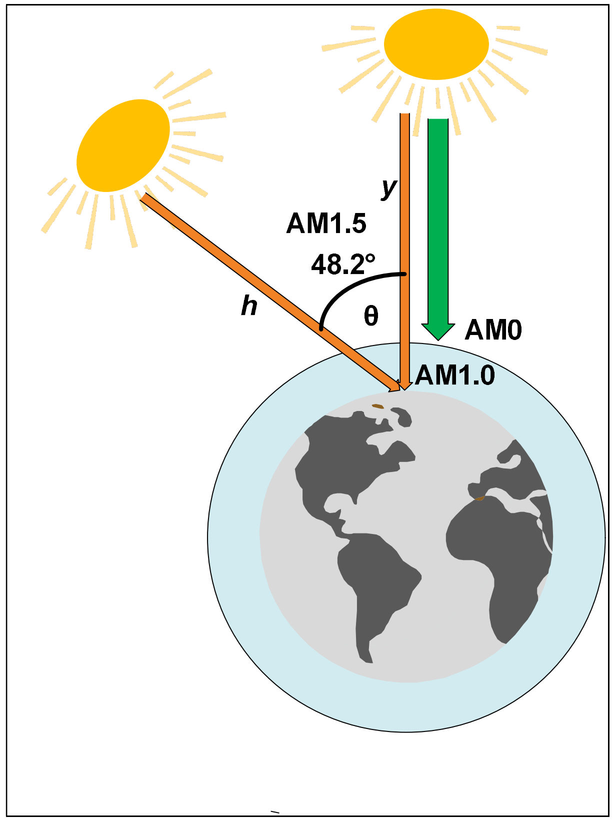

Figure 1.1: Sunlight radiation and Air Mass (AM)

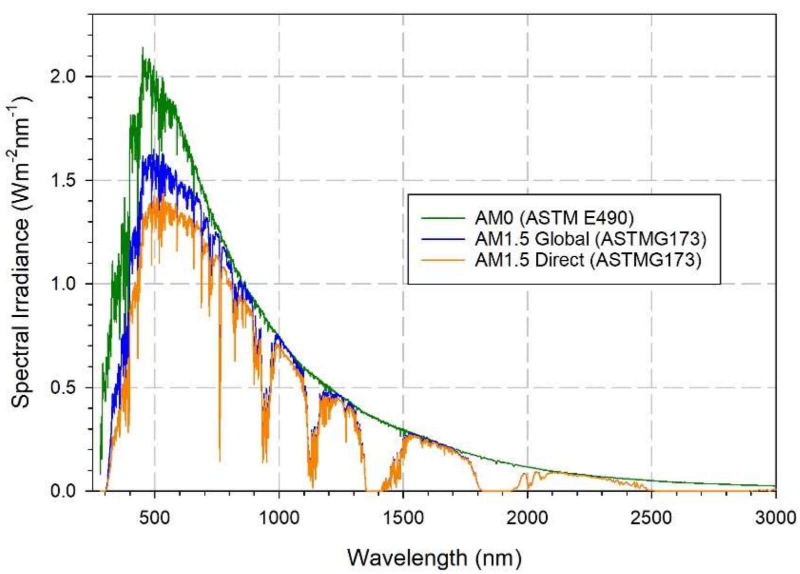

Figure 1.2: ASM G-173-03 Reference Spectra (International standard ISO 9845-1, 1992)

Even though solar energy is eco-friendly and an alternative to conventional resources, it has several limitations. First, it requires high cost, especially for solar material development, manufacturing photovoltaic cell devices and installing the solar power harvesting system. Second, to generate more energy, installing solar panels requires a large space area. Furthermore, it also costs a colossal power storage capacity, such as the battery banks, to save energy. Moreover, power generation depends on the season, weather, and geographic location to harvest adequate solar energy for electric power generation. For instance, during winter months and also in cloudy produce little power. Despite all the drawbacks of solar energy, it is still a promising alternative renewable energy source to compensate for the rise of electrical power demand and is pollution-free for the environment.

1.2 Solar cell

Energy from the sun is converted into electrical energy through the application of semiconductor devices known as a solar cells. It is also called a photovoltaic cell [16]. The solar cell structure is developed by the N-type and P-type semiconductor layers. When both layers are joined together, it forms a P-N junction. It converts solar or light energy into electrical energy by applying the photovoltaic effect.

The Photovoltaic effect generates voltage and electric current through a material upon exposure to sunlight. When the semiconductor material absorbs sufficient light energy, it will cause the excitation of electron carriers to a higher-energy state and leave a hole in the valence band. The electric field within the depletion region will separate the collection of light-generated carriers to the side of the P-N junction. The electrons will move to the N-type side and hole into the P-type side of the junction. Connecting a wire between the N-type junction to the P-type junction creates a pathway for the electrons to move towards the holes. The flow of electrons is known as electrical current. This principle is used by solar cells to produce electricity.

One solar cell enables the production of several watts of power. Many solar cells are wired together to make a solar panel. Thus, several solar panels are needed to generate enough electricity to power a household's energy consumption. This alternative mechanism is a feasible approach to convert the sun's irradiance directly into electricity. Advancement in solar technologies provides a solution to power human lives from the sun with less dependent on fossil resources. The main goal of solar cell technology is to produce reliable, low-cost, high-power conversion efficiency for wide user applications. However, several issues, such as the efficiency of the photovoltaic cell to overcome the Shockley-Queisser limit, material availability, device durability, involvement of toxicity process, system storage, and power measurement, have still become challenges for this technology [24].

Based on the Carnot cycle principle in thermodynamics, the temperature difference between the sun and earth produces ideal maximum efficiency of around 95%. However, a typical silicon solar cell technology cannot achieve this theoretical efficiency. According to the Shockley-Queisser limit, the maximum efficiency is 30% for a single junction solar cell with an energy band gap of 1.1 eV [25]. The vast differences are caused by transmission and thermalisation losses significantly related to the cell material band gap [24].

In the solar cell working principle, the transmission loss is due to the photon from the sun ray that has energy components below the material's energy band gap will not be absorbed by the device. The photon energy from sunlight higher than the energy band gap of the material will be absorbed and produce electron-hole pairs. The free-electron carriers will excite a high state within the conduction band state. These electrons will become thermalised into heat energy at the conduction band edge. Optimising the material's band gap is essential to balance those two kinds of losses. It can also increase the device absorption properties and improve the efficiency of the solar cell. Therefore, research is essential to understand the principal's underlying solar cell development and enhance its efficiency [26].

1.3 Solar cells Efficiency Achievement

The famous chart of NREL is illustrated in Figure 1.3. It summarises the worldwide research effort of the last 40 years and shows the current record efficiencies of solar cells at a laboratory research scale [27]. Moreover, the evolution of solar cell efficiency is categorised based on PV technology development. Thus, it shows that numerous works and research have been done to improve solar cell technology.

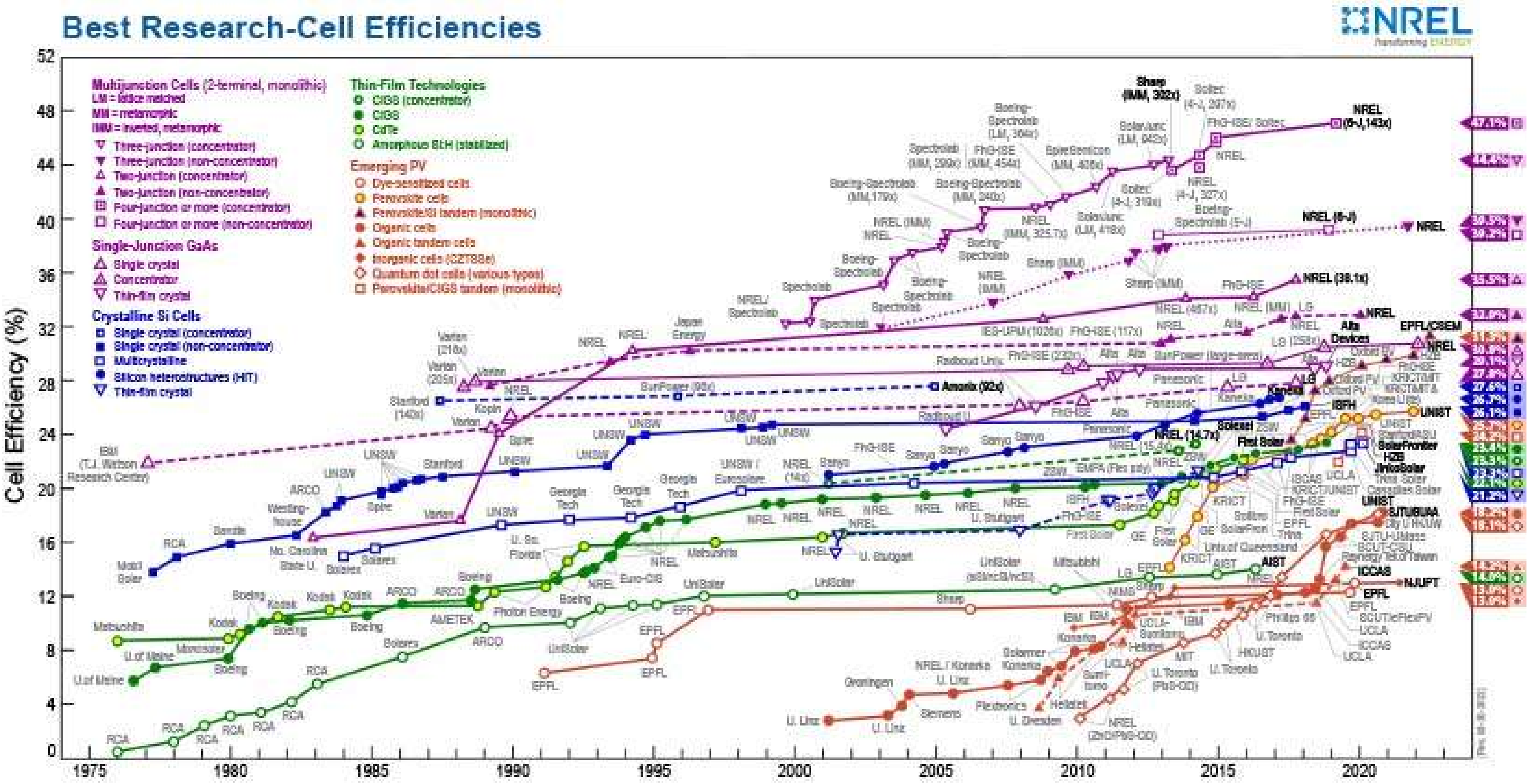

Figure 1.3: The evolution of best research solar cell efficiencies since 1975 [27].

It is taken from https://www.nrel.gov/pv/cell-efficiency.html

"This plot is courtesy of the National Renewable Energy Laboratory, Golden, CO."

The blue lines and dots represent the first PV generation made from crystalline silicon technology based on mono-crystalline and multi-crystalline silicon. Since it is made from pure quality material, it has fewer defects and relatively high efficiency. Moreover, it produces a broad spectral absorption range and high-current mobility. The best crystalline silicon solar cell efficiency record ranges from 23% up to 27.6% under concentrator [27]. However, producing highly pure silicon wafers in solar cell fabrication requires expensive technology and manufacturing processes to convert impurity sand into purified silicon semiconductor wafers. Another disadvantage is that most energy photons at the blue and violet spectrums absorbed by the silicon solar cell are wasted into heat [28].

Next are the thin-film technologies indicated by the green markers, whose record efficiencies range from 14% rise to 23.4% per cent [27]. The fabrication of thin-film technology implies low material cost than the first generation and reduces high-temperature processing. It is made on a large area, such as glass and plastic, with absorber material such as Cadmium Telluride (CdTe), Copper Indium Gallium Selenide (CIGS) and amorphous silicon. Despite the advantage of cheaper production cost of the solar cell, the efficiency is much lower than the maximum Shockley-Queisser limit efficiency and relatively lesser than silicon solar cell. In addition, the manufacturing process involves toxic materials such as Cadmium(Cd) and Telluride (Te) elements [28]. It is hard to make a thin-film solar cell as efficiently as traditional silicon-based solar panels.

The red colour lines and markers indicate emerging PV technologies like perovskite, Dye-Sensitized Solar Cells (DSSC) and organic solar cells. This category is based on the solar cell concept, which tries to improve conversion efficiency and maintain low-cost production. Therefore, it is expected would be higher than Shockley-Queisser's theoretical limit achieved from the first and second generations. Furthermore, the cost of the materials and processing techniques used to develop third-generation solar cells are expected to be cheaper. From the record, the efficiency contributed from this category has dramatically increased from around 13% to 25.7%. Moreover, the development of Perovskite/Si tandem cells achieved 29.8% efficiency, which is higher than silicon under the concentrator [27].

The purple colour markers represent the III-V PV technology based on single, double and triple junction solar cells. In the application of many junctions, it is called a multi-junction solar cell. This fourth PV technology uses semiconductor material from group III-V in the periodic table, such as Gallium Arsenide (GaAs) and Gallium Indium Phosphide (GaInP) [24]. The concept of a multi-junction solar cell is to reduce transmission and thermalisation losses by manipulating each junction's band gap to absorb full solar spectrum wavelengths and convert to higher-energy conversion [24]. It is shown that the efficiencies range from 27.8% up to 47.1% under concentrated light conditions [27]. The multi-junction is the most efficient solar cell today and is used in concentrated PV technology in space exploration applications. This technology has great potential to overcome the Shockley-Queisser limit. The motivation and contribution from this thesis outcome are related to developing the multi-junction solar cell.

1.4 Multi-junction solar cell

The solar spectrum comes in a wide range of photon energies. A single band gap material only absorbs a fraction of photon energies, and the rest are transformed into losses. As we recall, any electron that is excited higher than the energy band gap will relax down to the edge of the conduction band losing energy through thermalisation. As a result, the efficiency of single junction solar cells is limited by the thermalisation losses. The excitation of the electron-hole carrier is most efficient when the band gap matches all the photon energies of the solar spectrum. One way to surpass this limitation is by using multi-junction solar cells.

The multi-junction solar cell is designed by integrating a series of solar cells with different band gaps in a stacked layer [29]. The top layer cell is made from a higher energy band gap. Then, it is followed by a bottom layer with lower energy band gap material. Each layer or junction absorbs a different fraction of the solar spectrum. When sunlight enters the top layer, it only absorbs the higher energy photons. The photons lower than the top layer energy band gap will be practically transparent to the bottom layer and absorbed accordingly. Ideally, the efficiency of multi-junction solar cells surpasses the Shockey-Quiesser limit, shown in NREL's solar cell efficiency chart [27]. The highest efficiency of multi-junction solar cell was recorded at 47.1 % under the concentrator [27].

The model of a multi-junction solar cell is relatively simple to conceptualize. However, the actual implementation is more complex. One of the main challenges is material selection. The industrial standard of a multi-junction solar cell is called the III-V multi-junction solar cell. It is because the material is made from the combination of group III and group V elements in the periodic table. In order to electrically connect the different layers, it needs to ensure that these layers have a relatively similar lattice constant. As such that, the lattice connection at the interface is continuous. Otherwise, a lattice-mismatch effect will induce strain and defects at the interface of the connecting layers. This issue will prevent efficient charge transport and performance of the solar cell.

Another challenge is current matching in multi-junction solar cells. The band gap of the semiconductor determines the number of photons absorbed. Thus, the number of photons will determine the short circuit current. Each junction must produce a similar short circuit current for optimal performance of a multi-junction solar cell. However, the higher the top sub-cell band gap, the lower its short-circuit current. The top sub-cell band gap allows a more excellent range of light to pass through to the bottom layer. The bottom layer short circuit current increases higher than the top layer band gap. It is vital to avoid the lowest short circuit current from the sub-junction band gap limits the current of the entire device, and the additional current produced by other junctions becomes wasted [24]. Therefore, one of the mechanisms to achieve current matching between individual junctions is by optimizing each layer's absorbing thickness and selecting material with a suitable energy band gap.

A well-established commercial multi-junction solar cell product is InGaP/InGaAs/Ge, which stands for (Indium Gallium Phosphide/Indium Gallium Arsenide/Germanium). This three-junction solar cell is constructed from III-V compound semiconductor materials on a Germanium substrate. It is a cutting-edge commercial multi-junction solar cell device that has gained prominence in the photovoltaics application due to its high efficiency and versatility. This technology is renowned for efficiently converting sunlight into electricity for a wide range of solar spectra. It is particularly suitable for space applications, terrestrial concentrator photovoltaics (CPV), and other high-efficiency solar energy systems.

In the field of space exploration, this device efficiency performs 41.6% [30-31]. Moreover, InGaP/InGaAs/Ge solar cells, which exhibit high efficiency and radiation resistance, have been used in various space missions by space agencies like NASA and the European Space Agency (ESA). These solar cells are ideal for powering spacecraft and satellites due to their exceptional capabilities. Moreover, they are also being increasingly used in terrestrial CPV systems, where their high efficiency and concentration capability can significantly reduce the cost of solar energy production.

The InGaP/InGaAs/Ge solar cell comprises three distinct semiconductor layers, each optimized to absorb different portions of the solar spectrum. Figure 1.4 illustrates a three-junction solar cell InGaP/InGaAs/Ge with the material energy band gap properties and the solar spectrum wavelength.

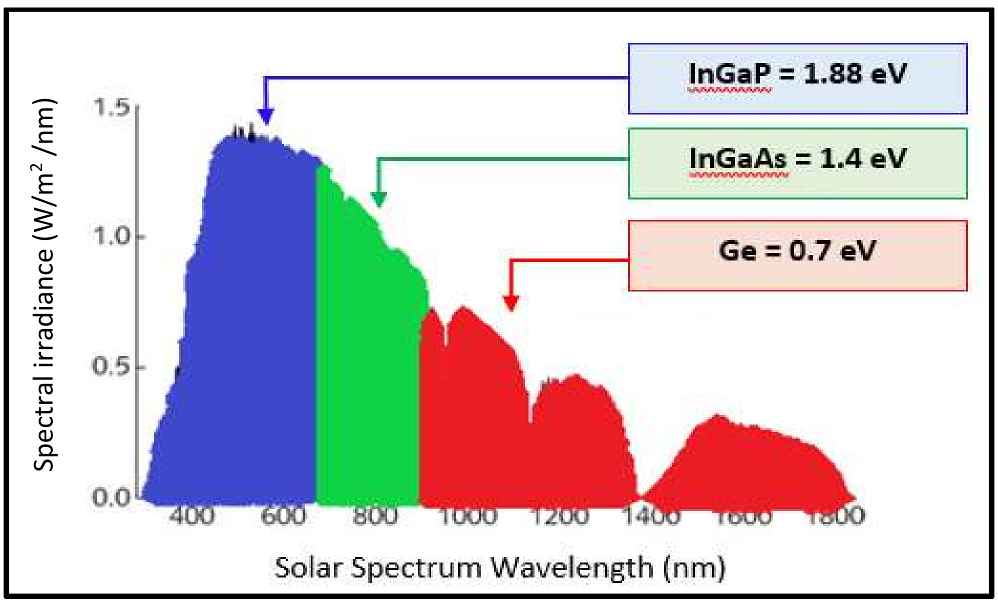

Figure 1.4: Example of established three junctions solar cell and solar spectrum profile [32]

adapted from [32]

The top layer or junction is typically made of Indium Gallium Phosphide (InGaP), with a band gap of 1.88 electron Volts (eV). It is designed to absorb high-energy photons in the blue and green solar spectral regions, which are in the range of 660 nm. The middle junction, composed of Indium Gallium Arsenide (InGaAs) with an energy band gap of 1.40 eV, absorbs photons in the near-infrared spectrum wavelength from around 890 nm. Finally, the bottom layer, constructed from Germanium (Ge) with a band gap of 0.7 eV, captures low-energy infrared photons that comprise a longer wavelength above 900 nm [32]. This multi-junction design enables more efficient solar spectrum utilization than traditional single-junction solar cells. Furthermore, these semiconductor materials are carefully selected because their lattice constants are relatively similar, allowing them to be electrically connected correctly.

Furthermore, the tunability of the bandgaps in each semiconductor layer enables the customization of InGaP/InGaAs/Ge solar cells for specific applications. For instance, by adjusting the composition of the semiconductor layers, researchers can optimize the solar cell for different solar spectra or operating conditions, further enhancing its performance and versatility.

Despite the fact that the Germanium is fittingly lattice-matched with the lattice constant requirement below the InGaAs junction, its band gap is far lower than the ideal 1 eV for optimum performance of the three-junction solar cell [32]. Since Germanium has the lowest band gap, it absorbs more photons than the top and intermediate cells. As a result, the amount of short circuit current produced by Germanium is almost twice the amount of limiting current produced by the top and middle junction [24]. This excess of high generated current is also not valuable for the overall device performance. Moreover, it has a lower open circuit voltage [33]. Hence, to achieve higher efficiency in multi-junction solar cells, another sub-junction with an optimum band gap of around 1 eV is recommended [34].

1.5 1 eV junction solar cell

The efficiency of commercial three-junction solar cells is forecasted to increase significantly by introducing a 1 eV junction with a lattice-matched material in the commercial multi-junction solar cell architecture. [31,34-37]. Incorporating a 1 eV semiconductor material in between the InGaAs and Ge to form the four-junction solar cell or implementing the 1 eV junction with substituting Germanium with other 0.7 eV band gap material is projected to enable multi-junction solar cells to achieve over 50% efficiency under concentrator [34,38]. This estimation is based on the theoretical model of multi-junction solar cells demonstrated in studies by S.Kurtz et al [34].

Moreover, a higher number of junctions in multi-junction solar cell devices is predicted to achieve as high as 50% efficiency [31,35,37,39].

However, the exact sub-junction with an optimum 1eV band gap of III-V binary material has yet to be commercially available [40]. This condition opens a wide range of options from the III-V ternary semiconductor group to meet the 1 eV band gap requirement. One of the main challenges is finding a III-V material that can be lattice-matched and provide better electronic properties within the GaAs structure.

One effective method for achieving a strain-compensated structure to obtain a 1eV bandgap is to utilize strain-balanced material structures, such as InGaAs/GaAsP multiple quantum wells (MQWs) [41]. For instance, a fully lattice-matched 70-period InGaAs/GaAsP MQW, reported by K. Toprasertpong et al., can extend absorption of external quantum efficiency up to 1068 nm wavelength. This device achieves over 75% current density compared to a 35-period MQW and nearly meets the targeted open-circuit voltage required for a quad-junction cell to achieve 50% efficiency. However, high dark current with the domination of non-radiative recombination causes degraded carrier collection and is also the main factor that affects the open-circuit voltage [42]. InGaAsP with a 1 eV band gap produces higher short-circuit current density, above 40.69 mA/cm2 under the AM1.5 solar spectrum [43]. It also reaches a fill factor of 77.75%, significantly close to the targeted quad-junction demonstrated in [42-43]. However, the device has a shorter recombination time due to higher doping density. Decreasing the doping density of the base layer and improving growth parameters will enhance the device's performance, especially the open-loop voltage [43].

Another challenge in creating a strain-balanced structure is that modifying the thickness layer can lead to unavoidable strain mismatch. However, the potential of the inverted metamorphic (IMM) layers technique is to develop a high-quality device structure for highly mismatched III-V semiconductor materials that can enhance solar cell efficiency. The IMM layers are grown by first developing lattice-matched top junctions on the host substrate, followed by the lowest bandgap layer. This process helps to minimize defects, conserves the device structure from the metamorphic layer effect, and improves efficiency. Additionally, the prospect of substituting the Germanium with a band gap (0.67 eV) located at the bottom layer in the InGaP/InGaAs/Ge structure with either InGaAs or CuInSe2, both of which have a 1eV band gap, is anticipated to result in a solar cell structure with better efficiency. An inherent limitation of this technology is that the IMM device's processing requirements are more intricate than ordinary solar cells [44-46].

Moreover, introducing diluted nitride into the host material, Gallium Arsenide (GaAs), can increase emission wavelength and decrease bandgap energy by 125meV per atomic percentage of incorporating nitrogen [47]. The interaction between the nitrogen resonant state and the conduction band of GaAs results in an anti-crossing effect in the energy band structure. As a result, the conduction band's minimum energy level extends below the minimum and significantly reduces the band gap. The bowing coefficient for GaAsNis approximately 10 eV and is highly influenced by the nitride composition [48]. This coefficient's magnitude is significantly higher than the average bowing coefficient found in other material systems, usually around 0.1 eV and independent of composition.

D.J. Friedman et al. have successfully incorporated nitride into InGaAs to create a 1 eV junction material known as InGaAsN [49]. The fill factor can range from 61% to 66%, whereas the increase in internal quantum efficiency is minimal, at just 0.2. Several research groups have investigated the incorporation of around 3% nitrogen and 8% antimony (Sb) into GaAs to create a 1 eV GaAsNSb material [50-51]. For instance, T. Thomas et al. demonstrate the model of GaNAsSb 1eV solar cell with the composition of 1.8% nitrogen and 8.5% Sb. This structure produces a short-circuit current at 23.6 mA/cm2, an open-circuit voltage of 0.44 V, and a fill factor of 67%. This composition model is restricted by the surface recombination and diffusion length [52].

Another example of 1 eV GaNAsSb is that incorporating 2% of Nitride with 6% of Sb enables the production of 15 mA/cm2 short-circuit current under AM 1.5G solar simulator with 850 nm long-pass filter. The fill factor obtained from the measurement is around 56% [53]. Nevertheless, the open-circuit voltage is also limited by the short minority carrier lifetime. The main obstacle in incorporating dilute Nitride is the growth process's difficulties, caused mainly by the significant disparity in lattice constant and thermal expansion coefficient [54]. Nitrogen incorporation significantly impacts the photoluminescence efficiency, minority carrier diffusion length, and electron mobility due to its typical development at low temperatures.

GaAsBiN is a material system capable of achieving a 1eV energy bandgap. It is formed by combining Bismide and Nitride with GaAs. Sweeney et al. utilize a band anti-crossing theory model to forecast the potential of GaAsBiN [55-56]. Introducing Bi into GaAs results in an interaction with the valence band, whereas incorporating nitride results in an interaction with the conduction band. Consequently, adding tiny percentages of both elements results in a lattice-matched system that significantly decreases GaAs's bandgap below the value of 1.42eV.

Optimizing the proportions of both Bi and N is anticipated to decrease the strain value. This is due to achieving a nearly lattice-matched GaAs structure when both elements are combined in a quad-alloy. Despite the challenging growth conditions of this material system, there are few publications on its actual growth. Yoshimoto et al. successfully grew GaAsBiN using the Molecular Beam Epitaxy machine in 2004, a significant achievement that validated the potential of this research. The characterization properties of the grown material were subsequently presented a few years later [57-59].

Thus, the development of inverted metamorphic growth [44-46], dilute nitride [60], dilute bismide [61] and multiple-quantum well [62] demonstrates the experimental promise of the 1 eV technology for increasing the efficiency of the multi-junction solar cell. In recent years, the research on Bismuth (Bi) has attracted significant attention, and it is proposed as a suitable candidate to fill in the 1 eV band gap material [61-62]. This thesis goes a step further demonstrating the significant potential of GaAsBi technology for improving solar cell performance.

Hence, the development of inverted metamorphic growth [44-46], dilute nitride [60], dilute bismide [61], and multiple-quantum well [62] demonstrates that the 1eV technology is experimentally promising for increasing the efficiency of the multi-junction solar cell. In recent years, researchers in Bismuth (Bi) have attracted much attention, and it is proposed as an appropriate candidate to fill in 1 eV band gap material [61-62]. Thus, this thesis demonstrates the performance of solar cells based on GaAsBi technology.

1.6 Bismuth

Bismuth (Bi), also called bismide, is the last material in the group V column in the periodic chemistry table [63]. It has an atomic number of 83 and has been identified as a giant atom among III-V semiconductor elements. Bi has historically been recognized since the fifteenth century during the German Renaissance [64]. This element is verified as a green, ecologically friendly metal, exhibiting homogenous properties to lead (Pb) and more stable than neighbouring atoms such as (Pb), antimony (Sb), and arsenic (As). Moreover, it exhibits lower thermal and heat conductivity among all metal elements. Conventionally bismuth is used for electric fuses, thermoelectric products, beauty products and pharmaceutical products [63-64].

In this decade, the research interest in dilute bismide focusing on applying GaAsBi has proliferated, as illustrated in the literature [63]. Due to the advantages and exciting properties offered by this new type of highly mismatched alloy, the application of bismide has become wider [65], such as in solar cells [66], optoelectronic devices [67], laser application [68] and telecommunication [69].

1.7 Advantages of GaAsBi

The main advantage of Bismuth is related to huge band gap reduction. It reduces the energy band gap of host material such as Gallium Arsenide (GaAs) by 60-90 meV for each per cent constituent of Bismide added to replace Arsenide composition [70-73]. The incorporation of bismide will alter the valence band maximum (VBM) level, making the gap between the conduction and valence band closer. Adding a small amount of Bi at about 4% to 6% into GaAs could achieve around 1eV junction solar cell, which can be integrated continuously between InGaAs and Ge solar junction. As a result, more efficient absorption of the solar spectrum above 900 nm up to 1200 nm wavelengths is possible to establish. Besides, incorporating bismide in a GaAs material retains good electron mobility properties [74], allows a strong absorption energy coefficient and benefits the design of multi-junction solar cells.

Besides the band gap reduction, high bismide content demonstrates a huge bowing of the spin-orbit splitting energy (ΔSO) in dilute GaAsBi [75]. By adding bismide concentration, it is not only increasing the valance band maximum (VBM) but also enlarges the spin-orbit splitting energy [76]. The increment of ΔSO is estimated at 50 meV for each per cent bismide content [77-78]. Furthermore, a vast spin-orbit splitting energy is produced by incorporating above 10% bismide on host substrate GaAs achieved higher than the magnitude of energy band gap ($\Delta SO > Eg$) of the material [76-77]. Thus, it is capable of eliminating inter-valence band absorption (IVBA) and also the dominant process of non-radiative (Auger recombination) [65,77-79]. This advantage benefits the near and mid-infrared (NIR &MIR) optoelectronic laser devices [80-82]. In addition, the advantage of giant spin-orbit bowing demonstrated by GaAsBi makes it highly significant for the spintronic application [75].

Another contribution of bismuth, it is identified as a semiconductor compound with a temperature-insensitive band gap changes characteristic [83] which shows promising material for long-wavelength laser diode application [60]. Research in [84] has experimentally demonstrated that the GaAsBi decreased the temperature coefficient of the band gap. These findings are verified by modulation spectroscopy and photoluminescence spectroscopy measurement [84]. Another finding described that the GaAsBi/GaAs quantum well laser diode exhibits a long lasing wavelength reaching 1.142 um at room temperature. Its temperature coefficient is 0.26nm/K during the temperature range of 77-350 K. This value is much lower than InGaAsP/InP and InGaAs/GaAs laser diode characteristics [85].

1.8 Aim of the Research

A previous study on the electrical properties of the GaAsBi P-i-N diodes has been conducted on the series of bulk and MQW p-i-n diodes [62,86-88]. The findings focus on the growth characteristic, the dark current analysis and solar cell performance at room temperature 300K. However, the practical operating temperature of the solar cell during sunlight is more than 60 OC. The solar cell temperatures are getting hotter as the devices are operated under concentrated sunlight.

At higher temperatures, the band gap properties of the GaAsBi will change. This condition theoretically alters the photovoltaic effect performance and solar cell parameters, especially the open-circuit voltage. In principle, the temperature variation will affect the open-circuit voltage more than the short-circuit current. Therefore, further detailed analysis and experimental measurement will be conducted to investigate the physics of the solar cell at higher temperatures and, thus, become the main objective and scope of this research work.

Three keys analysis is conducted under this research project to evaluate the performance of GaAsBi solar cells at temperature-dependent temperature. The first is to investigate the dark current behaviour of the GaAsBi bulk and MQW P-i-N diode as temperature increases from 293K up to 393K. This finding will verify the performance between those two sets of devices before being illuminated by the light source. Secondly, to model the solar cell parameters such as short-circuit current, open-circuit voltage and fill factor of the GaAsBi P-i-N diodes based on photocurrent measurement. It is generated from illumination under monochromatic light as temperature varies from 293K to 393K. The third study in this thesis is the carrier trapping effect on the MQW GaAsBi P-i-N diode based on current-voltage characteristics at low-temperature dependent from 15K to 300K.

The objectives of this thesis are highlighted below;

1. To investigate temperature-dependent of dark current performance between GaAsBi bulk and MQW P-i-N diodes.
2. To model the solar cell parameters of the GaAsBi MQW P-i-N diodes based on the illumination of monochromatic light as temperature varying from 293K up to 393K.
3. To investigate the carrier trapping effect on the MQW GaAsBi P-i-N diode based on light illumination at low-temperature dependent from 15K to 300K.

1.9 Structure of the thesis

Chapter 1 describes an introduction to solar energy, the efficiency of solar technology based on the NREL chart and the development of the multi-junction solar cell. This chapter also discusses the advantages of dilute bismuth for optoelectronics device applications and the potential for developing a 1eV junction for multi-junction solar cells.

Chapter 2 introduces several significant background theories to support the development of the research studies. These include the III-IV semiconductor structure, energy band gap, lattice match, PN junction, multiple quantum well structure and solar cell parameters. Moreover, this chapter also explains the principle related to the dark current analysis.

Chapter 3 briefs the growth of the GaAsBi devices used in this research work. Then, it discusses the methodology and experimental works conducted in this thesis. The temperature-dependent dark current set-up, the modelling of solar cell parameters and the light-bias carrier trapping experimental set-up are explained in this chapter.

The fourth chapter analyses the performance of the dark temperature current for both types of GaAsBi P-i-N devices. Several key findings, such as the ideality factor, recombination dominant and effect of temperature dependent on the devices, are shown in this chapter. Chapter 5 comprises two main findings. The study discusses the solar cell parameters based on photocurrent measurement under monochromator illumination. It is performed on the MQW P-i-N diodes with temperatures varying from 293K to 393K. Then, the second results discuss the effect of carrier trapping in the QW 20 P-i-N diode.

Chapter 6 is the final chapter that concludes with the findings of temperature-dependent dark current analysis, solar cell parameter characteristics and light-bias carrier trapping effect. This chapter also highlights recommendations for future work.

References

[1] World Energy Outlook Report 2019, International Energy Agency

[2] Z. Jiang, B. Lin, "China's energy demand and its characteristics in the industrialization and urbanization process", Energy Policy, Vol. 49 (2012), pp. 608-615, Elsevier, doi.org/10.1016/j.enpol.2012.07.002.

[3] M.S. Hossain, "Panel estimation for CO2 emissions, energy consumption, economic growth, trade openness and urbanization of newly industrialized countries", Energy Policy, Vol. 39 (2011), Issue 11, 2011, pp 6991-6999, Elsevier.

[4] C. Zhang, K. Zhou, S. Yang, Z. Shao, "On electricity consumption and economic growth in China", Renewable and Sustainable Energy Reviews, Vol. 76 (2017), 2017, pp. 353-368, Elsevier, doi.org/10.1016/j.rser.2017.03.071.

[5] W. Zheng, P.P. Walsh, "Economic growth, urbanization and energy consumption — A provincial level analysis of China", Energy Economics, Vol. 80 (2019), 2019, pp. 153-162, Elsevier, doi.org/10.1016/j.eneco.2019.01.004.

[6] A. Al-Badi, I. AlMubarak, "Growing energy demand in the GCC countries." Arab Journal of Basic and Applied Sciences, Vol. 26 (2019), Issue 1, 2019, pp. 488-496, Taylor & Francis, doi.org/10.1080/25765299.2019.1687396.

[7] M. Shahbaz, A.R. Chaudhary, I. Ozturk, "Does urbanization cause increasing energy demand in Pakistan? Empirical evidence from STIRPAT model", Energy, Vol. 122, 2017, pp. 83-93, Elsevier, doi.org/10.1016/j.energy.2017.01.080.

[8] R.V. Jones, K.J. Lomas, "Determinants of high electrical energy demand in UK homes: Appliance ownership and use", Energy and Buildings, Vol.117, 2016, pp. 71-82, Elsevier, doi.org/10.1016/j.enbuild.2016.02.020.

[9] Streck, C., Keenlyside, P. and Von Unger, M., "The Paris Agreement: a new Beginning", Journal for European Environmental & Planning Law, Vo. 13(1), 2016, pp. 3-29, Brill, doi.org/10.1163/18760104-01301002.

[10] O. Gippner, D. Tomey, "Shifting policy priorities in EU-China energy relations: Implifications for Chinese energy investment in Europe", Energy Policy, Vol. 101 (2017), pp. 649-658, Elsevier.

[11] Jesica de Boer, C. Zuidema, A. van Hoorn, Gert de Rpp, "The adaption of Dutch energy policy to emerging area-based energy practices", Energy Policy, Vol. 117 (2018), pp. 142-150, Elsevier.

[12] T. Ahmed, S. Mekhilef, R. Shah, N. Mithulananthan, M. Seyedmahmoudian, B. Horan, "ASEAN power grid: A secure transmission infrastructure for clean and sustainable energy for South-East Asia", Renewable and Sustainable Energy Reviews, Vol. 67 (2017), pp. 1420-1435, Elsevier.

[13] M. Santamouris, S. Haddad, M. Saliari, K. Vasilakopoulou, et. al, "On the energy impact of urban heat island in Sydney: Climate and energy potential of mitigation technologies", Energy and Buildings, Vol. 166 (2018), pp. 154-164, Elsevier.

[14] I. Ziogou, A. Michopoulos, V. Voulgari, T. Zachariadis, "Implementation of green roof technology in residential buildings nd neighborhoods of Cyprus", Sustainable Cities and Society, Vol. 40 (2018), pp. 233-243, Elsevier.

[15] Larissa de Souza Noel Simas Barbosa, D. Bogdanov, P. Vainikka, C. Breyer, "Hydro, wind and solar power as a base for a 100% renewable energy supply for south and Central America", Open access, PLoS One, 2017, doi.org/10.1371/jounal.pone.0173820.

[16] S.R. Bull, "Renewable Energy Today and Tomorrow", Proceedings of the IEEE, vol. 89, no. 8, pp. 1216-1226, Aug. 2001, doi: 10.1109/5.940290

[17] D. Abbott, "Keeping the Energy Debate Clean: How Do We Supply the World's Energy Needs?", Proceedings of the IEEE, vol. 98, no. 1, pp. 42-66, Jan. 2010, doi: 10.1109/JPROC.2009.2035162.

[18] M.D. Yandt, K. Hinzer, H. Schriemer, et. al, "Efficient Multijunction Solar Cell Design for Maximum Annual Energy Yield by Representative Spectrum Selection", IEEE Journal of Photovoltaics, Vol. 7, Issue: 2, pp. 695-701, 2017, IEEE

[19] N. Kumar, I. Hussain, B. Singh, B.K. Panigrahi, "Peak power detection of PS solar PV panel by using WPSCO", IET Renewable Power Generation, Vol. 11, Issue:4, 2017, pp. 480-489, The Institution of Engineering and Technology 2017

[20] S.A. Singh, G. Carli, N.A. Azeez, S.S Williamson, "Modelling, Design, Control and Implementation of a Modified Z-Source Intergrated PV/Grid/EV DC Charger/Inverter", IEEE Transaction on Industrial Electronics, Vol. 65, No. 6, 2017, pp. 5213-5220, IEEE

[21] Q. Wei, G. Shi, R. Song, Y. Liu, "Adaptive Dynamic Programming-Based Optimal Control Scheme for Energy Stirage Systems With Solar renewable Energy,", IEEE Transaction on Industrial Electronics, Vol. 64, No. 7, 2017, pp. 5468-5478, IEEE

[22] D. Qian, Z. Zheng, H. You, et. al, " Design rules for minimizing voltage losses in high-efficiency organic solar cells", Nature Material, Vol. 17 (2018), pp. 703-709.

[23] I. Dincer, "Renewable energy and sustainable development: a crucial review", Renewable and Sustainable Energy Reviews, Vol. 4, No. 2, 2000, pp. 157-175, doi.org/10.1016/S1364-0321(99)00011-8.

[24] S. Almosni, et.al, "Material challenges for solar cells in the twenty-first century: directions in emerging technologies", Science and Technology of Advanced Materials, Vol. 19, No. 1, 2018, Taylor & Francis, pp. 336-369, doi: 10.1080/14686996.2018.1433439

[25] W. Shockley, H.J Queisser, "Detailed balance limit of efficiency of p-n junction solar cells", Vol. 32, No. 3, 1961, Journal of Applied Physics, pp. 510-519, doi: doi.org/10.1063/1.1736034

[26] Tetsuo Soga, "Chapter 1 - Fundamentals of Solar Cell", Nanostructured Materials for Solar Energy Conversion, 2006, Elsevier, pp. 3-43, ISBN 9780444528445, doi: doi.org/10.1016/B978-044452844-5/50002-0.

[27] https://www.nrel.gov/pv/cell-efficiency.html
Access on 26 August 2022

[28] M. Imamzai, et. al, "A review on comparison between traditional silicon solar cells and thin-film CdTe solar cells". In Proceedings of National Graduate Conference (Nat-Grad 2012), pp. 1-5,

[29] A. Freundlich, A. Alemu, " Multi quantum well multijunction solar cell for space application", Physica Status Solid, Vol.2, No. 8, 2978-2981, 2005, Wiley-VCH Verlag GmbH & Co.KGaA, Weinheim

[30] J. H. Ermer *et al*., "Status of C3MJ+ and C4MJ Production Concentrator Solar Cells at Spectrolab," in *IEEE Journal of Photovoltaics*, vol. 2, no. 2, pp. 209-213, April 2012, doi: 10.1109/JPHOTOV.2011.2180893.

[31] R.R. King et al., "Solar cell generations over 40% efficiency," pres. at 26th European Photovoltaic Energy Conference, Hamburg, Germany, Prog. Photovolt: Res. Appl. (2012); doi:10.1002/pip.1255.

[32] Jeff Hecht, “Photonic Frontiers: High-Efficiency Photovoltaics: Photovoltaics takes small steps on journey to greater efficiency”, LaserFocusWorld, December 2012.
Access at:
https://www.laserfocusworld.com/test-measurement/research/article/16549510/photonic-frontiers-highefficiency-photovoltaics-photovoltaics-takes-small-steps-on-journey-to-greater-efficiency
date of access 09 September 2022

[33] H. Helmers, M. Schachtner, A.W. Bett, “Influence of temperature and irradiance on triple junction solar subcells”, Solar Energy Materials and Solar Cells, Vol. 116 (2013), pp. 144-152, Elsevier, doi:10.1016/j.solmat.2013.03.039.

[34] S. R. Kurtz, D. Myers and J. M. Olson, “Projected performance of three- and four-junction devices using GaAs and GaInP,” Conference Record of the Twenty Sixth IEEE Photovoltaic Specialists Conference, October 1997, pp. 875-878, doi: 10.1109/PVSC.1997.654226.

[35] R.R. King et al., "Band-gap-engineered architectures for high-efficiency multijunction concentrators solar cells”, pres. at 24th European Photovoltaic Solar Energy Conference, Hamburg, Germany, September 2009, pp. 55-61, doi:10.4229/24thEUPVSEC2009-1AO.5.2

[36] D. J. Friedman and S. R. Kurtz, "Breakeven Criteria for the GaInNAs Junction in GaInP/GaAs/GaInNAs/Ge Four-Junction Solar Cells,", Progress in Photovoltaics, Article vol. 10, no. 5, pp. 331-344, Aug 2002, doi: 10.1002/pip.430

[37] R. R. King *et al.*, "Next-generation, high-efficiency III-V multijunction solar cells," *Conference Record of the Twenty-Eighth IEEE Photovoltaic Specialists Conference - 2000 (Cat. No.00CH37036)*, Anchorage, AK, USA, 2000, pp. 998-1001, doi: 10.1109/PVSC.2000.916054.

[38] D.J. Friedman, “Progress and challenges for next-generation high-efficiency multijunction solar cells”, Current Opinion in Solid State and Materials, vol.14 no. 6, 2010, p.p 131-138, 14 (2010), ScienceDirect, doi.org/10.1016/j.cossms.2010.07.001.

[39] R. R. King, R. A. Sherif, G. S. Kinsey, S. Kurtz1, et al. “Bandgap Engineering in High-Efficiency Multijunction Concentrator Cells”, International Conference on Solar Concentrators for Generation of Electricity or Hydrogen, May 2005, Scottsdale, Arizona

[40] S. Almosni, et.al, “Material challenges for solar cells in the twenty-first century: directions in emerging technologies”, Science and Technology of Advanced Materials, Vol. 19, No. 1, 2018, Taylor & Francis, pp. 336-369, doi: 10.1080/14686996.2018.1433439

[41] N. J. Ekins-Daukes, J.M Barnes, K.W.J. Barnham et al., "Strained and Strain-Balanced Quantum Well Devices for High-Efficiency Tandem Solar Cells,", Solar Energy Materials and Solar Cells, Article vol. 68, no. 1, pp. 71-87, Apr 2001, doi: 10.1016/s0927-0248(00)00346-9

[42] K.Toprasertpong, H. Fujii, T. Thomos et. al, “Absorption threshold extended to 1.15eV using InGaAs/GaAsP quantum wells for over-50%-efficient lattice-matched quad-junction solar cells”,29th EU PVSEC, Amsterdam 2014, Progress in Photovoltaics Research and Application, vol.24, no. 4, pp.533-542, 2016, doi.org/10.1002/pip.2585.

[43] L. Ji, S. Lu, Y. Wu, P. Dai, L. Bian, et. al, “Carrier recombination dynamics of MBE grown InGaAsP layers with 1eV bandgap for quadruple-junction solar cells”, Solar Energy Materials and Solar Cells, vol. 127, 2014, pp. 1-5, doi.org/10.1016/j.solmat.2014.03.051.

[44] H. Yoon et al., "Progress of Inverted Metamorphic III-V Solar Cell Development at Spectrolab," in 33rd IEEE Photovoltaic Specialists Conference, San Diego, CA, May 11-16 2008, NEW YORK: Ieee, in IEEE Photovoltaic Specialists Conference, 2008, pp. 82-87. [Online]. Available: ://WOS:000273995000019

[45] J. F. Geisz et al., "40.8% Efficient Inverted Triple-Junction Solar Cell with Two Independently Metamorphic Junctions,", Applied Physics Letters, Article vol. 93, no. 12, p. 3, Sep 2008, Art no. 123505, doi: 10.1063/1.2988497.

[46] A. W. Walker, F. Bouchard, A. H. Trojnar, and K. Hinzer, "Inverted Metamorphic IIIV Triple-Junction Solar Cell with a 1 eV CuInSe2 Bottom Subcell,", International Journal of Photoenergy, Article p. 10, 2014, Art no. 913170, doi: 10.1155/2014/913170.

[47] S. Tixier et al., "Molecular Beam Epitaxy Growth of GaAs1-xBix,", Applied Physics Letters, Article vol. 82, no. 14, pp. 2245-2247, Apr 2003, doi: 10.1063/1.1565499. 26

[48] S. H. Wei and A. Zunger, "Giant and Composition-Dependent Optical Bowing Coefficient in GaAsN Alloys," Physical Review Letters, vol. 76, no. 4, pp. 664-667, Jan 22 1996, doi: 10.1103/PhysRevLett.76.664.

[49] D. J. Friedman, J. F. Geisz, S. R. Kurtz, and J. M. Olson, "1-eV Solar Cells with GaInNAs Active Layer,", Journal of Crystal Growth, Article; Proceedings Paper vol. 195, no. 1-4, pp. 409-415, Dec 1998, doi: 10.1016/s0022-0248(98)00561-2.

[50] A. Gubanov, V. Polojarvi, A. Aho, A. Tukiainen, N. V. Tkachenko, and M. Guina, "Dynamics of Time-Resolved Photoluminescence In GaInNAs And GaNAsSb Solar Cells,", Nanoscale Research Letters, Article vol. 9, p. 4, Feb 2014, Art no. 80, doi: 10.1186/1556-276x-9-80.

[51] T. Thomas et al., "GaNAsSb 1-eV Solar Cells For Use in Lattice-Matched MultiJunction Architectures,", 2014 Ieee 40th Photovoltaic Specialist Conference (Pvsc), Proceedings Paper pp. 550-553, 2014

[52] Thomas, Tomos & Fuhrer, Markus & Alvarez, Diego & Ekins-Daukes, N.J. & Tan, K. & Wicaksono, S. & Loke, W. & Yoon, Soon & Johnson, Andrew. (2014). GaNAsSb 1-eV solar cells for use in lattice-matched multi-junction architectures. 2014 IEEE 40th Photovoltaic Specialist Conference, PVSC 2014. doi:10.1109/PVSC.2014.6924980.

[53] K.H. Tan, S. Wicaksono, W.K. Loke, D. Li, S.F. Yoon, E.A. Fitzgerald, et. al, “Molecular beam epitaxy grown GaNAsSb 1eV photovoltaic cell”, Journal of Crystal Growth, vol. 335, Issue 1, 2011,pp. 66-69, doi.org/10.1016/j.jcrysgro.2011.09.023.

[54] J. S. Harris, "GaInNAs Long-Wavelength Lasers: Progress and Challenges,", Semiconductor Science and Technology, Article vol. 17, no. 8, pp. 880-891, Aug 2002, doi: 10.1088/0268-1242/17/8/317.

[55] S. J. Sweeney and S. R. Jin, "Bismide-Nitride Alloys: Promising for Efficient Light Emitting Devices in the Near- and Mid-Infrared,", Journal of Applied Physics, Article vol. 113, no. 4, p. 6, Jan 2013, Art no. 043110, doi: 10.1063/1.4789624.

[56] S. J. Sweeney, K. Hild, S. R. Jin, and Ieee, "The Potential of GaAsBiN For MultiJunction Solar Cells," in 39th IEEE Photovoltaic Specialists Conference (PVSC), Tampa, FL, Jun 16-21 2013, NEW YORK: Ieee, in IEEE Photovoltaic Specialists Conference, 2013, pp. 2474-2478. [Online]. Available: ://WOS:000340054100561

[57] M. Yoshimoto et al., "New Semiconductor GaNAsBi Alloy Grown by Molecular Beam Epitaxy", Japanese Journal of Applied Physics Part 2-Letters & Express Letters, Article vol. 43, no. 7A, pp. L845-L847, Jul 2004, doi: 10.1143/jjap.43.l845.

[58] M. Yoshimoto, W. Huang, G. Feng, and K. Oe, "New Semiconductor Alloy GaNAsBi with Temperature-Insensitive Bandgap,", Physica Status Solidi B-Basic Solid State Physics, Article; Proceedings Paper vol. 243, no. 7, pp. 1421-1425, Jun 2006, doi: 10.1002/pssb.200565270. 27

[59] M. Yoshimoto, W. Huang, G. Feng, Y. Tanaka, and K. Oe, "Molecular-Beam Epitaxy of GaNAsBi Layer for Temperature-Insensitive Wavelength Emission,", Journal of Crystal Growth, Article; Proceedings Paper vol. 301, pp. 975-978, Apr 2007, doi: 10.1016/j.jcrysgro.2006.11.118.

[60] V. Sabnis, H. Yuen, and M. Wiemer, “High-efficiency multijunction solar cells employing dilute nitrides”, AIP Conference Proceedings 1477, 2012, pp. 14-19, doi:10.1063/1.4753823

[61] T. Thomas, A. Mellor, N.P. Hylton, et. al, “Requirements for a GaAsBi 1 eV sub-cell in a GaAs-based multi-junction solar cell”, Semiconductor Science and Technology, Vol. 30, No. 9 (2017) pp. 094010,doi:10.1088/0268-1242/30/9/094010

[62] R.D. Richards, A. Mellor, F. Harun, et. al, “Photovolatic characterisation of GaAsBi/GaAs multiple quantum well devices”, Solar Energy Materials and Solar Cells, Vol. 172 (2017) pp. 238-243, Elsevier.

[63] L. Wang, L. Zhang, L. Yue, D. Liang, et. al, “Review Novel Dilute Bismide, Epitaxy, Physical properties and Device Application”, MDPI-Crystals, 2017, 7(3), 63;

[64] Otto Rohr, “Bismuth – the new ecologically green metal for modern lubricating engineering”, Industrial Lubricating and Tribology, Vol. 54. Issue:4, pp. 153-164, emeraldinsight, 2002.

[65] C.A Broderick, M. Usman, S.J. Sweeney, E.P.O Reilly, Band Engineering in dilute nitride and bismide semiconductor laser”, Semiconductor Science and Technology. 27 (2012), 094011 (14pp)

[66] R.D. Richards, F. Harun, J.S. Cheong, et. al, “GaAsBi: An alternative to InGaAs based multiple quantum well photovoltaics”, 2016 IEEE 43rd Photovoltaic Specialists Conference (PVSC), November 2016, pp. 1135-1137, IEEE

[67] K. Bertulis, A. Krotkus, G. Aleksejenko, V. Pacebutas, et. al, “GaAsBi: A material for optoelctronic terahertz devices”, Applied Physics letter, Vol. 88. Issue: 20 (2006).

[68] X. Wu, W. Pan, Z. Zhang, Y. KLi, et. al, “1.142 µm GaAsBi/GaAs Quantum Well lasers Grown by Molecular Beam Epitaxy”, ACS Photonics 2017, 4, pp. 1322-1326, ACS Publications.

[69] F. Afrin, T. Titirsha, “Speed analysis of wireless communication technology banked on HBT: An analytical approach to determine the impact of GaAs/GaAsBi diode mode”, 2015 International Conference on Computing and Communications Technologies (ICCCT), October 2015, pp. 66-71, IEEE

[70] S. Francoeur, M.J. Seong, A. Mascarenhas, et. al, “Band Band gap of GaAs1−xBix, 0<x<3.6\%”, Applied Physics Letters, Vol. 82, No. 22, pp. 3874-3876, 2005, AIP Publishing, doi: 10.1063/1.1581983

[71] S. Tixier, S.E Webster, E.C. Young, et. al, “Band gaps of the dilute quaternary alloys GaNxAs1−x−yBiy and Ga1−yInyNxAs1−x”, Applied Physics Letters, Vol. 86, No. 11, pp. 112113, 2003, AIP Publishing, doi: 10.1063/1.1886254

[72] K. Alberi, J. Wu, W. Walukiewicz, et. al, “Valence-band anticrossing in mismatched III-V semiconductor alloys”, Phys. Rev. B, Vol. 75, No. 4, pp. 045203, 2007, American Physical Society, doi: 10.1103/PhysRevB.75.045203

[73] V. Pačebutas, K. Bertulis, G. Aleksejenko, et. al, “Molecular-beam-epitaxy grown GaBiAs for terahertz optoelectronic applications”, Journal of Materials Science: Materials in Electronics, Vol. 20, pp. 363-366, 2009, Springer, doi: 10.1007/s10854-008-9625-1.

[74] C.J Hunter, F. Bastiman, A.R. Mohmaf, R.D. Richards, et. Al, “Absorption characteristic of GaAs/$GaAs_{1-x}Bi_x$ diodes in the near-infrared”, IEEE Photonics Technology Letters, Vol. 24, No. 23, 2012, IEEE.

[75] B. Fluegel, S. Francoeur, A. Mascarenhas, et. al, “Giant Spin-Orbit Bowing in $GaAs_{1-x}Bi_x$”, Phys. Rev. Lett, Vol. 97, No. 6, 2006, pp. 067205, American Physical Society, doi: 10.1103/PhysRevLett.97.067205

[76] Z. Batool, K. Hild, T.J.C. Hosea, et. al, “The electronic band structure of GaBiAs/GaAs layers: Influence of strain and band anti-crossing”, Journal of Applied Physics, Vol. 111, No. 11, 2012, pp. 113108, AIP Publishing, doi: 10.1063/1.4728028

[77] M. Usman, C.A Broderick., A. Lindsay, E.P.O’ Reilly, “Tight-binding analysis of the electronic structure of dilute bismide alloys of GaP and GaAs”, Physical Review B 84, 245202 (2011), The American Physical Society.

[78] C.A. Broderick, S. Mazzucato, H. Carrere, et. al., “Anisotropic electron g factor as a probe of the electronic structure of GaBixAS1-x/GaAs epilayers”, Physical Review B, Vol. 90, No. 19, 2014, doi:10.1103/PhysRevB.90.195301.

[79] S. J. Sweeney, "Bismide-alloys for higher efficiency infrared semiconductor lasers," 22nd IEEE International Semiconductor Laser Conference, 2010, pp. 111-112, doi: 10.1109/ISLC.2010.5642728.

[80] S. J. Sweeney, Z. Batool, K. Hild, S. R. Jin and T. J. C. Hosea, "The potential role of Bismide alloys in future photonic devices," 2011 13th International Conference on Transparent Optical Networks, 2011, pp. 1-4, doi: 10.1109/ICTON.2011.5970829.

[81] R. Butkute, A. Geizutis, V. Pacebutas, et. al, “Multi-quantum well Ga(AsBi)/GaAs laser diodes more than 6% of bismuth”, Electronics Letters, Vol. 50, No. 16, pp. 155-1157, July 2014.

[82] I. P. Marko and S. J. Sweeney, "Progress Toward III–V Bismide Alloys for Near- and Midinfrared Laser Diodes," in IEEE Journal of Selected Topics in Quantum Electronics, vol. 23, no. 6, pp. 1-12, Nov.-Dec. 2017, Art no. 1501512, doi: 10.1109/JSTQE.2017.2719403.

[83] Y. Tominaga, K. Oe, M. Yoshimoto, “Low Temperature Depedence of Oscillation Wavelegnth in GaAs1-xBix Laser by Photo-Pumping”, Applied Physics Express 3 (2010) 062201, June 2010, The Japan Society of Applied Physics.

[84] M. Yoshimoto, K.Oe, “Molecular Beam Epitaxy of GaAsBi and related quaternary alloys in Molecular Beam Epitaxy : From research to mass production”, Chapter 8, Elsevier, 2012.

[85] W. Xiaoyan, P. Wenwu, Z. Zhenpu, et. al., “1.142 µm GaAsBi/GaAs Quantum Well Lasers Grown by Molecular Beam Epitaxy”, ACS Photonics, Vol. 4, No. 6, 2017. Pp. 1322-1326, doi: 10.1021/acsphotonics.7b00240

[86] Rockett, T.B.O., et al., Influence of growth conditions on the structural and opto-electronic quality of GaAsBi. Journal of Crystal Growth, 2017. 477: p. 139-143.

[87] Richards, R.D., et al., MBE grown GaAsBi/GaAs multiple quantum well structures: Structural and optical characterization. Journal of Crystal Growth, 2015. 425: p. 237-240.

Chapter 2

Theoretical Background

In this chapter, several terms and importance semiconductor principles are described before introducing further discussion in GaAsBi technology.

2.1 Introduction to semiconductors

Semiconductors are materials that can perform electrical conductivity. Semiconductors exhibit conductivity less than conductor material and very much higher than insulators. This material's electrical conductivity property can vary relatively by giving heat energy through changes in temperature and adding impurities. Semiconductors are majorly classified into two types, known as elemental and compound semiconductor materials. Both types are widely applied in many electronic devices.

Elementary material comprises a pure single element, meaning it does not grow by combining other elements and is available in its natural structure. Example of this material is Silicon (Si) and Germanium (Ge). This kind of material has fix single energy band gap. Thus, it is limited to certain functionalities. For example, Silicon cannot emit light and is also unable to exhibit very high-speed operation in optical fibre communications. It is because to demonstrate those applications need to modify the energy band gap. In the light-emitting diodes application (LED), emitting light for different colours requires a particular energy band gap to meet the light spectrum's wavelength.

In contrast, compound semiconductors have more flexibility in designing electronic devices. It is due to the tuning energy band gap property and achieving various wavelength conditions. A compound material comprises two or more elements from different groups in the periodic table. Not all sorts of combinations will produce a semiconductor characteristic. It is formed by combining selected elements from Groups II and VI, Groups III and V and Groups IV with IV. Figure 2.1 shows several examples of compound semiconductors. However, this thesis is only focused on III-IV compound semiconductors.

Group II	Group VI	Compound	
Zinc (Zn) Cadmium (Cd)	Selenide (Se) Sulfur (S) Tellurium (Te)	ZnSe CdS CdTe	**Example of II-VI Compound Semiconductors**
Group III	**Group V**	**Compound**	
Aluminium (Al) Gallium (Ga) Indium (In)	Nitrogen (N) Phosphorus (P) Arsenic (As) Antimonite (Sb) Bismuth (Bi)	AlAs GaN GaP GaAs InP GaInP InGaAs GaAsBi	**Example of III-IV Compound Semiconductors**
Group IV	**Group IV**	**Compound**	
Carbon (C) Silicon (Si) Germanium (Ge)	Carbon (C) Silicon (Si) Germanium (Ge)	SiC SiGe	**Example of IV-IV Compound Semiconductors**

Figure 2.1: Example of compound semiconductor based on different groups combination

Each compound material has different properties, such as energy band gaps, lattice constant, effective mass and electronic carrier mobility. These properties allow the designing of new devices for many applications. For example, Aluminium Arsenide (AlAs) and Indium Phosphide have band gaps of around 2.2 eV and 1.35 eV, respectively. Indium antimonide (InSb) has an energy band gap of less than 0.17 eV and can be applied in the infrared region. Gallium nitride has a band gap of around 3.4 eV and is widely used in the ultraviolet or blue visible light region.

2.2 III-V Compound semiconductor material

III-V compound semiconductor materials combine two or more elemental substances from the periodic table of group III and IV elements. They are three types of III-IV compound material. Firstly is binary compound material. It is composed of two elements, like a Gallium arsenide (GaAs). The second category is the ternary compound. It is based on combining three elements, such as Gallium arsenide phosphide (GaAsP) material. The last composition is a quaternary compound created from four basic materials. An example of this type of material is Indium gallium arsenide phosphide (InGaAsP).

The development of III-V semiconductor elements is commonly applied for the photodetector, light-emitted diode, optical communication and other optoelectronic devices. It is because these elements' band gaps can be tailored through direct and indirect band gap properties. This compound semiconductor allows designing a narrow-band gap, medium and wide-bandgap materials. As a result, a broad wavelength spectrum for light absorption from deep ultraviolet to the far-infrared application can be achieved. For instance, Gallium Arsenide (GaAs) has a band gap of about 1.43 eV at room temperature 300K, near the infrared application [1]. In addition, these materials also have adequate thermal stability. Research has shown that incorporating elements like nitrogen or bismide into group III-V compound material results in the high potential of significant band gap reduction per unit strain [2-4].

2.3 Crystal structure of GaAs

A crystal lattice is the three-dimensional arrangement of a particle, such as an atom or molecule, represented in a diagram. Each particle is portrayed as a point or can also be indicated as an ion. This arrangement is known as a crystal lattice. A unit cell comprises a group of lattice points. It is a basic form of crystal lattice which repeats itself to generate a crystal structure. The distance between each atom in the primary unit cell is called the lattice constant. There are several other solid structures, such as amorphous and polycrystalline. However, those structures are not the focus of interest in this research work.

In III-V semiconductor alloy, similar and dissimilar atoms are linked in a cubic lattice form known as a zinc-blende crystal structure. For example, Figure 2.2 shows a basic unit of the Gallium Arsenide compound in the form of a zinc-blende crystal structure. A unit lattice of GaAs comprises four gallium atoms and four arsenic atoms bound to each gallium.

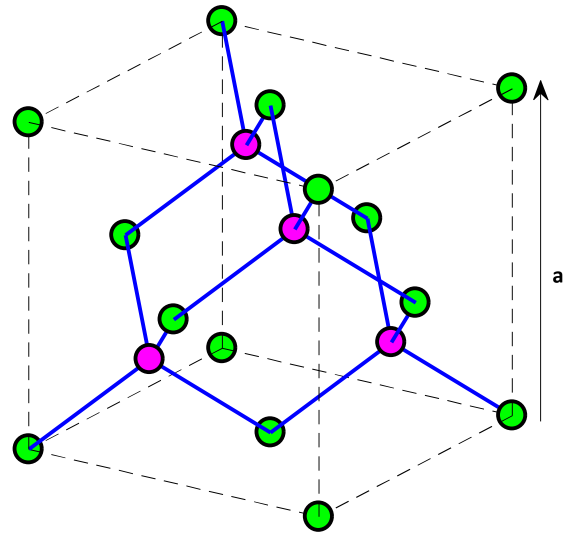

Figure 2.2: A unit lattice of GaAs zinc blende crystal structure where purple represents Gallium (Ga) atoms and green is Arsenide (As) atoms. The blue lines refer to the bonds between atoms, and '*a'* indicates the length spacing between atoms in the basic unit cell. It is also named a lattice constant.

GaAs is often used as a host substrate for the epitaxial growth of ternary III-V semiconductors compounds such as Indium gallium arsenide (InGaAs), aluminium gallium arsenide (AlGaAs), Gallium arsenide bismide (GaAsBi) and others. GaAs possess a sizeable direct band gap around 1.42 eV with a lattice constant of 5.65325 Å. It also operates at a wide temperature range for epitaxial growth and applies relatively low temperatures for surface oxide elimination. Moreover, GaAs have higher electron mobility than silicon and conveniently work for epitaxy layer growth in Molecular Beam Epitaxial (MBE) machines. As a result, GaAs is an appropriate candidate to be a host material for GaAsBi.

2.4 Basic of heterojunction III-IV semiconductor alloy

When a third element is incorporated into the III-IV compound will create a ternary III-IV semiconductor alloy. For example, Aluminium Arsenide (AlAs) and Gallium Arsenide (GaAs) compounds have band gaps of 2.2 eV and 1.42 eV respectively. In order to make Aluminium

Gallium Arsenide ($Al_xGa_{(1-x)}As$) alloy, is by adding some portion (x) of Aluminium Arsenide ($AlAs$) compound in some fraction ($1-x$) of Gallium Arsenide ($GaAs$). Adding a per cent of AlAs amount in GaAs enables tuning the band gap of the $Al_xGa_{(1-x)}As$ alloy from 1.42 eV to 2.2 eV. The *x* per cent is a mole fraction from 0 to 1. The composition in GaAsBi requires a compound of Gallium Bismide (GaBi) into the host compound of GaAs. Demonstrating 1 eV solar cell using GaAsBi alloy will require about 6% bismide content [5]. The mole fraction value is 0.06. Therefore, the composition of GaAsBi is represented as $GaAs_{0.94}Bi_{0.06}$

2.4.1 Vegards's law

Vegard's law explains that the lattice constant of the created semiconductor alloy is linearly dependent with the composition between two binary compound elements. The lattice constant for the ternary alloy ABC, (a_{ABC}) can be described in equation 2.1.

$$a_{ABC} = xa_{AC} + (1-x)a_{BC} \tag{2.1}$$

Where a_{ABC} is the lattice constant of the ternary alloy, x is the mole fraction composition of binary compound material, a_{AC} and a_{BC} are the lattice constant of compound material and host material respectively.

Vegard's law also can be used to model linear interpolation for the band gap of ternary semiconductor alloy. However, the band gap of the semiconductor alloy typically does not follow this relationship linearly. A correction parameter known as bowing parameter is applied to fit the non-linear bending behaviour of the alloy's energy band gap. Equation 2.2, shows the relationship between the energy band gap of ternary alloy (E_{ABC}) and the composition of the compound materials.

$$E_{ABC} = xE_{AC} + (1-x)E_{BC} + x(1-x)b \tag{2.2}$$

Where E_{ABC} is the band gap of the ternary alloy, x is the mole fraction composition of binary compound material, E_{AC} and E_{BC} are the band gap of compound material and host material respectively.

The energy band gap as a function of lattice constant (a) at room temperature 300K for several III-IV ternary alloys are illustrated in Figure 2.3. For instance, the AlGaAs alloy can be heteroepitaxy grown on the GaAs substrate with relatively small lattice mismatch since the GaAs and AlAs compounds both are in the form of zinc blende crystal structure and have a nearly close lattice constant which is 5.6533Å and 5.6605Å respectively [1]. The lattice constant for GaAsBi alloy and GaAs compound is considered a relatively high lattice-mismatch alloy. It is because as the composition of bismide increases to reduce the GaAs band gap, the lattice mismatch becomes larger. Based on illustration in the chart, the lattice parameter between these materials increases as the desired band gap reduces from 1.42 eV to 1.0 eV.

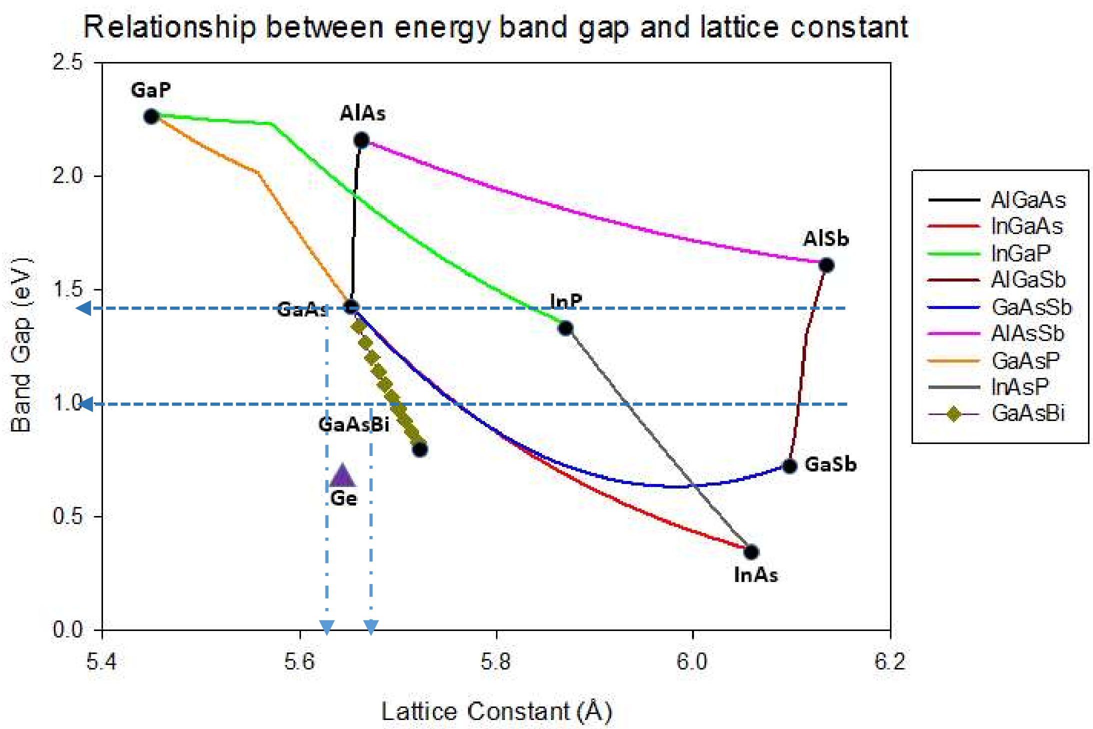

Figure 2.3: The Band gap in eV unit is plotted for lattice constant in Amstrong (Å) unit for selected III-IV ternary alloys. Adopted from [1].

2.4.1 Band anti-crossing Model (BAC)

Since Vegard's law establishes a linear interpolation relationship, estimating the band gap reduction in several III-IV semiconductor alloys is not appropriately practical. Due to a large amount of bowing coefficient applied, Equation 2.2 cannot effectively estimate the material's band gap. For instance, the calculated bowing parameter demonstrated for Gallium Arsenide Nitride (GaAsN) is 25 eV. The value is immense for ternary semiconductor compound estimation, typically a smaller amount than 1 eV [6]. Several other principles and techniques are used to estimate the band gap value, such as dielectric modelling, density functional theory and tight-binding band structure [7-10]. The band anti-crossing model (BAC) is also one of the approaches to estimating the band gap for highly mismatched alloy materials.

The Band Anti-Crossing (BAC) model is a theoretical framework that explains the significant reduction in the band gap observed in dilute nitrides. According to the BAC model, the interaction between the localized nitrogen states and the extended conduction band states of the host semiconductor leads to a new electronic band structure.

In the host semiconductor (for example GaAs), the conduction band minimum is typically at the Brillouin zone point. This means that at the Brillouin point, the wave vector, which describes the phase of the electron wave-function, has no components in any direction. This point is located at the origin of the reciprocal lattice. Therefore, when a nitrogen atom is incorporated, it introduces highly localized energy states within the band structure. The localized nitrogen states interact with the conduction band states of the host semiconductor, resulting in the repulsion and reformation of the energy bands. This interaction leads to the formation of two new hybrid bands: a lower energy band (E^{-}) and a higher energy band (E^{+}).

The system can be described by a 2x2 Hamiltonian matrix integrating the interaction between the energy of the conduction band minimum denoted (E_C) and the energy level of the localized nitrogen states (E_N). By diagonalizing this matrix, we obtain the new energy eigenvalues for the system, representing the new hybrid bands E^{-} and E^{+}. The lower energy band (E^{-}) represents the new conduction band edge, which is significantly lower than the host semiconductor's original conduction band edge. This shift process results in a reduced band gap. The reduction in the band gap allows dilute nitrides to absorb longer wavelengths of light, making them suitable for infrared applications. In addition, this phenomenon contributes to the ability to absorb a broader spectrum of sunlight and improves the overall efficiency of solar cells.

In this case GaAsBi, the localised state introduces in the valance band. This concept is proposed to model the band gap reduction in other highly mismatched semiconductors, such as GaAsBi.

2.4.3 GaAsBi band gap estimation using VBAC model

It is well known that the advantage of bismide enables band gap reduction of about 70-90 meV/%Bi content [11-12]. Incorporating bismide composition in host GaAs material introduces localised bismide states interacting strongly with valence band maximum (VBM). The changes in the VBM are more prominent than the conduction band. Therefore, the BAC model is adopted to define this phenomenon by introducing the valence band anti-crossing model (VBAC) [13].

Incorporated Bismide atom introduces localized impurity states in the valence band region of the host material (in this case, GaAs substrate). These localized states interact with the valence band states of the GaAs, leading to the formation of new hybrid energy band states. The localized Bismide states interact with the GaAs band structure by splitting the valance band into two energy sub-bands, theoretically named the higher energy band edge, E^+, and lower energy band edge, E^-. The E^+ becomes the new valence band maximum (VBM). This condition increases the valence band closer to the conduction band, which defines the band gap reduction in host GaAs material.

However, the bismide may also affect the behavior of conduction band minima, which can be estimated using virtual crystal approximation (VCA) [14]. As a result, the band gap of GaAsBi ternary alloy is the energy difference between the new conduction band minimum (CBA) and the new valence band maximum (VBM). The formulation of the energy band for GaAsBi can be represented using the equation below;

$$E_{\pm}(GaAsBi) = \frac{E_v(GaAsBi) + E_{Bi} \pm \sqrt{(E_v(GaAs) - E_{Bi})^2 + 4xC_{Bi}^2}}{2} \tag{2.3}$$

$$E_v(GaAs) = -\frac{\hbar^2 k^2}{2m^*} \tag{2.4}$$

The new approximation for conduction band

$$E_{CB-VC} = E_g(GaAs) - \Delta E_{CBM} \tag{2.5}$$

The energy band gap of GaAsBi

$$E_g(GaAsBi) = E_{CB-VC} - E_+(GaAsBi) \tag{2.6}$$

The explanation of the parameters in the above equation is described below;

$E_\pm(GaAsBi)$	energy of sub-bands split in the valence band
$E_v(GaAs)$	energy of the valence band maximum (VBM) for GaAs
E_{Bi}	energy of the Bi level
x	bismide, (Bi) concentration (from 0 to 1)
C_{Bi}	coupling between Bi level and the GaAs valence band maximum
$\hbar$	reduced Plank constant or Dirac constant, $\hbar = (\frac{h}{2\pi})$. Where h is Plank constant equal to 6.626 ×10-34 J.Hz-1
k	momentum
m^*	effective mass of hole
$E_g(GaAs)$	energy band gap of GaAs is approximately 1.42 eV
ΔE_{CBM}	conduction band offset between GaAs and GaBi is approximately 2.3 eV [14]

2.4.4 Hetero-epitaxy structure

A high-quality crystal layer can be grown in a homo-epitaxy layer where the crystalline film grows in a similar substrate. However, multi-junction solar cell architecture grows the desired crystalline epitaxy in a different host substrate material. Both compounds have different band gap properties and stack up on one another. This arrangement is known as a hetero-epitaxy structure. The relationship between band gap and lattice mismatch between desired materials limits it. Growing the material in hetero-epitaxy is complex due to differences in growth temperature between materials, lattice constant dissimilarity, layer thickness, and bonding between different atoms. Despite this complexity, the semiconductor alloy can be developed in a high vacuum molecular beam epitaxy (MBE) machine.

The slight difference between both compounds' lattice constant will create a lattice-mismatched. In this situation, both material atoms will pull apart a little so that they can be fitted one on top of the other in an epitaxial structure. This process develops strain or stress at the junction layer. A significant increment will cause misfit dislocation defects [1] and form a relaxation epilayer at the end of the growth. The lattice misfit defect is described as;

$$F = \frac{a_o(s) - a_o(f)}{a_o(f)} \tag{2.7}$$

Noticed that; $a_o(s)$ is the lattice constant of the substrate and $a_o(f)$ is referred to as a relaxed lattice constant of the desired film material. When the misfit (F) magnitude is small, and the layer is thin, the tensile strain will compress and help the epi-layer lattice match with the substrate. Pseudomorphic layers are built up across the host substrate. In contrast, if the growing thickness of the epi-layer increases further beyond critical thickness tc, the strain energy in the layer will form a misfit dislocation defect and lead to a relaxed layer. This means the layer must have sufficient thickness so that the material cannot be strained into the layer below, referred to as metamorphic.

A metamorphic layer, a crucial element in semiconductor device fabrication, is an intermediate layer grown between a substrate and a strained epitaxial layer. Its primary role is to manage and accommodate the lattice mismatch between them, preventing excessive strain and dislocations. The metamorphic layer gradually changes its lattice constant from the substrate to that of the epitaxial layer, effectively reducing the strain in the epitaxial layer. By grading the composition, the metamorphic layer can absorb dislocations and defects, preventing them from propagating into the active epitaxial layer. The thickness of the metamorphic layer is not arbitrary but carefully designed. It must be sufficient to accommodate the gradual change in the lattice structure without propagating dislocations.

In the context of growing GaAsBi on a GaAs substrate, where the GaAsBi layer requires a higher Bi content for a reduced band gap, a metamorphic layer can manage the strain. GaAsBi graded buffer layer can be grown, gradually changing the composition from GaAs to the desired GaAsBi. The thickness of this graded layer is designed to be sufficient to transition the lattice constant smoothly, minimizing dislocation propagation.

Figure 2.4 illustrates the two conditions of surface growth based on the description of the thickness of the grown layer. Hence, it is possible to achieve a high-quality hetero-epitaxy crystal structure of GaAsBi on the GaAs substrate. This depends on adding a sufficient amount of Bi composition into the substrate material, which must adhere to the lattice mismatch and critical thickness parameters.

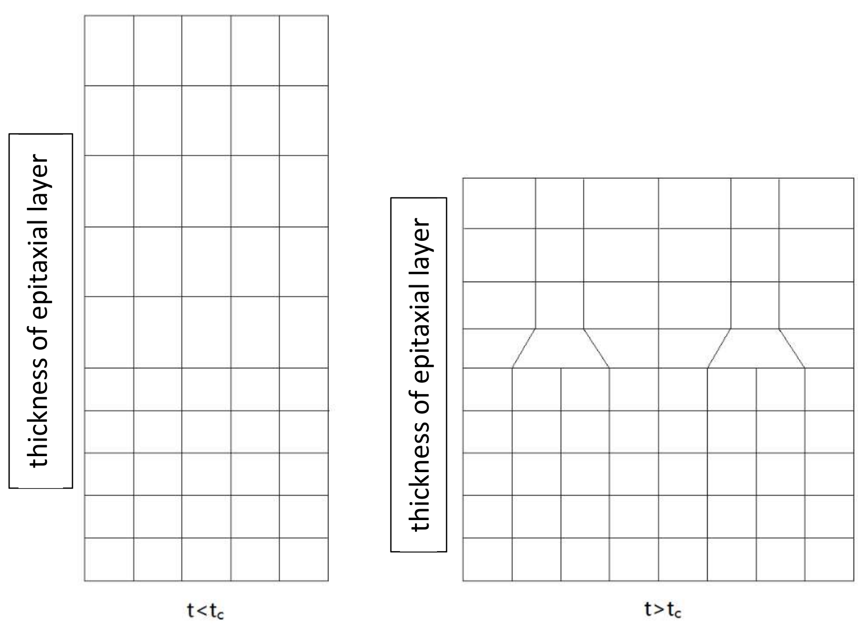

Figure 2.4: (a) shows the pseudomorphic hetero epitaxial as $t<t_c$ and (b) illustrates the misfit dislocation resultant from $t>t_c$. Adapted from [1]

The semiconductor GaAsBi has a band gap of 1 eV and exhibits a high absorption coefficient, typically around 10^4 cm^{-1} for wavelengths near the band edge at 1240 nm. According to calculations from the Matthews-Blakeslee (MB) model, the critical thickness of a GaAsBi layer with around 6% Bi on a GaAs substrate is approximately 20-30 nm.

However, this thickness is less than the ideal absorption depth (~100 nm). The absorption depth ($1/\alpha$) indicates that significant absorption occurs within the first 100 nm of the material. Despite a thickness limited to 20-30 nm due to strain considerations, the GaAsBi layer, which has a high absorption coefficient, can still effectively absorb a substantial portion of incident light near its band edge. A multiple quantum well (MQW) structure can be implemented to boost absorption further. This method, involving alternating thin GaAsBi layers with GaAs barriers, significantly increases the adequate absorption thickness without surpassing the critical thickness for each layer.

2.5 PN junction

A PN junction is one of the main principles in many electronic semiconductor device applications. The interaction between a p-type and n-type compound in semiconductor materials establishes the operation of the PN junction. Figure 2.5 shows the layout of the PN junction. Many free carrier holes are available in the p-region, and electrons in the n-region.

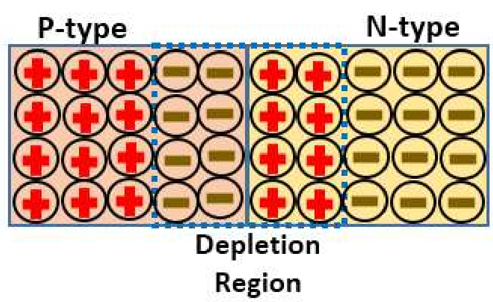

Figure 2.5: The layout of PN junction at equilibrium

When no external bias voltage is applied, some free electrons will diffuse into the p-region, leaving positive donor ions near the junction. At the same time, holes will diffuse to the n-region and leave behind negative acceptor ions near the junction. The diffusion process is due to the different concentrations in both regions. This phenomenon will create a free space region called the depletion region and establish an electric field. In addition, it creates a built-in potential caused by an electric field in the depletion region. The carriers' movement process is described based on the band diagram principle in the P-N junction, as illustrated in Figure 2.6.

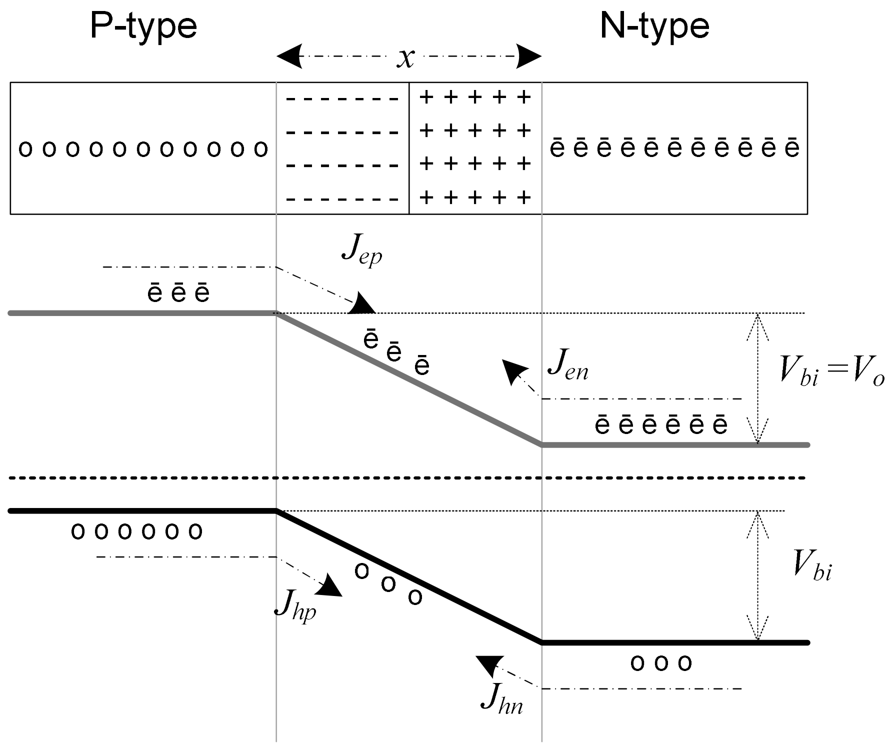

Figure 2.6: The P-N junction operation at zero bias voltage.

Figure 2.6 explains that the current flow exists in the p-n junction due to the movement of free carriers. Four essential component carriers are named majority hole, J_{hp} and minority electron, J_{ep} from the p-region; majority electron, J_{en} and minority hole, J_{hn} from the n-region. Both majority carriers, J_{en} and J_{hp} will diffuse across their opposite site to fill in the empty state in both regions. The phenomenon results in a diffusion current. When the majority of electrons (J_{en}) move to the p-region, it will leave behind positive donor charges and as the majority of the hole (J_{hp}) moves to the n-region leaving behind negative accepter charges. As the diffusion continued, it built an electric field across the junction. The electric field's direction is from the n-type to the p-type region. This electric file allows the minority carriers, J_{hn} and J_{ep} drift to the opposite region, creating a drift current that will cancel out the diffusion current. These movement of currents will continue until reaches equilibrium condition where there is no net current. It means the diffusion current is equal to the drift current.

A Forward bias is when an external voltage is applied across the PN junction to overcome the equilibrium condition. The positive terminal of the bias will connect to the p-type, and the negative terminal will be connected to the n-type. At forward bias, the applied voltage must be larger than the built-in potential voltage in the depletion region. It will reduce the built-in potential and make the depletion region narrower. This condition will allow more majority carriers to flow across the junction. As a result, creating more diffusion current [15] and become dominant in the diode current. Therefore, the drift current is no more equal to the diffusion current.

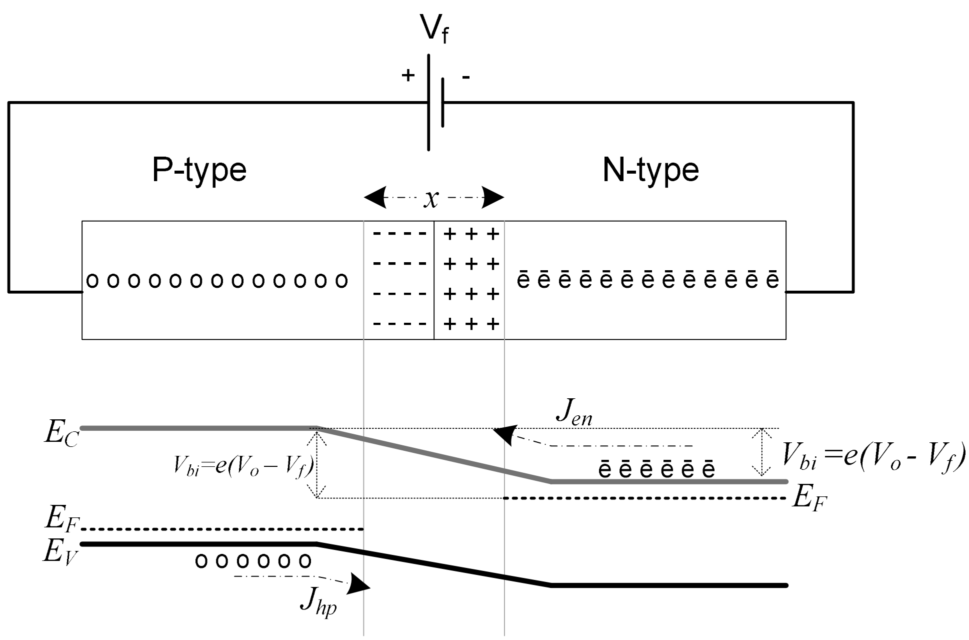

Figure 2.7: The P-N junction operation at forward bias voltage.

In contrast, if the external voltage is applied in reverse bias, the depletion region will rise broader. It is because the applied voltage increases the built-in potential. It will limit the majority carrier to diffuse to the opposite region. As a result, no diffusion current will be flowing across the junction. There will be a small number of minority carriers swept away by the electric field, creating a small current called reverse saturation current. The PN junction will act like an insulator in the circuit. The applied reverse voltage should be within a specific limit to avoid reverse breakdown voltage. If the particular limit is exceeded, then the depletion region at the junction will break down, resulting in a very high current flowing across the junction. This situation makes the PN device get overheated and damaged. Figure 2.8 shows the reverse bias connection on the PN junction.

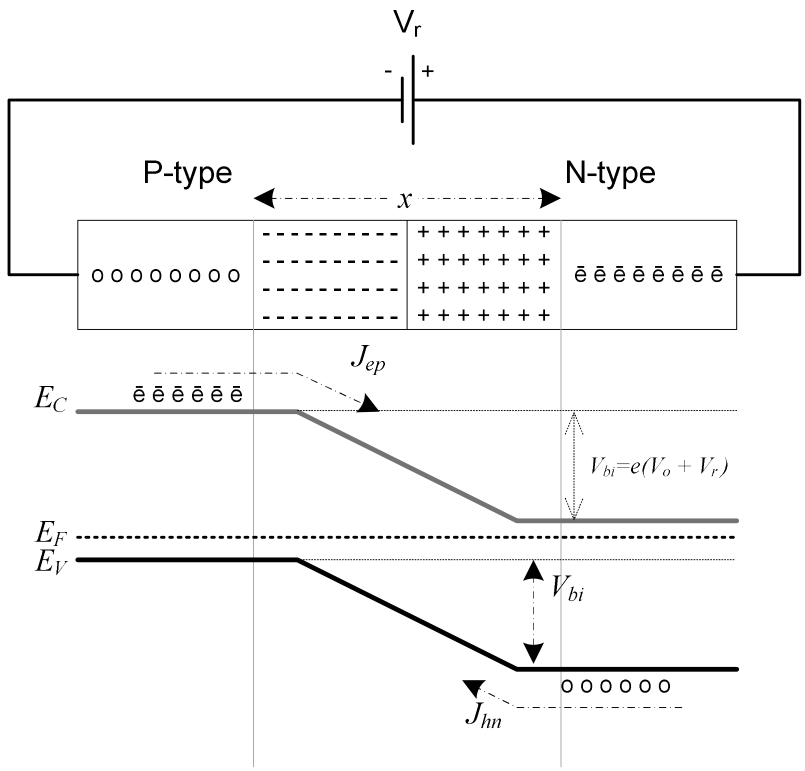

Figure 2.8: The P-N junction operation at reverse bias voltage.

2.6 Absorption of light in the diode

In the solar cell working principle, the generation of electrical energy from the absorption of sunlight is based on a phenomenon referred to as the photovoltaic effect. Generally, when semiconductor materials are illuminated by light, the energy from the light particles called photons is absorbed or transparent depending on the band gap of the diode's material. If the energy of the photons is higher than the material's band gap, it will generate free electron-hole pair carriers. The free electron will get excited to the conduction band at a sufficient amount of energy absorbed from the photons, leaving behind a hole in the valence band. Then, the light-generated carriers are swept away across the i-region. The current will be collected during the presence of the electric field. For the absorption process in the i-region, the carriers from both p and n regions will diffuse into the i-region before they are swept away and create current. Figure 2.9 demonstrates the collection of generated electron-hole pairs from the absorption of a photon in the p-i-n diode.

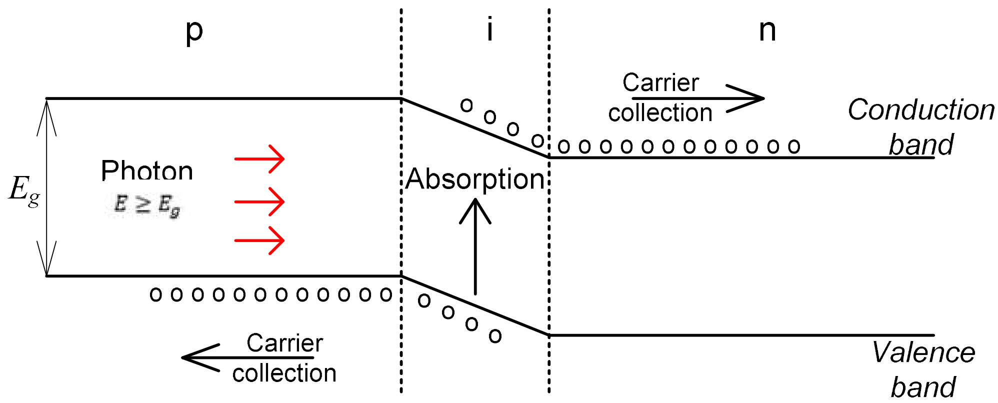

Figure 2.9: The collection of generated electron-hole pairs from absorption of photon in the i-region of p-i-n diode

Besides this phenomenon, other conditions exist due to the relationship between the photon and band gap energy. For instance, if the photon energy is less than the band gap of the device, then no electron will be excited to the conduction band. However, if the photon energy is much higher than the band gap, the electron will get thermalised at the band edge, and the energy will be converted to thermal energy and become thermal loss

The absorption coefficient measures the absorption of light that travels into the diode, α. This parameter determines that a given thickness of the material will absorb the light at the corresponding wavelength. Each material has a different value of α. If the absorption coefficient value is high, it means strong absorption by the diode. Figure 2.10 illustrate the α value for different semiconductor material measured at room temperature. Each semiconductor's absorption coefficient has a sharp edge. It is because when the light travels beyond the material cut-off wavelength, the absorption will decrease abruptly, and after a longer wavelength, the light becomes transparent to the diode.

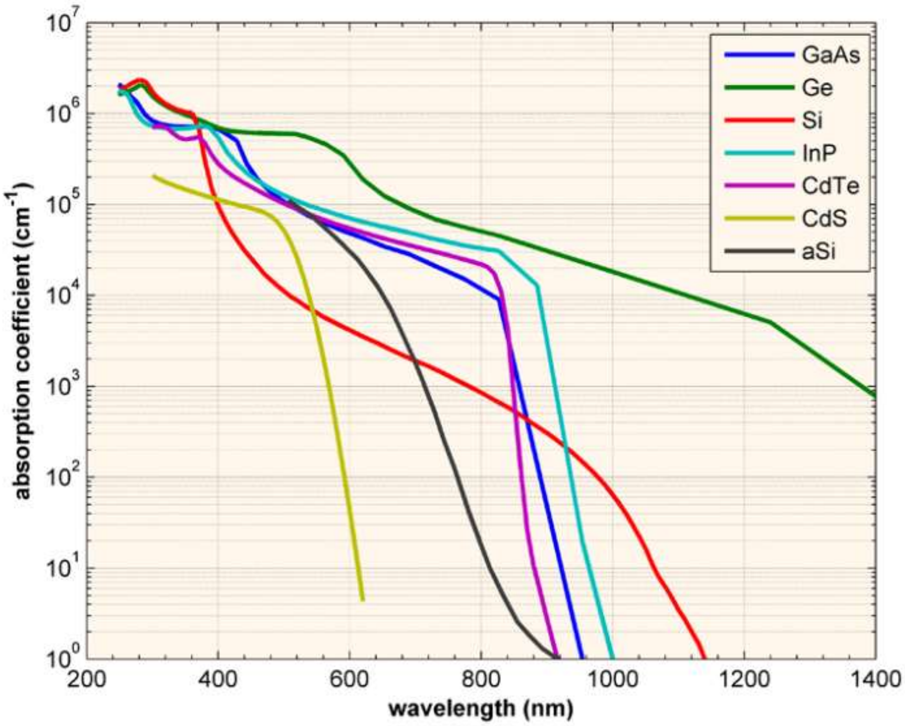

Figure 2.10: The absorption coefficient for several materials such as; GaAS, Ge, Si and other compounds.

The diagram is adapted from source [16]

2.7 I-V characteristics of the single solar cell model.

The incident photons from light energy create the light-generated charge carriers, also known as electron-hole pairs. The PN junction collects and separates these charges, allowing current to flow in the external circuit. A solar cell can be modeled as a basic single-diode model, as shown in Figure 2.11. A current source, I_{ph}, represents the photo-generated current. Part of that current flows through the forward-biased diode, while the remaining current flows into the external circuit. The model also includes parasitic resistances, such as the shunt resistance, Rsh representing the leakage current, and the series resistance; Rs indicates the physical resistance in the contacts and the semiconductor layers. Therefore, the final external current (I) is described in Equation 2.8

$$I = I_{ph} - I_d - I_{R_{sh}} \tag{2.8}$$

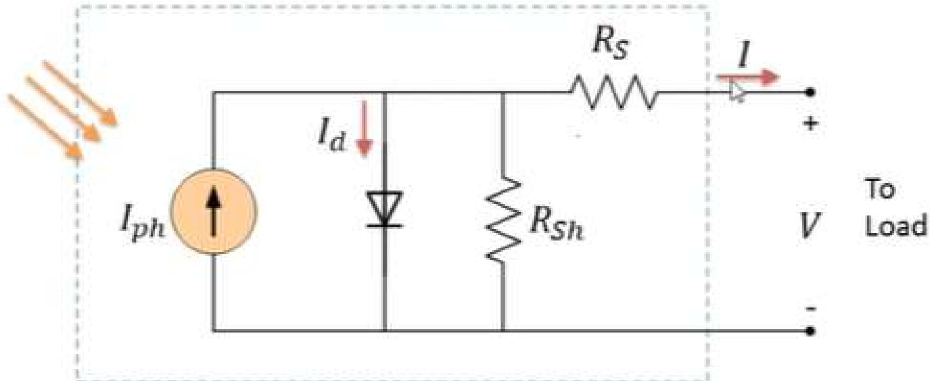

Figure 2.11: Single diode model for solar cell

The diagram is adapted from source [16]

The diode current, I_d is given by the Shockley diode expression as in equation 2.9

$$I_d = I_0 \left[\exp\left(\frac{q(V+IR_S)}{nk_BT} - 1\right)\right] \tag{2.9}$$

As a result, the total external current becomes to the total photo current, I_{ph} subtracts the diode current, I_d and the current through the shunt resistance as described in Equation 2.10.

$$I = I_{ph} - I_0 \left[\exp\left(\frac{q(V+IR_S)}{nk_BT} - 1\right)\right] - \left(\frac{(V+IR_S)}{R_{sh}}\right) \tag{2.10}$$

The others parameters are described as below;

I_0	Dark saturation current
q	Electron charge
k	Boltzmann constant
T	temperature
n	Ideality factor

The I-V characteristics consist of the short-circuit current and open-circuit voltage, which are determined from the graphical representation of Equation 2.10. In practical measurements, the external voltage is systematically swept from zero to a maximum value, and at each voltage, the corresponding external current is meticulously measured. These two key values form the I-V characteristic of this solar cell device.

The forward bias operation is essential in the I-V curve characteristic of the diode current. If the measured forward I-V is a low value close to zero, it indicates the saturation current of the diode. This implies that the diode junction is not receiving any light. At this point, the diode current is also referred to as dark current, and its value is temperature-dependent as the forward voltage increases. When the voltage exceeds the built-in-in potential of the junction, the diode current will rise exponentially. Therefore, the I-V characteristic of no light current closely resembles the behavior of the diode's current in the negative sign ($-I_d$).

The I-V characteristic is also use to describe the photocurrent (I_{ph}) during light illumination. The external current will follow Equation 2.10. The dark current will increase due to the generated photocurrent. Since the irradiance goes further, the total current increases higher. The maximum irradiance will determine the maximum I-V plot. The maximum current produced at zero voltage is called a short-circuit current. The forward bias voltage in the I-V plot at zero current will determine the open-circuit voltage. The temperature of the solar cell also influences both parameters. In principle, the temperature changes affect the open circuit voltage more than the short-circuit behavior.

In addition to the short-circuit current and open-circuit voltage, the I-V characteristic plot can be used to determine the fill factor (FF) parameter. The maximum power of solar cells can be estimated based on the total photocurrent at different biases. This maximum operating power occurs at the maximum short circuit current, *IMP*, and open circuit voltage, *VMP*. These results are used to determine the fill factor. The Fill factor (FF) is the ratio between the maximum power output of the solar cell to the product of its short circuit current and open circuit voltage.

Mathematically, the fill factor of the solar cell is formulated as follows;

$$FF = \frac{I_{MP} \times V_{MP}}{I_{SC} \times V_{OC}} \tag{2.11}$$

Understanding the fill factor (FF) concept is crucial for maximizing solar cell efficiency. The fill factor plays a critical role in determining a solar cell's maximum power output. It is determined by dividing the maximum power output by the product of its open-circuit voltage (Voc) and short-circuit current (Isc) [16]. Optimizing the fill factor of solar cells can ensure the highest possible power output, increasing energy harvesting from the sun and producing sustainable green energy in the future.

The maximum power output of a solar cell is visualized through the I-V characteristic graph. This graph is constructed by multiplying the photocurrent, (I_{ph}) at each point of illumination with the applied bias voltage. For example, the resulting plot, shown in Figure 2.12, is crucial for identifying the peak of the maximum power, which indicates the position of the maximum short-circuit current (IMP) and open-circuit voltage (VMP). These parameters are used to determine the fill factor via Equation 2.11. Thus, the fill factor (FF) is the ratio between the maximum power from the solar cell and the product of short-circuit current and open-circuit voltage [17]. Table 2.1 provides example of necessary values for determining the fill factor.

Table 2.1: The fill factor parameters for QW20 device

MQW (QW20) GaAsBi P-i-N diode solar cell parameters			
Device	IMP (mAcm-2)	VMP (V)	FF
QW20	0.355	0.32	69.04%

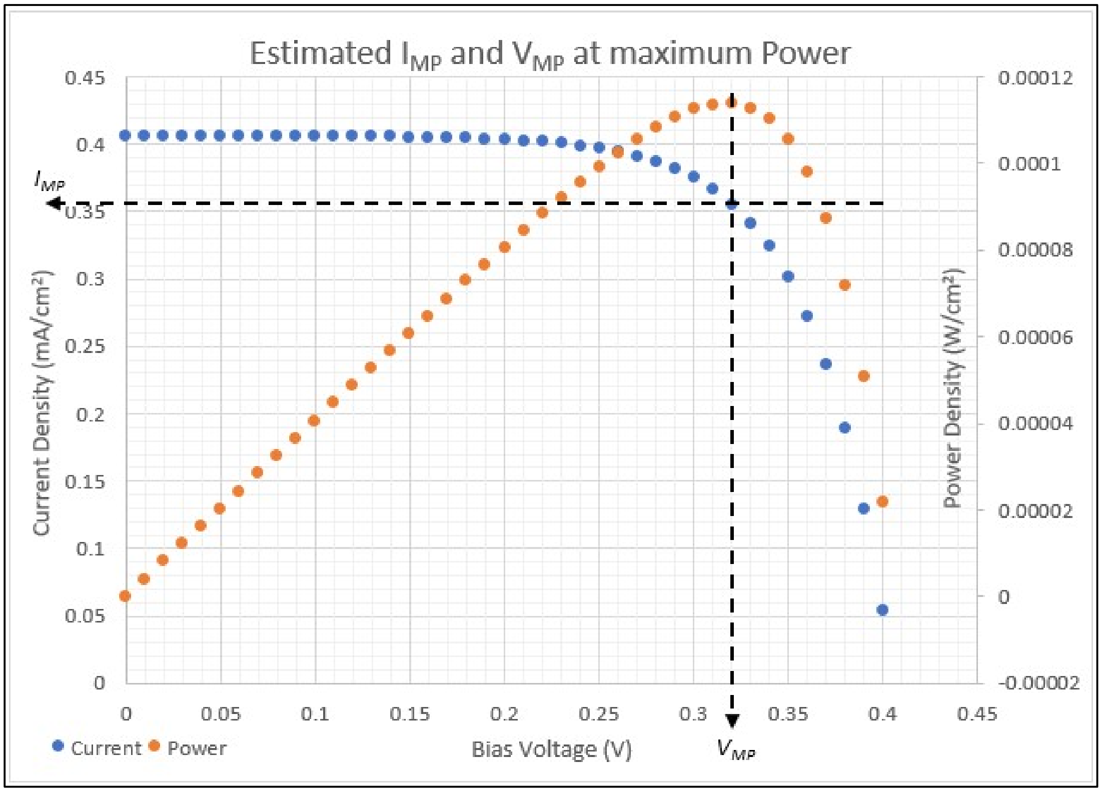

Figure 2.12: The estimated IMP and VMP at maximum operating power

References

[1] B.G Streetman, S.K. Banerjee, "Solid State Electronic Devices", Sixth Edition, 2008, Prentice-Hall of India.

[2] C.A Broderick, M. Usman, S.J. Sweeney, E.P.O Reilly, Band Engineering in dilute nitride and bismide semiconductor laser", Semiconductor Science and Technology. 27 (2012), 094011 (14pp)

[3] B. Royall, H. Khalil, S. Mazzucato, A. Erol, N. Balkan, "Experimental investigation and numerical modelling of photocurrent oscillations in lattice matched $Ga_{1-x}In_xAs_{1-y}$/GaAs quantum well p-i-n photodiodes", Nonascale research Letters (2014), 9:84, Springer Open Journal.

[4] H.M. Khalil, N. Balkan, "Carrier trapping and escape times in p-i-n GaInNAs MQW structures", Nonascale research Letters (2014), 9:21, Springer Open Journal.

[5] C.J Hunter, F. Bastiman, A.R. Mohmaf, R.D. Richards, et. Al, "Absorption characteristic of GaAs/$GaAs_{1-x}Bi_x$ diodes in the near-infrared", IEEE Photonics Technology Letters, Vol. 24, No. 23, 2012, IEEE.

[6] I. Vurgaftman, J. R. Meyer, and L. R. Ram-Mohan, "Band parameters for III-V compound semiconductors and their alloys," (in English), Journal of Applied Physics, Review vol. 89, no. 11, pp. 5815-5875, Jun 2001, doi: 10.1063/1.1368156

[7] J. A. Vanvechten and T. K. Bergstresser, "ELECTRONIC STRUCTURES OF SEMICONDUCTOR ALLOYS," (in English), Physical Review B-Solid State, Article vol. 1, no. 8, pp. 3351-+, 1970, doi: 10.1103/PhysRevB.1.3351.

[8] E. D. Jones et al., "Band structure of InxGa1-xAs1-yNy alloys and effects of pressure," (in English), Physical Review B, Article vol. 60, no. 7, pp. 4430-4433, Aug 1999, doi: 10.1103/PhysRevB.60.4430.

[9] S. H. Wei and A. Zunger, "Predicted band-gap pressure coefficients of all diamond and zinc-blende semiconductors: Chemical trends," (in English), Physical Review B, Article vol. 60, no. 8, pp. 5404-5411, Aug 1999, doi: 10.1103/PhysRevB.60.5404.

[10] M. Usman, C.A Broderick., A. Lindsay, E.P.O' Reilly, "Tight-binding analysis of the electronic structure of dilute bismide alloys of GaP and GaAs", Physical Review B 84, 245202 (2011), The American Physical Society.

[11] S. Francoeur, M.J. Seong, A. Mascarenhas, et. al, “Band Band gap of GaAs1−xBix, 0<x<3.6\%”, Applied Physics Letters, Vol. 82, No. 22, pp. 3874-3876, 2005, AIP Publishing, doi: 10.1063/1.1581983

[12] S. Tixier, S.E Webster, E.C. Young, et. al, “Band gaps of the dilute quaternary alloys GaNxAs1−x−yBiy and Ga1−yInyNxAs1−x”, Applied Physics Letters, Vol. 86, No. 11, pp. 112113, 2003, AIP Publishing, doi: 10.1063/1.1886254

[13] K. Alberi, J. Wu, W. Walukiewicz, et. al, “Valence-band anticrossing in mismatched III-V semiconductor alloys”, Phys. Rev. B, Vol. 75, No. 4, pp. 045203, 2007, American Physical Society, doi: 10.1103/PhysRevB.75.045203

[14] A.R. B. Mohmad, "Growth and Characterisation of GaAsBi," ed: University of Sheffield; 2013, 2013.

[15] John Allison, “Electronic Engineering Semiconductor and Devices”, 1990, McGraw-Hill Book Company

[16] Sánchez-Ortiz, H. A. (2015). Design of monitoring system for photovoltaics performance verification plant in Project Las Nubes. https://core.ac.uk/download/83115980.pdf

[17] (2023). DEVELOPMENT OF ROLL-TO-ROLL SLOT DIE COATED PEROVSKITE SOLAR CELLS. https://doi.org/10.23889/SUthesis.63628

[18] https://www.pveducation.org/pvcdrom/pn-junctions/absorption-coefficient

Chapter 3

Experimental setup and methodology

This chapter explains the experimental set-up, the equipment and the technology used in the measurement during the research. There are three main experiments involved in the studies. Firstly, temperature-dependent dark current analysis on bulk p-i-n GaAsBi diode and MQW p-i-n GaAsBi. Next, is the photocurrent measurement on the MQW p-i-n GaAsBi devices at different temperatures. Third, is the I-V measurement on the QW20 p-i-n GaAsBi diode at low temperatures.

3.1 Introduction to Molecular Beam Epitaxy (MBE) operation

Molecular beam epitaxy (MBE) is an epitaxy deposition technique for developing a thin layer of single crystal-structure material. It deposits molecular or atomic beams on a heated substrate under ultra-high vacuum conditions. In 1960, J.R. Arthur and Alfred Y. Cho invented MBE technology at the Bell Telephone Laboratories [1]. It is widely used in manufacturing semiconductor materials and optoelectronic devices [2]. Figure 3.1 shows an example of the MBE layout and several standard components attached to the MBE machine.

The operation in Molecular beam epitaxy must occur in a high or ultra-high vacuum chamber. The entire thing, the substrate and the crucible source elements are enclosed in a stainless steel chamber that would get vacuum levels of 10×10^{-10} and up to 10 to 10×10^{-11} Torr. This high vacuum level in the chamber is obtained using several vacuum pumps to reach different pressure ranges effectively. Those pumps are, for instance, turbo-molecular pumps supported by ion and diffusion pumps. It is to maintain acceptable low vacuum levels and remove light air gas molecules such as hydrogen in the growth chamber. This is important to minimise impurities and other air gas molecules colliding with the required evaporated molecule as they travel to the target surface. Furthermore, a high vacuum level reduces contamination and creates a mean-free path for the evaporated molecules to travel to the substrate surface.

The sources that will supply those elements are the evaporation crucibles known as the Knudsen or effusion cells. In this method, the material to be deposited is heated in an effusion evaporator cell. It then diffuses out of the cell and heads towards the target surface on the substrate. Once the molecule atom hits that surface, it will either stick to the substrate surface or bounce around, reacting with the surface and then sticking to it. This method can develop a thin film because the molecules come out of the effusion cell in a beam, and the rate at which the molecules are emitted from the evaporator cell can be controlled precisely by controlling its temperature. Moreover, the deposition rate is an essential criterion in MBE that allows the films to grow epitaxially. These deposition rates require a high vacuum condition to achieve the same impurity levels as other deposition techniques [3-4].

During the growing operation, reflection high energy electron diffraction (RHEED) is regularly used to monitor the growth of the crystal layers [5]. The shutters in front of each furnace are controlled to build a specific thickness of each layer for a single layer of atoms. Intricate structures of layers of different materials, such as developing AlGaAs and GaAsBi alloy, can be fabricated using this mechanism. This control has allowed the development of more complex hetero-epitaxy structures where the electrons can be confined in space, giving quantum wells or even quantum dots. Such layers are now critical for many modern semiconductor devices applications, including semiconductor lasers and light-emitting diodes.

MBE is famous for its controlled material evaporation, facilitating high-range temperature mobility and fewer defects [6]. However, the growth process requires a longer duration. Figure 3.1 shows an example of the MBE layout and several standard components attached to the MBE machine. However, this is not the exact illustration of the MBE machine used during the project to grow GaAsBi alloy.

In this research study, the experimental work does not directly involve growing GaAsBi material. This was due to several technical issues and limitations during the research study. The bulk GaAsBi p-i-n diodes were grown by Dr Tom Rockett, and MQW GaAsBi p-i-n diodes were grown by Dr Robert D. Richard. Both researchers have given the courtesy to use and perform further analysis on the devices. All devices were grown using an MBE-STM machine in The University of Sheffield's MBE laboratory.

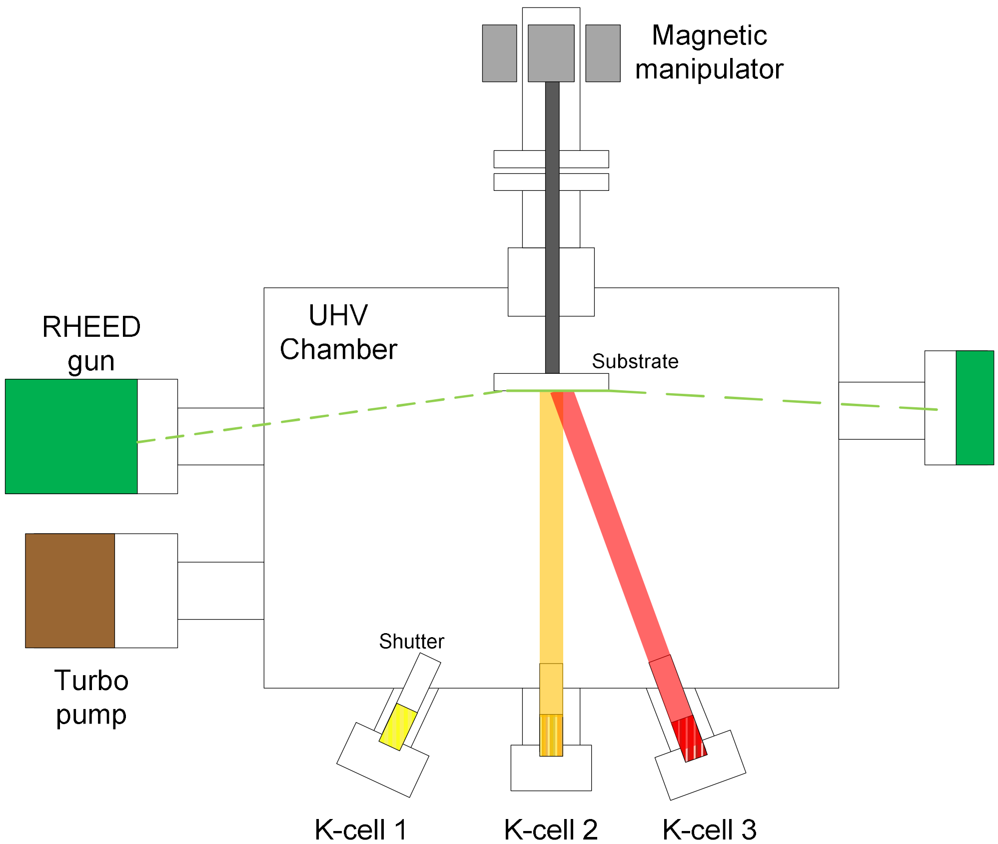

Figure 3.1: MBE machine technology. Adapted from [7]

3.2 Devices structure

During the temperature-dependent electrical characterization, two sets of devices are used. The first set consists of two bulk p-i-n diodes that utilize different growth strategies. One series, called Tgrow, involves creating bismide composition at different temperatures but using the same Bismide flux constant at 10.6×10^{-8} mBar. The second series, FBi, involves configuring the bismide based on various bismide flux arrangements but keeping the growth temperature constant at 375°C.

The second set is a series of multiple quantum wells GaAsBi p-i-n devices that were grown in an n-type GaAs substrate. Both sets of devices are used in the temperature-dependent dark current measurement, and the results are discussed in Chapter 4. The temperature-dependent I-V photocurrent measurement only involves MQW GaAsBi p-i-n diodes, as discussed in Chapter 5.

3.2.1 Bulk GaAsBi p-i-n diodes structure

The bulk GaAsBi p-i-n diodes are grown on the n-type GaAs (001) substrate with 300 nm n-type GaAs buffer. Then, a 100 nm GaAsBi bulk layer was grown as the i-region of the p-i-n diodes. The GaAsBi's thickness is design to have 100 nm thin is because to prevent from strain relaxation effect that possibly obscure the characterization analysis. After that, another 10 nm un-doped GaAs thin layer was grown on the top of the GaAsBi i-region, followed by a 300 nm p-type GaAs layer. This type of structure was applied for both series of GaAsBi p-i-n diodes.

The n and p-type layers, with a thickness of 300 nm, were grown at 577 °C using As2 [11]. The dopant concentrations used were 2×10^{18} cm^{-3} for the n-type layer and 4×10^{18} cm^{-3} for the p-type layer. To avoid the desorption of arsenic from roughening the surface of the device, the ratio of As: Ga atomic flux is almost about 1.6:1. The growth rate of GaAs is 0.60 ± 0.01 ML/s. It was measured after depositing the n-type layer using the RHEED oscillation mechanism. The gallium cell temperature was carefully regulated for a 0.60 ± 0.01 ML/s growth rate. The GaAsBi growth process began after allowing the substrate and the As cracker to cool for about 20 min period. Throughout the development of the GaAsBi layer, growth parameters such as substrate temperature, Bismide beam equivalent pressure (BEP), and Bismide growth temperature were systematically varied. The devices were fabricated into an annular mesa p-i-n diode with a standard back contact [8].

The device structure is illustrated in Figure 3.2. The only dissimilarity between the series of devices is about incorporating bismuth composition. The various bismuth content in Tgrow series is based on different GaAsBi growth temperatures, and the FBi series is based on different bismuth flux applied during the i-region growth. The information on GaAsBi temperature growth and bismuth composition for both series are described in Table 3.1. The details of the growth parameters are recorded in [8].

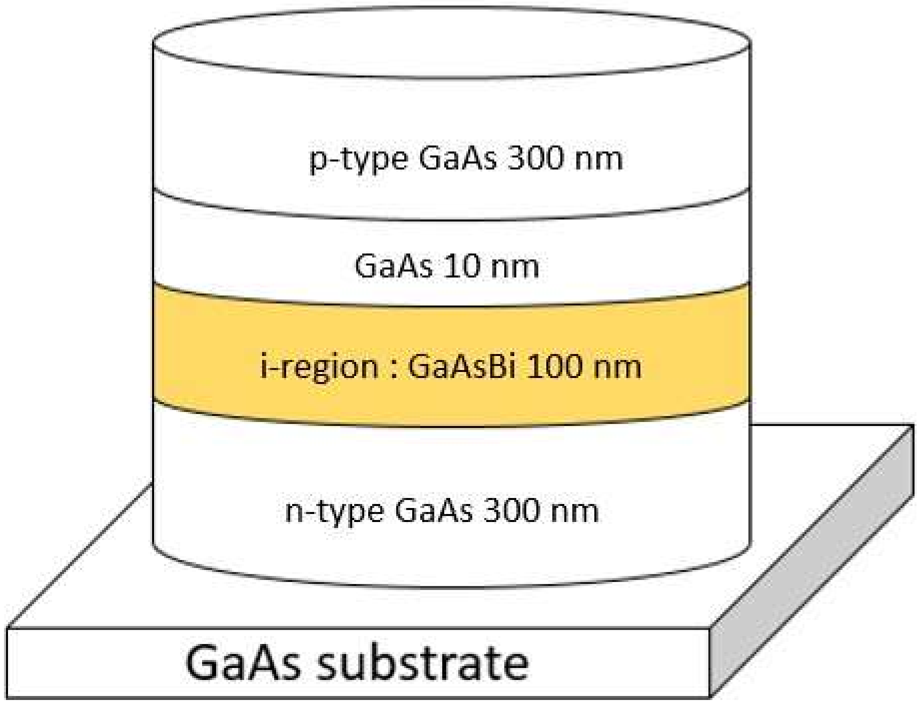

Figure 3.2: The structure of bulk GaAsBi p-i-n diodes for both Tgrow and FBi series. The illustration and information are adapted from [8]

Table 3.1: Growth temperature and bismide content information of the GaAsBi p-i-n devices which been used in the experimental work.

Series	**Tgrow (°C)**	**FBi (× 10-7 mBar)**	**[Bi] (%) from XRD [8]**	**Eg (eV) inferred from [Bi] following [9]**
Tgrow	355	1.06	3.5	1.16
	405	1.06	1.4	1.31
FBi	375	0.50	1.3	1.31
	375	2.12	5.4	1.05

3.2.2 MQW GaAsBi p-i-n diodes structure

The other set of devices used during temperature-dependent measurement is MQW GaAsBi p-i-n diodes. In previous work, a series of multiple quantum wells devices were grown in n-type GaAs substrate; with 200 nm n-type GaAs buffer; 200 nm n-type Al0.3Ga0.7As cladding region; about 620 nm in a total of MQW intrinsic region; followed by 600 nm p-type Al0.3Ga0.7As cladding region and covered by 10 nm p-type GaAs layer. In the MQW i-region, the nominal thickness of GaAsBi in every sample is 8 nm sandwiched by the number of GaAs barrier thicknesses. The structure of the devices is shown in Figure 3.3. The details of the growth parameters are recorded in [10].

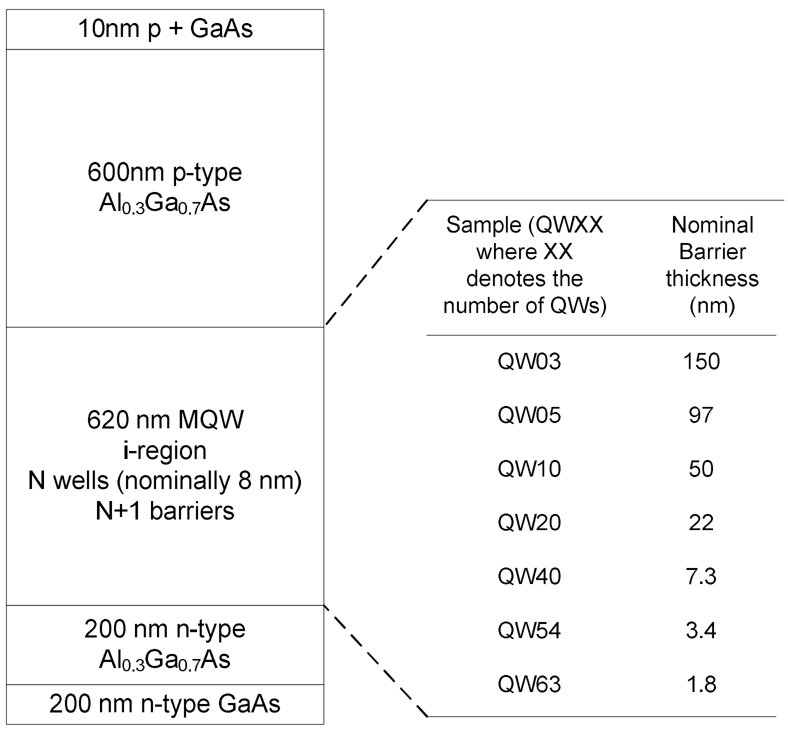

Figure 3.3: The structure of MQW series GaAsBi p-i-n diode.

The diagram is adapted from [10]

The n-type GaAs buffer layer with a thickness of 200 nm was grown at 580 °C with a meticulously controlled growth rate of 0.55 mm/h. The same growth temperature was applied for the n-type AlGaAs cladding using a similar Ga flux of 3.44 atoms nm^{-2} s^{-1}, and also the Al and As2 flux were 1.47 atoms nm^{-2} s^{-1} and 7 atoms nm^{-2} s^{-1} respectively to produce $Al_{0.3}Ga_{0.7}As$. Prior to the growth of the MQW region, the sample was allowed to cool down to 380 °C, and the arsenic cracker cooled down from 1000 °C to 650 °C to prepare As_4 for the growth of the MQW layer. Before growing the first GaAsBi well, a Bismide pre-layer was constructed on the growth surface. The quantum well layer thickness in every sample was kept at 8nm. The series of MQW p-i-n diodes differ in terms of the number of wells and barriers. However, the whole i-region for all samples is designed at 620 nm, and each number of wells is kept fixed at 8 nm. Therefore, Only GaAs barrier thickness varies accordingly to maintain the whole i-region structure at 620nm.

A standard photolithography process and wet etching are implemented to fabricate GaAsBi MQW p-i-n diodes in the form of circular mesa diodes with several radii up to 200 µm. The back contact was made using In/Ge/Au, and the top contact was made using Au/Zn/Au.

In developing the GaAsBi MWQ p-i-n diode, AlGaAs cladding is introduced at the top and bottom layers of the MQW i-region. Including AlGaAs cladding layers in GaAsBi devices can significantly improve light absorption and overall device performance. The primary purpose is to help confine electron and hole carriers within the active region by creating a potential barrier. It also enhances the confinement optical mode, ensuring more light interacts with the active region, thus improving absorption and emission efficiencies.

AlGaAs, with its larger band gap compared to GaAsBi, serves a crucial role in creating a potential barrier for both electrons and holes. This barrier effectively confines them within the GaAsBi layer, significantly reducing carrier leakage out of the active region. The increased carrier density within the GaAsBi layer enhances the probability of radiative recombination, thereby improving photoluminescence efficiency.

Furthermore, AlGaAs cladding layers have a lower refractive index compared to GaAsBi. These refractive index differences create an optical waveguide effect, a phenomenon where light is confined within a particular region due to differences in refractive indices. This effect confines more light within the GaAsBi layer. Improved optical confinement ensures that more incident light is absorbed within the GaAsBi layer, enhancing the overall absorption efficiency.

3.3 Temperature-dependent dark current-volatge (I-V) measurement

Dark current-voltage (I-V) measurement is frequently used to investigate the behaviour of solar cells before illumination under a light source. This measurement enables to analyse of the fundamental of the device's electrical properties, such as saturation current, series resistance, ideality factor and shunt resistor. The characteristic of the dark current performance will determine the quality of the fabricated solar cell and follow the behaviour of the diode working principle [11]. In addition, the electrical properties from the dark current are evaluated as temperature-dependent.

The temperature-dependent dark I-V was measured using the experimental setup, as shown in Figure 3.4. The measurement is performed in a controlled dark room where all light is switch-off, and a wide thick black cloth fully covers the setup. Each GaAsBi p-i-n diode involved in this measurement is placed directly on a copper heater stage, and both items are set on the probe station. The stage's temperature is increased from room temperature at 22 C to 120 C. The dark current is measured at 22 °C, then 40 °C, followed by 60 °C, 80 °C, and 100 °C and ends at 120 °C. Figure 3.5 illustrates the setup for heating the heater stage.

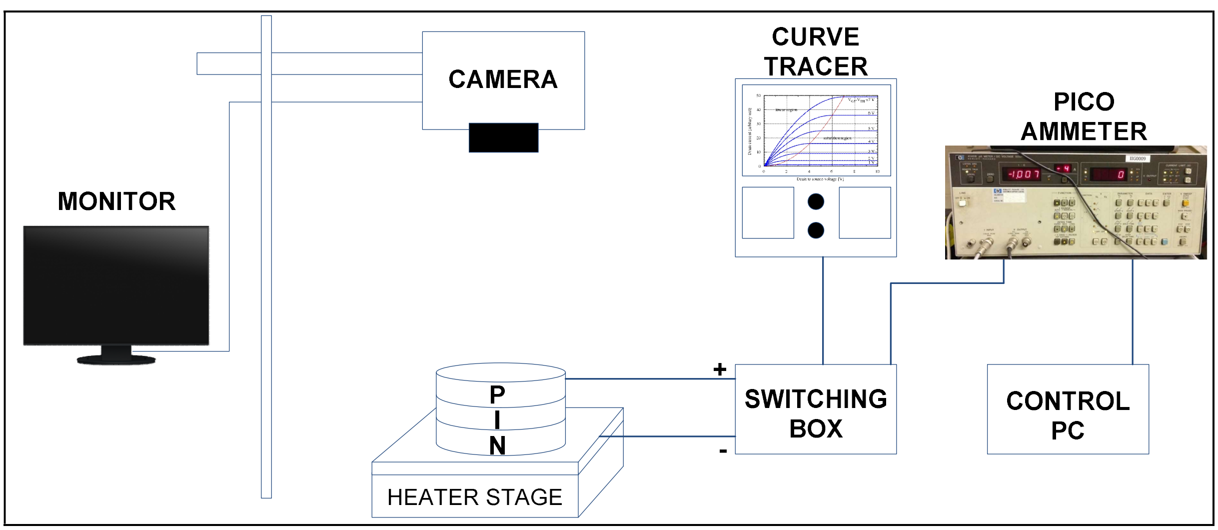

Figure 3.4: The layout for temperature-dependent dark current-voltage measurement. The setup is covered using a thick black curtain, and the experiment is conducted in a dark control room.

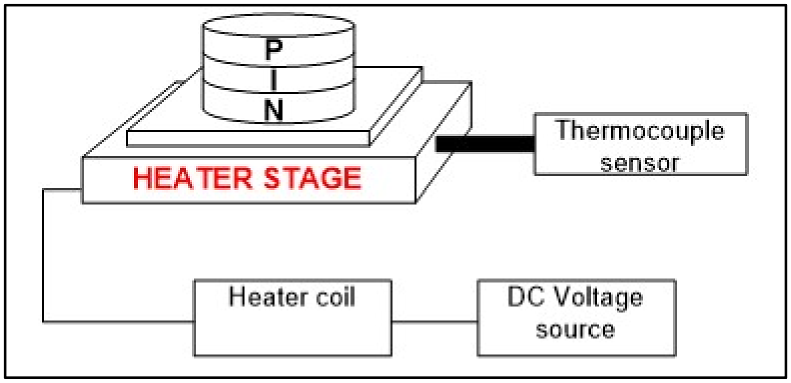

Figure 3.5: The arrangement of heating the heater stage for temperature-dependent dark current-voltage measurement.

Figure 3.5 shows that in the heater stage, a copper block is heated using a heater coil by adjusting the amount of DC voltage source. The temperature increases proportionally with the increment of DC voltage. The thermocouple sensor measures the temperature of the heater stage. During this experiment, it is assumed that at each measured temperature, the heat distribution on the heater stage surface is uniformly consistent, heating the same temperature on the p-i-n diode. Therefore, the temperature shown on the thermocouple sensor is the device's current temperature.

One fabricated sample of GaAsBi p-i-n device contained several diodes with different size mesa 200, 100 and 50 µm radius. The camera is used to select and probe the diode. All three radius-sized mesa diodes are measured to determine the current densities of the device. From the current density, it will verify that the current behaviour is dominated by the bulk current when different radius sizes are aligned together. If the current density is dissimilar, it indicates an edge leakage current produced from a small resistive area at the mesa edge. The lowest dark current density will be selected to perform the actual measurement.

A Hewlett-Packard HP4140B pico-ammeter is used to measure forward bias dark current I-V. The pico-ammeter supplies the voltage and measures the current at each voltage bias applied to the device. It is controlled by computer software connected to a pico-ammeter using a general-purpose interface bus (GPIB) cable. The measured data will be transferred to the computer through this interface cable. The testing process is comprehensive and ensures the quality of the devices. First, measure the forward voltage bias for actual measurement and then manually check the device's performance using a curve tracer. Forward and reverse voltage are applied on the device, and the resulting I-V curve behavior is displayed on the tracer monitor. This helps to differentiate the diode condition and select the highest quality diode for actual dark current measurements. Several diodes are measured, and only the one that produces the lowest dark current is selected to perform the temperature-dependent dark current measurements. This procedure was applied to all bulk and MQW devices during the experiment. The forward dark current-voltage data is mathematically fitted using the Shockley diode equation, as shown in Equation 3.1. The parameters contained in the Shockley diode equation are obtained from the fitting process. These parameters are further analysed for temperature-dependent.

$$J = J_0 \left[exp\left(\frac{qV}{nk_BT}\right) - 1 \right] - J_L \tag{3.1}$$

Where J is the total current density, q is the charge on an electron, and V is the applied voltage bias. k_B is the Boltzmann constant. T is the temperature of the diode during measurement. J_L is the additional drift current density caused by illumination. J_0 is the saturation current density of the diode, and n is the ideality factor. The J_0, n, and J_L values are adjusted heuristically until all the fitting lines closely match the dark current measurement data. This adjustment process is carried out for each device at various temperatures. The fitting process also uses least squares method analysis to ensure that the difference between the experimental dark current and the fitting data is very close. For example, Figure 3.6 illustrates the dark current densities for GaAsBi QW20 p-i-n diodes. The symbol represents the measured dark current, and the solid line indicates the fitted dark current under 20°C (293K) and 80°C (353K) conditions. The y-axis is on a logarithmic scale, and the x-axis shows the forward bias voltage. The fitting parameters used for this estimation are detailed in Table 3.2.

Table 3.2: The Shockley diode parameter applied to determine the fitting dark current densities

T (K)	J0 ($mAcm^{-2}$)	n	J_L ($mAcm^{-2}$)
293	2.40E-05	1.89	9.89E-04
353	2.96E-03	1.82	1.71E-03

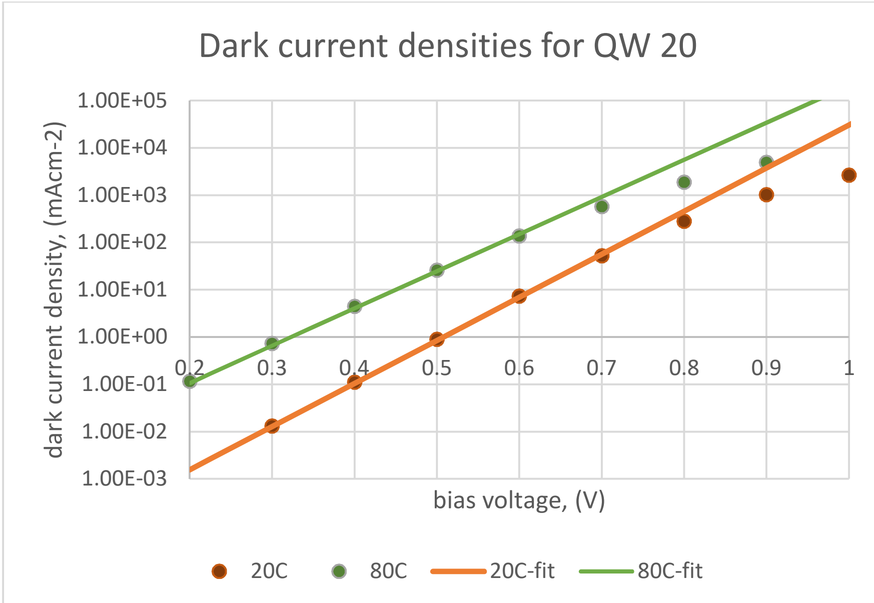

Figure 3.6: The dark current densities for GaAsBi QW20 p-i-n diodes for room temperature, (20°C) and at higher temperature (80°C).

3.4 Temperature-dependent photocurrent measurement setup

The short-circuit current and open-circuit voltage performance will be affected when the solar cell is illuminated under the concentrator. It is because the temperature of the device increases and gets hotter under the solar concentrator. Temperature-dependent photocurrent measurement is conducted to model the short-circuit current of GaAsBi p-i-n diode at high temperature under light source illumination. Furthermore, measuring photocurrent at different forward bias voltages will theoretically estimate the full illumination I-V curve at different temperatures. Thus, the device cannot identify the amount of short circuit current and open circuit voltage achieved.

The short circuit current and open circuit voltage performance will be affected when the solar cell is illuminated under the concentrator. It is because the temperature of the device increases and gets hotter under the solar concentrator. Temperature-dependent photocurrent measurement is conducted to model the short-circuit current of GaAsBi p-i-n diode at high temperature under light source illumination. Furthermore, measuring photocurrent at different forward bias voltages will theoretically estimate the full illumination I-V curve at different temperatures. Thus, the amount of short circuit current and open circuit performed by the device can be verified.

The experiment setup for temperature-dependent photocurrent measurement is depicted in Figure 3.6. This experiment uses a bright 100W white tungsten lamp as the light source. The white light is focused on the input slit of the monochromator and diffracted by a grating. In this technique, only one colour at a particular wavelength is created at a given time according to the refracting angle and transmitted through the output slit simultaneously. The spectra are recorded wavelength by wavelength. The process of dispersing white light through a monochromator and creating a spectrum of monochromatic light is controlled by software in the attached computer.

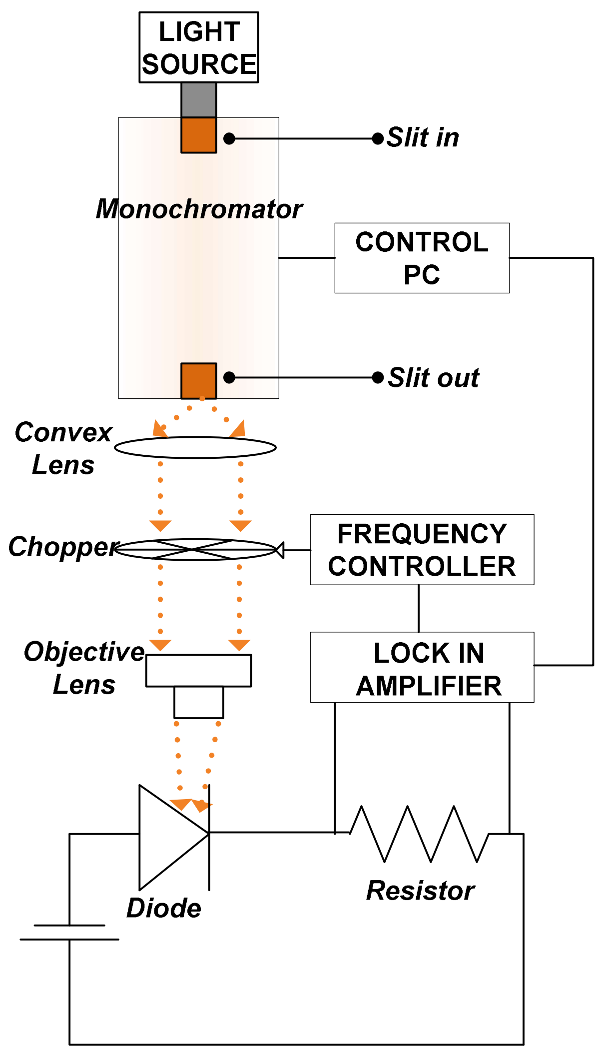

Figure 3.7: The schematic experimental set up for the photocurrent measurement at different temperature

The selected range of wavelength spectrum exit from the output slit is chopped at 180Hz. This chopping frequency is also set into the lock-in-amplifier (LIA) as the phase lock reference signal's frequency. The LIA model used in this measurement is SR 830, manufactured by Stanford Research System (SRS). The objective lens focuses the output light spectrum on illuminating the diode. The photocurrent measurement was only conducted on the selected 200 μm radius-sized mesa diode. The diode is cascaded series with a load resistor, whereas the LIA connection is parallel with the load resistor. Thus, the LIA measures only the amount of voltage across the load resistor. Since the current that flows into the diode and resistor is similar, the photocurrent can be obtained from the voltage across the resistor using Ohm's law principle. Besides, a considerable load resistor value is vital to minimise the contribution of dark current during measurement. In this measurement, the value of the load resistor is 100kΩ.

Furthermore, a polished GaAs wafer is placed below the objective lens to filter the light spectrum below 870 nm during the measurement. It ensures that the photocurrent measured in the experiment is only contributed by the absorption of photons in the i-region. The findings will be comparatively significant when measuring photocurrent on InGaAs p-i-n diode.

The advantage of the phase locking mechanism in the LIA system is that it intensifies the reading of the photocurrent signal during measurement by eliminating the effect of the noise signal and dark current. Noise signals can come from surrounding unwanted light. Therefore, setting the input and reference frequency at 180Hz will suppress the unwanted signal that could affect the photocurrent signal. Moreover, the dark current can be mitigated down to nano-amps. Thus the data obtained from this measurement is a full photocurrent signal generated by the diode. The result of the photocurrent signal is plotted according to wavelength and displayed on the control computer.

The photocurrent recorded by the computer is in arbitrary unit, which is indicated as I_{ph}. This photocurrent is a result of converting the voltage drop on the load resistor read by the LIA module. Equations 3.2 and 3.3 demonstrate the mathematical process of converting the resistor's voltage to an arbitrary photocurrent signal, I_{ph}. However, this is only a photocurrent signal and cannot be acknowledged as the definite value of photocurrent generated from the p-i-n diode. Several other mathematical processes are involved in transforming the photocurrent signal and model into actual photocurrent generated by the GaAsBi p-i-n diode.

$$LIA\ Voltage\ (V) = \frac{Output\ signal}{10} \times Sensitvity \tag{3.2}$$

$$I_{ph} = \frac{LIA\ Voltage}{0.45 \times R} \tag{3.3}$$

Where; sensitivity depends on the LIA sensitivity setting used during measurement. R is the load resistor. The factor 0.45 is the coefficient taken from the first component of the output signal in a square wave after filtered by a low-pass filter. The AC components of the output wave vanish after passing a low-pass filter. The reading display on the LIA shows the input signal V_x, as $\frac{\sqrt{2}}{\pi}V_x$. [12-13].

In this experiment, the temperature-dependent setup is conducted by placing every GaAsBi p-i-n diode sample on a copper heater stage. It is a similar approach described in Figure 3.5. The stage's temperature is increased from room temperature at 22 °C to 120 °C. The photocurrent is measured at 22 °C, then 40 °C, followed by 60 °C, 80 °C and 100 °C, and ends at 120 °C. The photocurrent measurement at each temperature is performed based on several bias voltages applied on the p-i-n diode. The bias voltage started at 0V, followed by 0.1V, 0.2V, then 0.3 V and 0.4V. The photocurrent result at every bias voltage and temperature is used to model the short-circuit current, open-circuit voltage and other solar cell parameters.

3.5 Modelling of temperature-dependent photocurrent based on illumination from monochromatic light

The result from photocurrent measurement shows a photocurrent signal due to a particular range of wavelengths. In order to determine the actual value of photocurrent illuminated by a light source require several mathematical processes. The first process is to identify the amount of power from the monochromatic light received by the p-i-n diode. This step requires the responsivity of the device, where a high responsivity value describes the device's efficiency in generating photocurrent at a given incident power. Equation 3.4 shows the responsivity formula for a particular wavelength.

$$R = \frac{I_{ph_\lambda}}{P_\lambda} \quad (A/W) \tag{3.4}$$

Where R is the responsivity, I_{ph_λ} is the photocurrent value at a specific wavelength and P_λ is the incident optical power landing on the device; in this case, is the power from the monochromatic light at each wavelength.

The procedure to obtain responsivity value is by measuring photocurrent using a commercial photodiode. An InGaAs FDGA05 commercial photodiode with an active detection area of 0.00196 cm^2 is used during the calibration process. This device has a reasonably close wavelength range with the experimental p-i-n diode. Then, based on the interpolated responsivity data provided by the manufacturer and applying Equation 3.5, the amount of monochromatic incident power that falls onto the photodiode will be determined. Equation 3.5 is deduced from Equation 3.4. In addition, Equation 3.6 is applied to obtain power density on the photodiode.

$$P_{(PD)} = \frac{I_{ph_{(PD)}}}{R_{(PD)}} \quad (A/W) \tag{3.5}$$

$$P_{(density,PD)} = \frac{P_{(PD)}}{Area_{(PD)}} \quad (W/cm^2) \tag{3.6}$$

This calibration process verifies the actual amount of power received by the measured p-i-n diode. It is because, in the case of photocurrent setup, the power of the light source is attenuated during travel through a monochromator, several lenses and mirrors with different setting angles. Therefore, to determine the optical power fall on the p-i-n diode by multiplying the power density result from Equation 3.6 with the active detection area of the measured p-i-n diode as described in Equation 3.7.

$$P_{(pin\ diode)} = P_{(density,PD)} \times Area_{(pin\ diode)} \quad (W) \tag{3.7}$$

Where, the mesa p-i-n diode's active detection area for a 200 μm radius during the experimental work is given as 0.0296 cm^2.

Next is to obtain the measured device's quantum efficiency (QE). When a photodiode is illuminated with a light source, the photon will be absorbed and create several electron-hole pairs. This generated carrier determines the current produced by the device. Therefore, the quantum efficiency is the ratio between the electron-hole pairs generated due to the number of incident photons absorbed by the device. Equation 3.8 describe the formula to determine QE. The value of quantum efficiency is calculated at every photocurrent signal wavelength.

$$QE = \frac{number\ of\ electron{-}hole\ pairs\ generated\ (in\ second)}{number\ of\ incident\ photo\ \ \ (in\ second)}\ \ (\frac{chagre/sec}{photo\ \ /sec}) \tag{3.8}$$

Aside;

$$number\ of\ electron - hole\ pairs = \frac{I_{ph}}{q} \tag{3.9}$$

$$number\ of\ incident\ photon = \frac{P_{pin\ diode}}{\hbar\nu} \tag{3.10}$$

Where; I_{ph} is the photocurrent of the measuring device, q is the electronic charge which is $(1.69 \times 10^{-19}\ Coulombs)$, $P_{pin\ diode}$ is the optical power fall onto the measured diode obtained from Equation 3.7, ħ is the reduced planks constant which is $(6.62607 \times 10^{-3}\ \ m^2 kg/s)$ and ν is the frequency of incident light.

After formulating the p-i-n diode's quantum efficiency, the following process is to determine the AM 1.5 power spectrum. It is because the solar irradiance AM 1.5 will be used to model the theoretical amount of photocurrent generated by the device upon incident power from the sunlight. In order to estimate the solar cell performance under a real sunlight spectrum, a standard AM 1.5 solar irradiance is extracted and interpolated from the NREL website. It is free and available for download [14]. Figure 3.6 shows the AM 1.5 solar irradiance.

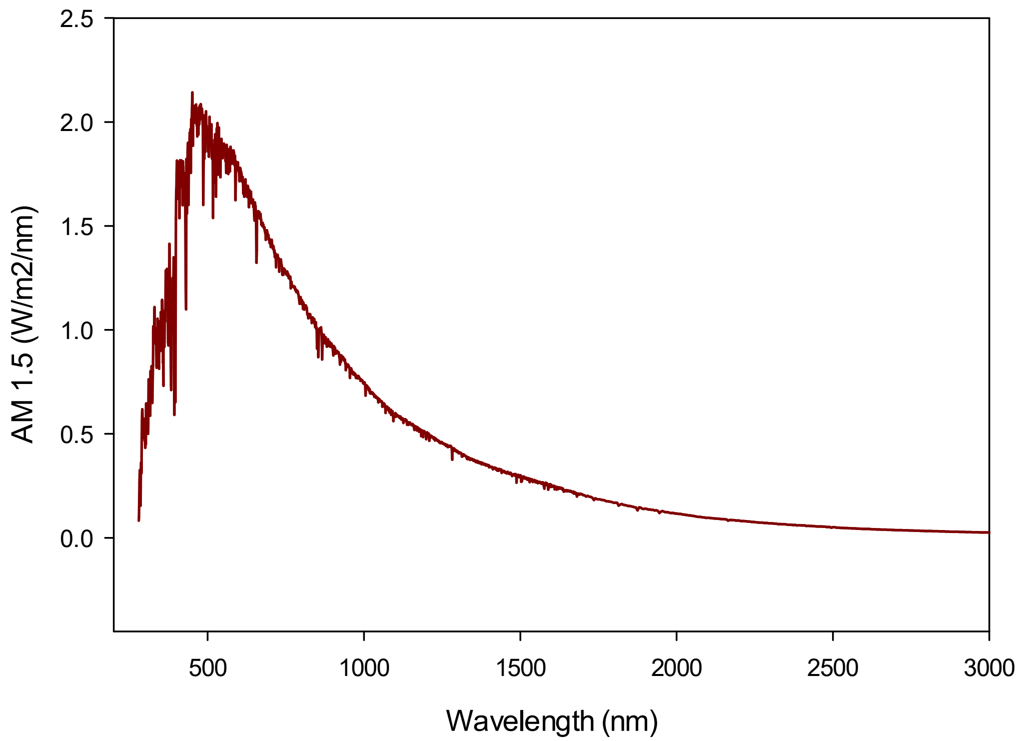

Figure 3.8: The AM 1.5 solar irradiance was adopted from [14]. The short-circuit current estimation in this experiment is based on 870 nm to 1200 nm wavelength.

Therefore, integrating a product between quantum efficiency and incident power from AM 1.5 solar irradiance enable us to estimate the number of electron-hole pair generated by the GaAsBi p-i-n diode when illuminated under sunlight. This process is shown in Equation 3.11. Then, the results will be used to model the theoretical amount of photocurrent produced by the measuring device using Equation 3.12. The photocurrent model based on Equation 3.12 is estimated for every bias voltage at every temperature-dependent measurement.

$$n_{e-h\ pairs} = \int [QE \times number\ of\ incident\ photon(AM\ 1.5)] \quad (3.11)$$

$$I_{ph,GaAsBi} = n_{e-h\ pairs} \times q \ \ (\text{Amp}) \quad (3.12)$$

3.6 Current-voltage measurement at low temperature-dependent

The third experiment is to investigate carrier trapping characteristics in GaAsBi multiple quantum well p-i-n diode. In this case, it is to study the hole-trapping effect that causes the reduction of depletion width of GaAsBi/GaAs multiple quantum well solar cells under light bias. It can be observed by looking at carrier escape time changing as a function of temperature [15]. Therefore, to demonstrate this investigation, a current-voltage measurement at low-temperature is conducted, and the experimental setup is illustrated in Figure 3.7

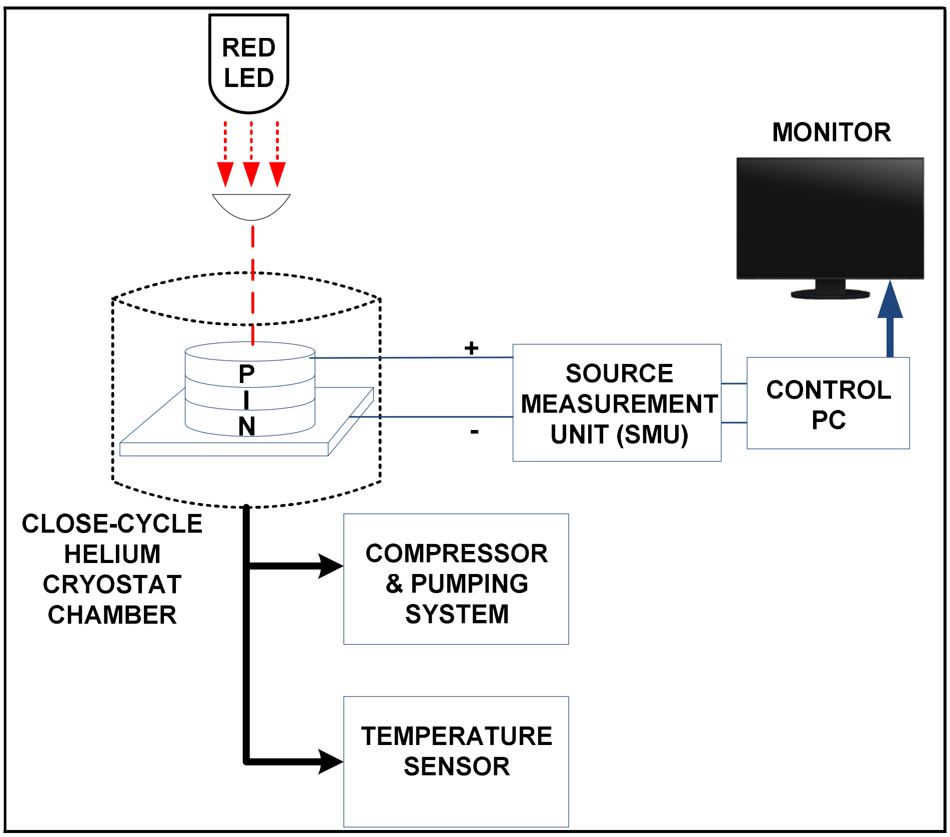

Figure 3.9: Experimental layout for low temperature current-voltage measurement under illumination of light-bias

In this experiment, the current-voltage (I-V) was measured in the dark and illumination of light from room temperature down to 15 Kelvins. The measurement is performed on one GaAsBi MQW p-i-n device known as QW20. Its structure has 20-period MQW in the i-region, consisting of 8 nm GaAsBi and 22 nm GaAs as barriers. The device was packaged in a die-bondable open package or

T05 header package. It is placed in a close-cycle Helium cryostat under vacuum conditions and illuminated by a 660 nm red LED positioned outside the cryostat set-up. A focus lens was used to concentrate the LED light on the GaAsBi MQW p-i-n diode. The red LED at 660 nm wavelength was used in this experiment to ensure minimal light absorption in the upper AlGaAs cladding layer and let the charge carriers fully excited through the i-region [15]. The chamber was built-in with a feedthrough mechanism for electrical contact, allowing current-voltage measurement [15]. A low-pressure level in the chamber was created with the help of a helium compressor, a vacuum pump and a water supply. Temperature sensors monitor the temperature changes in the close-cycle cryostat chamber. The dark and photocurrent are measured using a Keithley source measurement unit (SMU), and the data are recorded using a control computer. In addition, the electron and hole escape times were determined via Equation 3.13. Further explanation about the carrier trapping measurement and significant findings of this work were published in the article [15].

$$\frac{1}{\tau_{th}} = \frac{1}{L}\sqrt{\frac{k_B T}{2\pi m^*}} \exp\left(\frac{-(V_0(T)-E(T))}{k_B T}\right) \tag{3.13}$$

Where, τ_{th} is the meantime for the carrier to thermally escape; $V_O(T)$ and $E(T)$ are band offset and energy of bound state respectively at a given temperature; L noted as the quantum well width; m^* is the carrier effective mass, k_B is the Boltzmann constant.

References

[1] A. Y. Cho, "Film Deposition by Molecular-Beam Techniques,", Journal of Vacuum Science & Technology, Article vol. 8, no. 5, pp. S31-&, 1971, doi: 10.1116/1.1316387.

[2] Hajime Asahi; Yoshiji Horikoshi, "General Description of MBE," in Molecular Beam Epitaxy: Materials and Applications for Electronics and Optoelectronics , Wiley, 2019, pp.23-39, doi: 10.1002/9781119354987.ch2.

[3] Herman, M.A., Richter, W., Sitter, H. (2004). Molecular Beam Epitaxy. In: Epitaxy. Springer Series in MATERIALS SCIENCE, vol 62. Springer, Berlin, Heidelberg. https://doi.org/10.1007/978-3-662-07064-2_7

[4] Nunn, W., Truttmann, T.K. & Jalan, B. A review of molecular-beam epitaxy of wide bandgap complex oxide semiconductors. Journal of Materials Research 36, 4846–4864 (2021). https://doi.org/10.1557/s43578-021-00377-1

[5] Applied RHEED: Reflection High-Energy Electron Diffraction During Crystal Growth By Wolfgang Braun

[6] advantages mbe

[7] A. R. B. Mohmad, "Growth and Characterisation of GaAsBi," ed: University of Sheffield; 2013, 2013.

[8] Rockett, T.B.O., et al., Influence of growth conditions on the structural and opto-electronic quality of GaAsBi. Journal of Crystal Growth, 2017. 477: p. 139-143.

[9] Richards, R.D., et al., Molecular beam epitaxy growth of GaAsBi using As2 and As4. Journal of Crystal Growth, 2014. 390(0): p. 120-124.

[10] Richards, R.D., et al., MBE grown GaAsBi/GaAs multiple quantum well structures: Structural and optical characterization. Journal of Crystal Growth, 2015. 425: p. 237-240.

[11] D. L. King, B. R. Hansen, J. A. Kratochvil and M. A. Quintana, "Dark current-voltage measurements on photovoltaic modules as a diagnostic or manufacturing tool," *Conference Record of the Twenty Sixth IEEE Photovoltaic Specialists Conference 1997*, pp. 1125-1128, doi: 10.1109/PVSC.1997.654286.

[12] S. R. S. Inc., "Model SR830 DSP Lock-In Amplifier," ed. California, US, 1993.

[13] F. Harun, "Characterisation of GaAsBi/GaAs Multiple Quantum Wells for Photovoltaic Applications," ed: University of Sheffield; 2020, 2013.

[14] https://www.nrel.gov/pv/cell-efficiency.html
Access on 26 August 2022

[15] R.D. Richards, T.B.O. Rockett, M.R.M Nawawi, F. Harun, et al, "Light-biased IV characteristics of a GaAsBi/GaAs multiple quantum well pin diode at low temperature", Semiconductor Science Technology, Vol.33 (2018) 094008, IOP Publishing, doi: 10.1088/1361-6641/aad72a

Chapter 4

Temperature-Dependent of Dark Current-Voltage Characteristic for GaAsBi Devices

4.1 Introduction

Current-voltage (I-V) characterisation of a GaAsBi material is studied to understand the current mechanism of the device, which plays an essential role in solar cell performance. Incorporating Bismide into GaAs enables the development of a 1eV band gap device model for increasing multi-junction solar cell efficiency [1]. A key aspect of GaAsBi is large band gap reduction with increases of Bismide composition [2]. However, achieving a significant amount of Bismide fraction in GaAs host material with moderately small lattice-mismatched requires a dramatic decrease in growth temperature. A previous study has produced a very high growth of GaAsBi material in a molecular beam epitaxy (MBE) configuration, with up to 22% Bismide using low growth temperature at 200° C and relatively low As to Ga flux ratios [3]. This atypical growth temperature regime causes anti-site defects and Bi cluster [4-6]. In addition, decreasing growth temperature can lead to high carrier density defects in the band gap, thus increasing the non-radiative recombination at the band gap [7].

In the literature, few results are available to discuss the analysis of dark current voltage. Table 4.1 displays examples of GasAsBi solar cell devices with dark current-voltage measurements from different researchers. The dark current results were chosen based on different percentages of Bismide incorporation on GaAs substrate. As specified in the references, the Bismide concentration ranges from 1.31% to 5.90%. The GaAsBi layer thickness for these devices is marginally similar, except for the devices in reference [10], which have a slightly thicker layer of about 200 nm. All devices are grown by the molecular beam epitaxy technique (MBE) and developed as pin diode structure. The value of saturation current density is extracted from the dark current results in the literature by numerically fitting with the standard Shockley's diode equation.

$$J = J_0\left[exp\left(\frac{qV}{nk_BT}\right) - 1\right] - J_L.$$

The information in Table 4.1 provides a significant relationship between saturation current density (J_0) and the incorporation of Bismide. It is comparatively accepted that the saturation current density of the devices increases with a higher Bismide concentration percentage. Therefore, the critical factor in increasing dark current performance is the Bismide concentration. Moreover, some studies have demonstrated that increasing Bismide flux and lowering the growth temperature during the material growth process strongly influence the rise in dark current [9-11].

Table 4.1: Relationship of saturation current density with respect to Bismide concentration from literature.

Bismide concentration (%)	GaAsBi layer thickness (nm)	Saturation current density, J_O (mA/cm^2)	Ref
5.90	100	5.91×10^{-3}	[8]
5.37	100	5.42×10^{-4}	[9]
4.1	190±30	3.61×10^{-5}	[10]
3.4	190±30	2.70×10^{-5}	[10]
1.31	100	2.04×10^{-6}	[9]

This could affect and reduce the solar cell efficiency. One of the reasons for this phenomenon is that the increment of Bismide percentage decreases the device's carrier mobility, and its result is much lesser when compared to GaAs carrier mobility that grew under lower conventional temperatures [12-13]. However, the reduction of carrier mobility from GaAsBi is still tolerably better than the impact of the incorporation of nitride in GaAs [12]. A study also has shown that a large ideality factor of more than two was obtained for GaAsBi devices grown at 360°C. The high ideality factor describes that the current mechanism is dominated by recombination due to localized states [11].

In addition, there have been findings related to the electrical properties of optoelectronics devices incorporating a small amount of bismide. For instance, a photodiode made of InAsBi demonstrated outstanding potential for use in mid-wave infrared (MWIR) detection. A small bismide composition at 1.5% content enables an extended cut-off wavelength in the spectral region reaching up to 3.95um [14]. On the other hand, a nearly lattice-matched InGaAsBi detector grown on an InP substrate with a bismide content of 3.2% has shown promise for short-wave infrared application. The detection range for the cut-off wavelength is from 1.6um to 2.1um and exhibited promising dark current density [16].

Moreover, Z. Cao's work has focused on investigating the impact of thermal annealing after growth on the electrical properties of GaSbBi Schottky diodes. The study revealed that as the annealing ftemperature and time vary, significant improvement in device performance leads to lower dark current. At room temperature measurement, the results suggest that a GaSbBi diode with 3.5% Bismide content, annealed at 500°C for 30 minutes, exhibits good dark current behavior with ideality factor 1.3 and saturation current at 3.72 × 10-5 A [15]. Nevertheless, all of these dark current assessments were limited to comparisons of room temperature characteristics.

To date, there has been no investigation into the behavior of GaAsBi current mechanism at high temperatures. It is essential to understand how the current performance of the GaAsBi solar cell functions as temperature rises, specifically when used under concentrator application. As the temperature increases, the device's performance may change due to the alterations in its electrical properties. Therefore, this chapter studies the dark current-voltage characteristics of two series of bulk GaAsBi p-i-n diodes at temperatures ranging from 20 °C (293 K) to 120 °C (393 K). The findings are related to the diffusion and recombination-mediated current behaviors described in the Shockley diode equation. These outcomes help evaluate the impact of bismuth content and growth conditions on the dark current characteristic in GaAsBi device. Additionally, the investigation extends to analyse the performance of the dark current-voltage behavior in the GaAsBi MQW p-i-n diodes.

4.2 Experimental setup

Two series of double heterostructure GaAsBi p-i-n diodes were used to analyse the dark current mediation at different temperatures varying from 20 °C (293 K) to 120 °C (393 K). The series is Temperature Growth ($T_{grow)}$ and Bismide Flux (F_{Bi}). In the Tgrow series, the bismide composition is constructed by varying different growth temperatures. In contrast, in the F_{Bi} series, the amount of bismide composition is constructed by varying the bismide flux. All devices have an i-regions thickness approximately at 100nm and are grown using the same Molecular Beam Epitaxy (MBE) machine at The University of Sheffield but implement different growth process. Important information about the device's growth and structure is described earlier in Chapter 3, Table 3.1 and also available in reference [9].

The forward bias current-voltage (I-V) measurements were conducted during experiment using a Keithley source measure unit in a dark room. A copper heating block elevates the devices' temperature by regulating the voltage supply connected to the copper block. As the voltage increased, the temperature rose. The temperature condition is measured using a thermocouple placed within the copper block. The I-V measurement started at room temperature 20 °C, then followed by an increment of 20 °C. Thus, the other temperature-dependent applied in these measurements are 40 °C, 60 °C, 80 °C, 100 °C and 120 °C.

4.3 Analysis for Dark Current Mechanism in GaAsBi p-i-n diodes

Figure 4.1 shows the forward bias dark current-voltage results for two sets of GaAsBi p-i-n diodes under temperature-dependent measurements. The blue line represents the T_{grow} series, which was grown at the highest and lowest temperatures of 405°C and 355°C respectively. The red color, represents the (F_{Bi}) series, both grown at 375°C but with different Bismide flux configurations. The lowest Bismide flux is 0.5 × 10-7 mBar, and the highest Bismide flux is 2.12 × 10-7. The vertical axis shows the dark current-voltage density (J-V) in mAcm-2, while the horizontal axis represents the forward bias voltage ranging from 0 to 1.2 V. The marker illustrates different temperatures during measurement, and the solid line represents the fitted data obtained using the general Shockley diode equation.

Each data point represents the device's J-V (current-voltage) characteristics at different temperatures. All data demonstrated significant diode current behavior. Despite the devices being grown differently, their dark currents increased as the percentage of Bismide composition increased. The results of the dark current behavior at room temperature are consistent with those reported in the previous study [9]. Dark current results for these devices are shown in Appendix A.

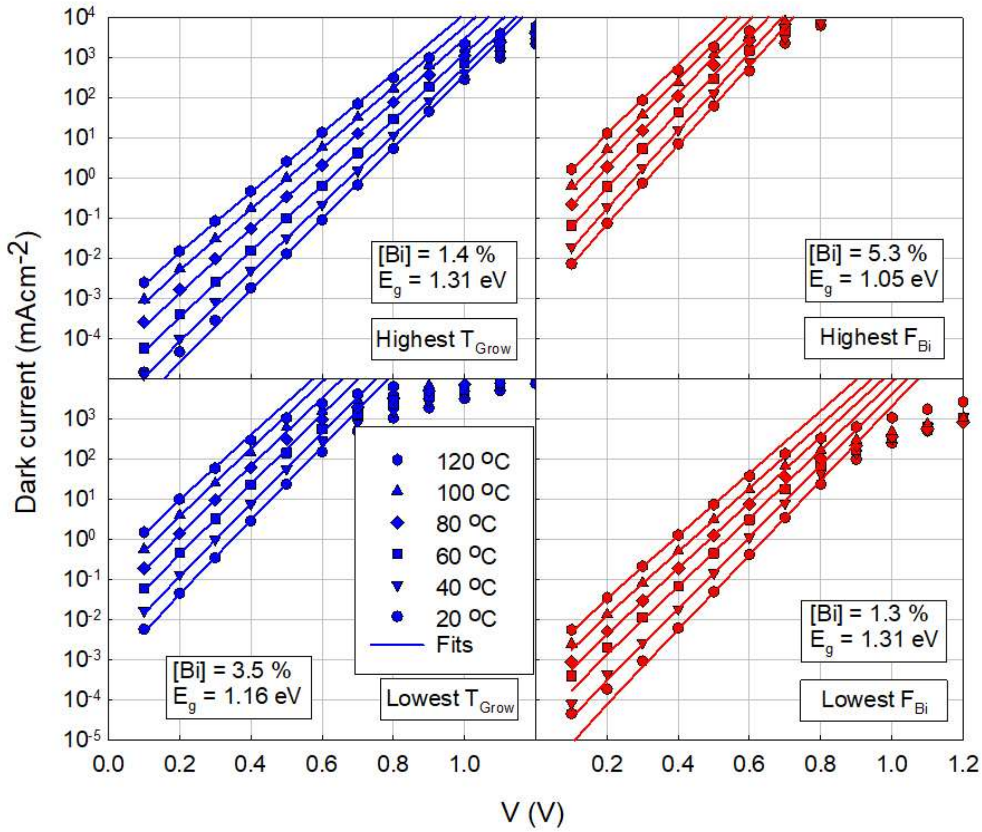

Figure 4.1: Forward bias J-V curves of the selected diodes, fitted using Equation 1. The blue color represents the diodes grown under changing growth temperatures, whereas the diodes fabricated by varying Bi flux series are illustrated in red [23].

It is reported that the dark current behavior at the forward bias during room temperature measurement demonstrates diode-like behavior, and the ideality factor is estimated at 2, which suggests that the recombination mechanism significantly influences the saturation dark current [9].

A similar trend of temperature-dependent current behavior for small Bismide percentages where their dark current density starts at 10^{-5} mAcm^{-2}. In contrast, for higher Bismide concentration the dark current density starts from around nearly order of 10^{-2} mAcm^{-2}. Furthermore, it is evident that in all devices, as the temperature increases from 300 K to 393 K, the dark current increases by more than two orders of magnitude. This indicates that as the device temperature rises above room temperature, more carriers have enough thermal energy to move from the valence band and generate a hole-pair carrier under completely unilluminated conditions.

Besides, the slope of the dark current for all devices is limited at high forward bias voltage around 0.8 to 1.0 V. This possibly shows the effect of series resistance in the roll-over of diode's dark current characteristic above 0.8 V. The series resistance can significantly impact the losses at the diode current level.

Nevertheless, not all devices were measured during the temperature-dependent measurement. The lowest dark current at room temperature 300 K, produced by the samples' 200 μm radii device of was chosen to be measured at elevated temperature. Every data is fitted with the general Shockley diode equation described in Equation 4.1 in order to determine the saturation current density and ideality factor.

$$J = J_0 \left[exp\left(\frac{qV}{nk_BT}\right) - 1 \right] - J_L \tag{4.1}$$

Where J is the total current density, q is the charge on an electron, and V is the applied voltage bias. k_B is the Boltzmann constant. T is the temperature of the diode during measurement. J_L is the additional drift current density caused by illumination. J_0 is the saturation current density of the diode, and n is the ideality factor. The ideality factor balances the contribution of total current from diffusion and recombination current. If the n is equal to 1, it is dominant by the diffusion mechanism, and n is equal to 2 when recombination mechanism dominates. The -1 and $-J_L$ terms from Equation 4.1 have been excluded during the fitting process. This means that the approximation does not hold the dark current data at low bias. Furthermore, since the experiment is conducted in a completely dark room, the contribution from photocurrent is insignificant.

The fitting quality shown in Figure 4.1 suggests that the dark current behavior agrees well with the ideal Shockey's diode equation. At high bias, the current behavior deviated from the fitting line, usually depicted as parasitic series resistance. A curving line obtained at high forward bias theoretically illustrates this series resistance characteristic. This condition could also be limited by the source-measurement unit (SMU), which indicates a straight-line section at high forward bias [9]. However, incorporating the series resistance effect into the approximation cannot fit the dark current data at high bias in this situation. A similar result has been exhibited in other literature on

GaAsBi p-i-n diodes [10,18]. This chapter's analysis emphasizes the region where the diode's current can be well-fitted using the Shockley diode equation.

In every fitting, the ideality factor ranges from 1.5 to 1.9. This finding recommends that current recombination mechanisms dominate the current behavior in these devices. To explicate this further, the J_0 values of the devices are estimated using the current recombination model by expanding Equation 4.1. The theoretical derivation of the J_0 term follows the S.M. Sze textbook in page 98 [19].

From Equation 4.1, expand the term J_0 becomes;

$$J = J_0\left[exp\left(\frac{qV}{nk_BT}\right) - 1\right] - J_L \tag{4.1}$$

$$J = q\sqrt{\frac{D}{\tau}}\frac{{n_i}^2}{N}\ exp\left[\frac{qV}{k_BT}\right] + \frac{qW_Dn_i}{2\tau}exp\left[\frac{qV}{2k_BT}\right] - J_L \approx J_0\left[exp\left(\frac{qV}{nk_BT}\right) - 1\right] - J_L \tag{4.2}$$

Where, D and τ are the diffusion coefficient and the recombination lifetime of the minority carriers in the junction, n_i is the intrinsic carrier density, N is the minority carrier impurity concentration, W_D is the depletion width,

The intrinsic carrier density is approximately given by:

$$n_i = 4.9 \times 10^{15}\left(\frac{m_{de}m_{dh}}{m_0^2}\right)^{3/4} M_C^{1/2} T^{3/2} exp\left(\frac{-E_g}{2k_BT}\right) \tag{4.3}$$

Where m_{de} (m_{dh}) is the density of states effective mass for electrons (holes), m_0 is the electron rest mass, h is Planck's constant, M_C is the number of equivalent minima in the conduction band. Grouping all non- or weakly-temperature dependent terms into simple coefficients (A', B' and C'), the temperature dependence of J can be approximated by:

$$J \approx \underbrace{A'\left[T^3 exp\left(\frac{qV-E_g}{k_BT}\right)\right]}_{Diffusion\ current} + \underbrace{B'\left[T^{1.5} exp\left(\frac{qV-E_g}{2k_BT}\right)\right]}_{Recombination\ current} \approx C'\left[exp\left(\frac{qV-E_g}{nk_BT}\right)\right] \tag{4.4}$$

Equation 4.4 indicates that the saturation dark current density results from a combination of diffusion and recombination current mechanisms. Theoretically, one of these current components dominates the saturation dark current term, J_0. The J_0 values of the devices extracted from Figure 4.1 were evaluated using only the recombination current approximation described in Equation 4.4. During this estimation process, the ideality factor is held constant at two, and the band gap values for each device described in Table 3.1 are applied. In this approximation, the band gap parameter described in Table 3.1 is considered fixed and does not change during the temperature-dependent measurement. The estimation of recombination current in Equation 4.4 is reliable for temperature-dependent analysis because most of the terms in the equation are constant and can be approximated using numerical methods, except for the temperature term which varies accordingly in the experiment. Figure 4.2 shows the results of the saturation dark current density as a function of temperature.

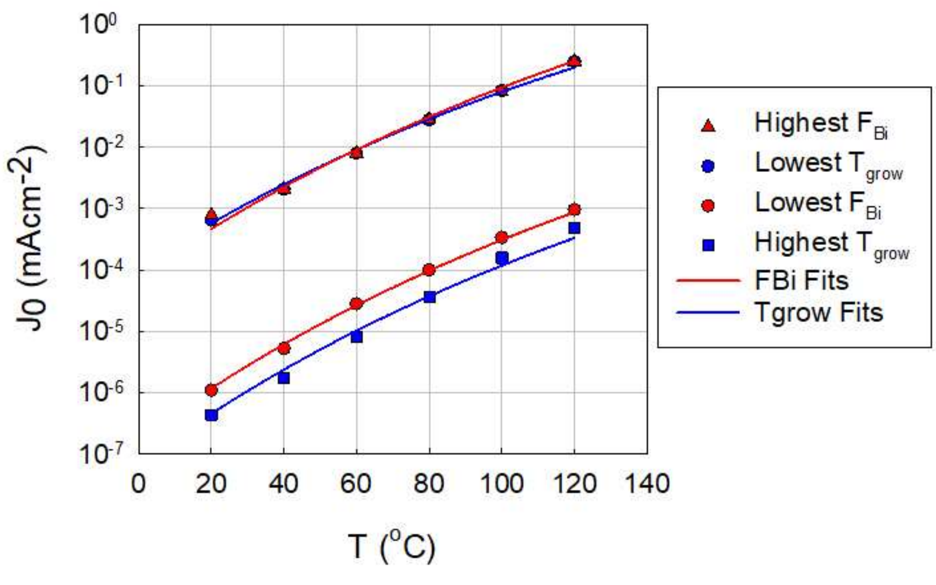

Figure 4.2: The J_0 varies with temperature for selected diodes. The fitting lines assume only recombination current (i.e. n = 2). [23]

In Figure 4.2, the saturation dark current density, J_0, is revealed to be dominated by the recombination current mechanism. The graph plots J_0 in (mAcm^{-2}) on the y-axis against temperature ranging from 20°C to 120°C on the x-axis. The markers on the graph correspond to the saturation dark density extracted from Figure 4.1 using Equation 4.1.

Meanwhile, the solid line indicates the estimated recombination current density calculated using Equation 4.4. From the results, it is evident that all saturation dark current density increases exponentially with the temperature-dependent measurement.

Additionally, all the recombination current density estimation lines agree well with the J_0 from the experimental data. The highest FBi saturation dark current density aligns with the lowest Tgrw current density, while the two low Bismide compositions series (lowest F_{BI} and highest T_{grw}) are slightly in a similar range. As the temperature rises from 20°C to 120°C, the saturation dark current density increases by about three orders of magnitude. Thus, these findings confirm that the recombination current mechanism dominates the saturation dark currents.

In Figure 4.2, the saturation dark current was previously estimated by fully considering the dominant recombination current. However, as the forward bias voltage increases, the current behavior may not be entirely dominated by recombination current, and the diffusion current component may contribute to the overall dark current at forward bias.

Therefore, in the next investigation, a complete temperature-dependent dark current behavior can be reevaluated using the overall term in Equation 4.4 by estimating the C' coefficient value and ideality factor through a numerical approach. For this estimation, the ideality factor is not fixed at two because to observe that the recombination mechanism may not entirely dominate the dark current. The band gap for these GaAsBi p-i-n diodes is similar to the band gaps in the previous description in Figure 4.2. All dark current data points from the forward bias measurement are grouped by particular biases corresponding to temperature. The results are represented in the Arrhenius plot, as illustrated in Figure 4.3. The dark currents data and their fitting line for each bias are plotted for 1000/T.

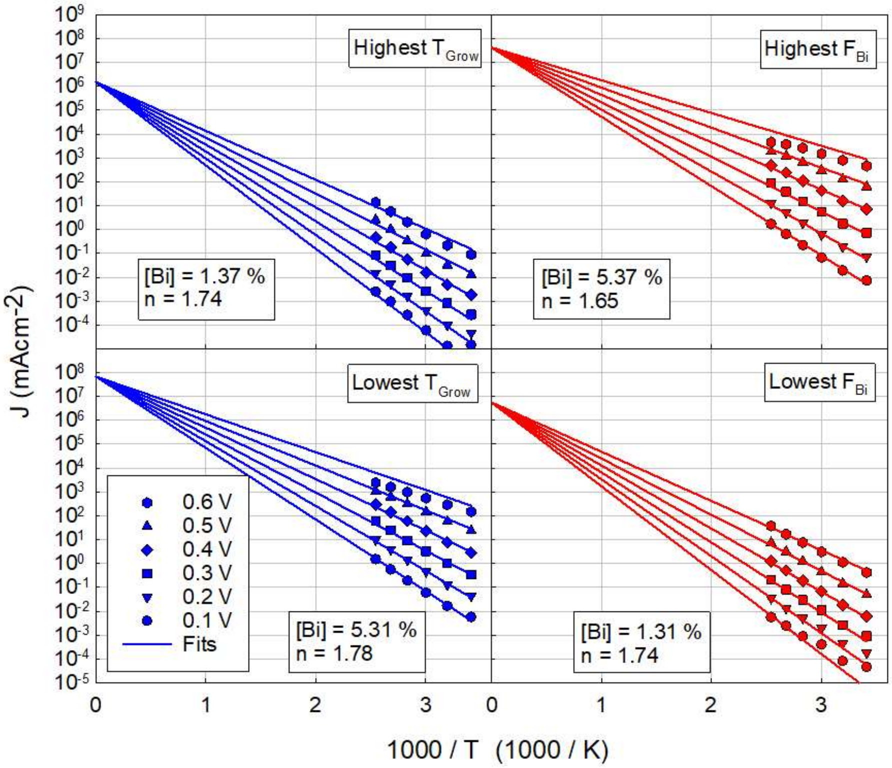

Figure 4.3: Arrhenius plots of the J-V data for selected diodes. For each device, the fitting lines were all produced using the band gap determined from the XRD results in [17] and a fixed ideality factor, as displayed in the figure. [23]

From the Arrhenius representation in Figure 4.3, the graph illustrates the dark current points in $mAcm^{-2}$ for each forward bias voltage against 1000/T. Every marker indicates the specific forward bias voltage range from 0.1 to 0.6 V. Each diode demonstrates a self-consistent dark current. Most intermediate voltages, ranging from 0.2V to 0.5V, achieve accurate fitting. At low voltage, the estimation may be affected by parasitic shunt resistance and the presence of a small light-bias photocurrent. When observed at high voltage, the diode's current behavior deviates from the Shockley diode equation, which aligns with the previous observation in Figure 4.1.

Moreover, in this approach, each diode is fitted using a fixed ideality factor between 1.65, 1.74 and 1.78, which correspond to the device estimation. As a result, the current recombination approximation remains a significant factor in the device's performance at high bias voltage. However, the recombination mechanism in the overall dark current does not strongly dominate compared to the saturation dark current density, which confirms that the ideality factor is noticeable at 2. It is justified that, even as temperature increases, the forward dark current is significantly limited by a recombination mechanism and can be well-fitted using a single ideality factor above 1.65.

In the previous discussion, the findings established that the recombination mechanism at temperature-dependent dominates the dark current behavior for the Bismide devices grown in different variation conditions. Next, is to examine how the Bismide concentration affects the dark current performance. The saturation current density of all GaAsBi p-i-n diode devices at room temperature is plotted based on their band gaps.

According to reference [9], the T_{grw} series consists of five devices grown at a constant Bismide flux of 10.6×10^{-8} mBar. However, the Bismide composition varies with different growth temperatures. On the other hand, the FBi series also includes five devices grown at a fixed Bismide growth temperature of 377 °C but with different Bismide fluxes. The information growth of these two series Bismide is adapted from [9] and presented in Table 4.2.

All of these p-i-n diodes underwent dark current-voltage measurements at room temperature. The saturation dark current for each device was determined using the standard Shockey diode equation described in Equation 4.1. Figure 4.4 portrays the saturation dark current density for each device according to the band gap of the device. All the data are fitted using the total forward current in Equation 4.4.

Table 4.2: Important growth parameters for two series of GaAsBi p-i-n diodes that are T_{grw} F_{Bi} series, adapted from [9]. The saturation current density is determined using Shockey diode equation.

Device	Growth Temperature (°C)	FBi BEP ($\times10^{-8}$ mBar)	Bi content from XRD measurement %	Band gap, Eg (eV)	Saturation dark current density, J_0 ($mAcm^{-2}$)
T_{grw} series	355	10.6	3.51	1.17	6.48E-04
	375	10.6	3.25	1.19	5.12E-05
	385	10.6	2.82	1.23	3.68E-05
	395	10.6	2.19	1.26	5.67E-06
	405	10.6	1.37	1.32	4.36E-07
F_{Bi} series	375	5.0	1.31	1.32	1.10E-06
	375	7.6	2.25	1.26	1.67E-05
	375	10.6	3.25	1.19	5.12E-05
	375	15.0	4.12	1.14	1.32E-04
	375	21.2	5.37	1.07	7.91E-04

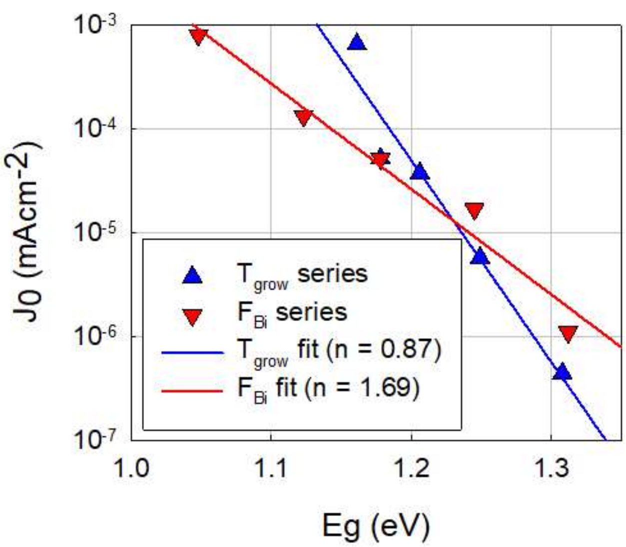

Figure 4.4: Room temperature saturation dark current (J_0) data of the devices. The red line indicates the expected behavior for recombination-dominated current and has been fitted to the F_{Bi} series data (red). The blue line is a simple exponential function fitted to the T_{grow} series data (blue); the Shockley diode equation could approximate this line with an ideality factor of 0.87. [23]

The result from Figure 4.4, depicts that all Bi flux series have about the same growth temperature (~ 375 °C), which merely agrees with the theoretical recombination current characteristic. Although the band gap varies, the data can still be fitted with a single ideality factor of around 1.69, which is relatively close to the result in the Arrhenius representation. This approximation is consistent with the temperature-dependent J-V discussion where the recombination mechanism dominates all dark current devices. However, the Tgrow series portrays a more dramatic increase of saturation dark current when the Bismide percentage increases, resulting in decreasing band gaps. A point of view from T. Rockett's interpretation of these results suggests that the device from the growth temperature series has been more significantly affected by related defects than the Bismide series devices [9].

Besides, it can be seen from the fitting line where the ideality factor is about 0.87, which is not physically reasonable and quite large discrepancy from which is different from the Tgrw series discussed in Figure 4.2 and Figure 4.3. The ideality factor in previous both figures agree well that the saturation dark current density in the Tgrw series dominated by the recombination current.

One of the possible reasons to explain this difference can be related to the recombination lifetime of the minority carriers, denoted by the (τ) term in Equation 4.2. In the Tgrow series, reducing the growth temperature produces higher Bismide incorporation, which can decrease band gaps to the targeted value. The decrement of minority carrier lifetime in devices from lower growth temperatures perhaps causes an enhanced dark current for this series. In order to understand the different behaviors of the two series, τ is estimated to be reduced by a factor of 40 between the highest and lowest growth temperature (405 °C and 355 °C), respectively. The calculation to demonstrate the reduction factor 40 is determined by considering the difference between the recombination current, J_{re}, and the fitted saturation current, $J_{0fit,}$ of the highest and lowest T_{grw} devices. The two devices have a band gaps of 1.31 and 1.16 eV respectively.

For the band gap at 1.32eV (the highest Tgrw device) the J_0 fitting line values are:
$J_{re} = 3.09\times10^{-6}$ mAcm^{-2} (F_{Bi} data point located on the red line at Eg equal to 1.32 eV)
Tgrw fit = 3.61×10^{-7} mAcm^{-2} (T_{grw} data point read on the blue line at Eg equal to 1.32 eV)
Therefore, to determine the J_{re} for the Tgrw fit similarly with the J_{re} on the red line, it can be corrected approximately = 10 × Tgrw fit.

For the band gap at 1.16 (the lowest Tgrw device) the J_0 fitting line values are:
$J_{re} = 6.03\times10^{-5}$ mAcm^{-2} (data point located on the red line at Eg equal to 1.16 eV)
Tgrow fit = 2.94×10^{-4} mAcm^{-2} (data point read on the blue line at Eg equal to 1.16 eV)
Thus, to determine the J_{re} for the Tgrw fit similarly with the J_{re} on the red line, it can be corrected approximately $J_{re} = 0.2 \times$ Tgrw fit.

To calculate the change in τ (assuming that's the reason for the increase in J_0), lets calculate the two factor differences:

At 1.31eV:
J_{re}/Tgrow fit = 3.09 mAcm^{-2} / 0.361 mAcm^{-2}
= 8.6

At 1.16eV:
Tgrow fit / J_{re} = 29.4 mAcm^{-2} / 6.03 mAcm^{-2}
= 4.9

As a result, the total factor difference = 8.6×4.9 ~ 40

A previous study has shown a GaBiAs with 8.4% bismide concentration were grown using an MBE machine at two different low temperature. One of the devices was grown at 280 °C and the other was at 330 °C. For a comparable growth temperature reduction (approximately 50 °C differences), an electron carrier lifetime decrement of two orders of magnitude was observed, although the researcher devices are grown at lower absolute growth temperatures [20].

In Appendix B, Figures 4.6 to 4.9 depict several droplet-like defects on the device surface. Notably, the device with a higher bismide concentration exhibited more defects than those with a lower concentration. The author also segmented the image and counted the number of droplet-like defects. The findings suggest that no significant correlation exists between the droplet density and bismide content for devices with less than 4% bismide incorporation. The defects are likely gallium droplets, possibly from the growth process, such as cell spitting or background impurities from the growth chamber.

4.4 Summary on the temperature-dependent dark current for GaAsBi p-i-n diodes

Temperature-dependent dark current densities of two sets of GaAsBi p-i-n diodes grown at different conditions were investigated. The diodes in the T_{grw} series were grown at 405°C and 355°C with a constant Bismide flux, while the diodes in the F_{Bi} series were grown at a fixed temperature of 375°C with various Bismide flux configurations.

The results indicate that dark current densities increased as the Bismide composition increased. As the temperature increased from 300 K to 393 K, the dark currents increased by over two orders of magnitude. The ideality factor ranges from 1.5 to 1.9, signifying that recombination current mechanisms dominate the devices' current behavior.

The devices' saturation current densities, J_0, were assessed using the recombination current model. The ideality factor was held constant at two fixed band gap values were applied. A graph was created to display J_0 against temperatures ranging from 20°C to 120°C, demonstrating an exponential increase in all saturation dark current densities. The study shows that the saturation dark current density aligns closely with the fitted estimation data when the ideality factor is equal

2. However, the current behavior is not entirely governed by the recombination current at high forward bias. During the approximation of high forward bias voltage, each diode is fitted using a fixed ideality factor between 1.65 and 1.78.

The study examines how the concentration of Bismide affects dark current behavior under different growth conditions. The results show that recombination current is the main factor influencing devices developed at a standard temperature. Devices grown at lower temperatures demonstrate higher dark current densities, likely due to a decrease in minority carrier lifespan caused by the lower temperature. The Bismide content of the devices has little impact on their characteristics apart from reducing the band gap, which leads to an increase in dark currents.

4.5 The structure of GaAsBi MWQ p-i-n diodes

The strategic use of Multiple Quantum Well (MQW) structures continues to revolutionize optoelectronic devices, enabling significant advancements in solar cells, lasers, and detectors. This development is due to the MQW's ability to confine carriers and tailor optical absorption. The critical aspect of designing MQW devices is precisely controlling barrier thickness and the number of QWs as they influence strain balance, carrier transport, and overall quantum well quality. It is crucial when working with lattice-mismatched materials like GaAs/InGaAs and GaAsBi/GaAs. Proper strain management is essential, as quantum wells can experience strain resulting from the lattice mismatch between the well and barrier materials, leading to defects and dislocations. Integrating thicker barriers makes it possible to alleviate strain, provide enhanced structural support, and reduce the interaction between adjacent QWs. These measures collectively contribute to superior strain balance and an overall enhancement in the quality of quantum wells. Figure 4.5 demonstrates the energy band structure for the GaAsBi MQW.

Figure 4.5 illustrates the energy band structure and carrier dynamics in a GaAsBi/GaAs multiple quantum well (MQW) p-i-n diode under the influence of incident sunlight. This structure is designed to enhance the absorption of sunlight and improve carrier dynamics within the device.

Sunlight enters the device, providing the energy needed to excite electrons from the valence band to the conduction band, primarily within the GaAsBi quantum wells due to their narrower band gap compared to the surrounding GaAs. The intrinsic region of the pin diode, containing the MQW structure. It's crucial for the operation of the device as it's where the electron-hole pairs are generated and separated.

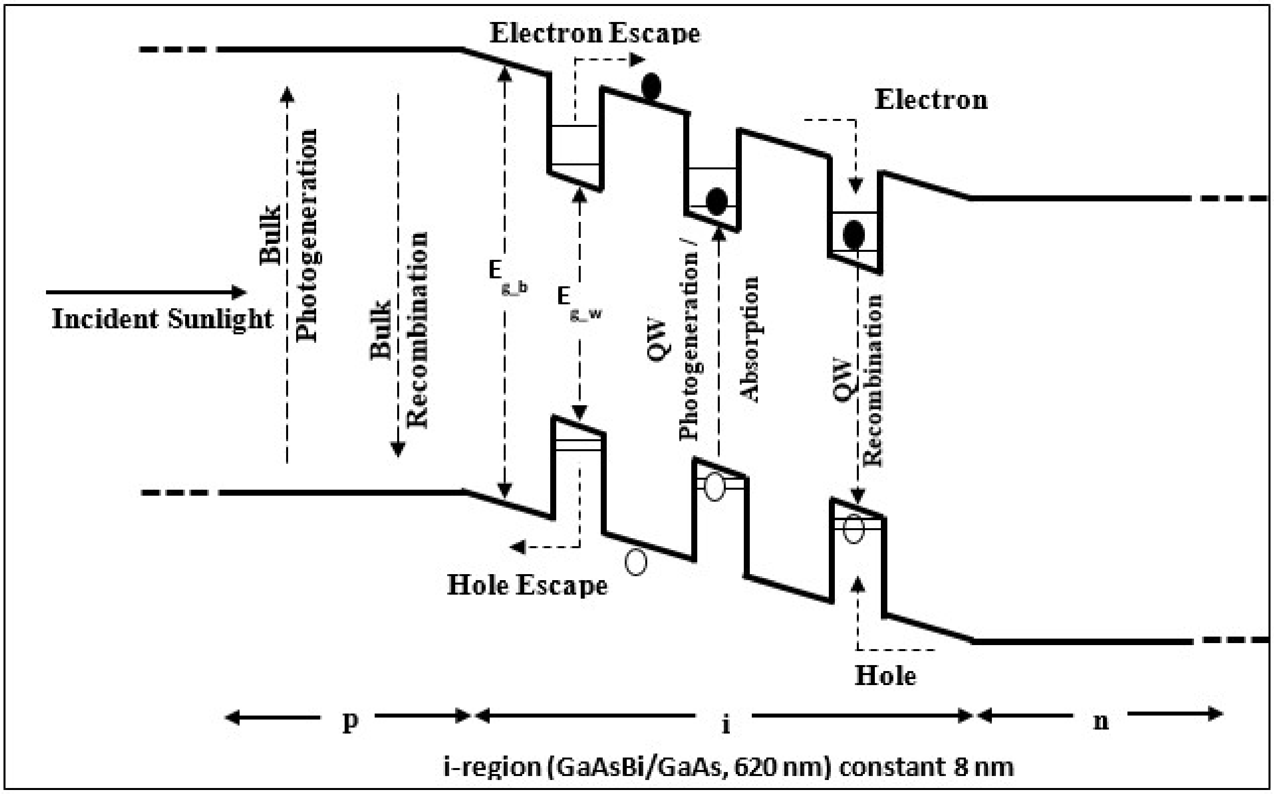

Figure 4.5: The energy band diagrams structure for the GaAsBi MQW pin diodes

This quantum well structure comprise of energy band gap of the well (GaAsBi) and band gap of the barrier (GaAs) which denoted by E_{g_w} and E_{g_b}. The quantum well has a narrower band gap compared to the barrier which is typical in MQW structures to enhance absorption and carrier confinement allowing for more efficient utilization of the solar spectrum. Nevertherless, recombination within the quantum wells, potentially due to defects or interface quality. Ideally, the recombination in well is minimized through design optimizations to ensure that most carriers contribute to the photocurrent. The electron and hole generated in the quantum wells may have enough energy to escape to the barrier layers (GaAs) and then contribute to the photocurrent. This is facilitated by the thermal energy, depending on the barriers thickness modulation or having favorable band alignments and also the energy of the carriers. Conversely, carriers from the barriers can be captured into the wells. This dynamic equilibrium affects the carrier density and recombination rates within the wells.

Besides, during the incident sunlight is absorbed in bulk region electrons and holes are generated in the bulk AlGaAs regions outside the quantum wells. Some of the carriers recombine in the bulk material before they can contribute to photocurrent. This bulk recombination represents recombination losses in the bulk material outside of the quantum wells. It is an undesirable process where electron-hole pairs recombine without contributing to current generation.

The MQW structure is designed to enhance the absorption of light, thereby increasing the generation of photocarriers (electrons and holes). By carefully designing the band gap of the wells and barriers, the device can optimize the separation and collection of carriers, which is crucial for achieving high efficiency in solar cells. The intrinsic region (i-region) plays a pivotal role by serving as the active layer where most of the photoconversion processes occur.

This GaAsBi MQW p-i-n diode structure represents a sophisticated approach to enhance the photovoltaic properties of solar cells by integrating materials with different band gaps to optimize light absorption and carrier management. The use of GaAsBi in quantum wells is particularly significant due to its ability to absorb lower energy photons, thus broadening the spectral response of the solar cell, which increases the range of photons that can be converted to electrical energy.

In this experiment, the GaAsBi MQW pin diodes are grown at 380 °C and applied similar bismide flux at 2.4 × 10-7 mBar. The i-region thickness for each quantum well device is maintained at 620 nm, and the well layer thickness remains constant at 8 nm while the barrier thickness varies accordingly. Table 4.3 provides information on barrier thickness and the estimation of bismide content. The schematic structure of the GaAsBi MQW pin diode is shown in Figure 4.6. The growth process is described in Chapter 3, under subheading 3.2.2, and these devices are grown by Dr. R.D. Richards in the MBE Laboratory at the University of Sheffield.

Table 4.3: The MQW device Bi contents were estimated from transmission electron microscopy and photoluminescence measurements [21].

Series	Tgrow (°C)	FBi (× 10-7 mBar)	Number of QWs	Barrier thickness (nm)	[Bi] (%)
MQWs	380	2.4	5	97	5.0
	380	2.4	20	22	5.0
	380	2.4	40	7.3	5.0
	380	2.4	54	3.4	5.0
	380	2.4	63	1.8	5.0

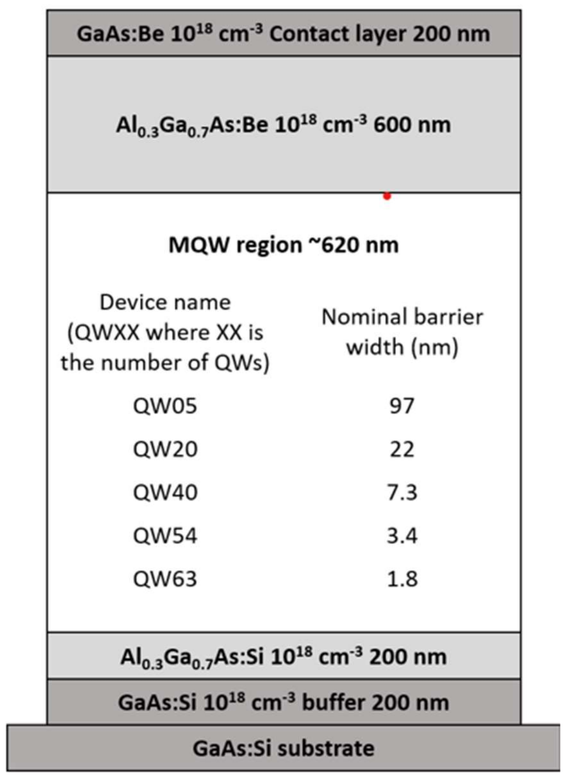

Figure 4.6. Schematic diagrams of the GaAsBi MQW device structures in this experimental work.

The thickness of the individual quantum well and barrier should be reduced when increasing the number of quantum wells while keeping the total active region thickness constant. Thus, adding more quantum wells while maintaining the same active region thickness results in thinner individual layers. However, the structure for this GaAsBi MQW pin diode shown in Figure 4.6 depicts that the well has an acceptable significant thickness at 8 nm, and this thin layer is kept constant while increasing the number of wells. The barrier thickness is reduced from 97 nm to as low as 1.8 nm when the number of wells increases. Thinner wells can tolerate strain better for successful strain balancing, but thin barriers can worsen strain buildup, leading to strain relaxation at defect sites.

More wells with thinner barriers can increase strain within the structure as strain accumulates from each quantum well. When the barrier is too thin, significantly below 1 nm, the strain cannot fully relax, which leads to the generation of dislocations that reduce the quality of the quantum wells. In contrast, keeping the barrier thickness above 10 nm can help accommodate the strain, even when the number of wells increases.

The thickness of the barriers directly impacts the quality of quantum wells. Thicker barriers effectively isolate quantum wells, thereby minimizing well-to-well interaction and ensuring the QWs are free from strain-related dislocations. Moreover, thicker barriers significantly enhance carrier confinement, leading to a potential improvement in device performance. In this experiment, QW 05, QW20, and QW40 are relatively considered in the range of strain-balancing devices because their barrier thickness is moderately thicker than QW54 and QW63. Yet, the QW54 and QW 63 are having strain-relaxation effects. However, both devices' barriers still have thicknesses above 1 nm.

If the barriers are too thin, strain relaxation can become incomplete, leading to increased recombination at defects and reduced performance. In addition, the barrier thickness significantly influences the phenomena of carrier tunneling between adjacent QWs. Thinner barriers (below 1 nm) can result in quantum mechanical tunneling between wells, leading to leakage current and increased recombination, which degrades device performance. Very thin barriers reduce confinement and enhance tunneling effects.

From previous literature, this GaAsBi MQW series was distinguished into two categories. There are strain-balancing and strain-relaxation devices. Strained devices comprise of QW03, QW05, QW20 and QW40, whereas QW54 and QW63 are relaxed devices [21].

The classification can be identified from the growth structure defect observed using Normaski measurement. The Normaski image for GaAsBi MQW p-i-n devices is shown in Appendix C. Dr. R.D. Richards from the University of Sheffield conducted the measurement, and the results were documented in his manuscript [21]. The image in Appendix C shows varying sub-surface damage lines in all MQW samples. The sub-surface damage lines for devices from the lower quantum wells (QW05 up to higher QW40) were found to have very few orthogonal and straight lines. This condition does not exhibit a strain relaxation effect on the sample. In contrast, plentiful damage lines are observed in QW54 and QW63, with more straight and orthogonal lines found under the Nomarski microscopy [21]. These findings indicate strain relaxation existed in these higher quantam well samples. As a result, the dark current for relaxed devices is higher than for strain-balancing MQW devices.

4.6 Temperature-dependent dark current of MQW GaAsBi devices

In previous dark current discussion for bulk pin diodes, the dark current behavior is not affected much from the Bismide flux growth-based condition. However, lowering the growth temperature regime for getting higher bismide content, appears reducing the carrier-life time thus increasing dark current. In this section, the dark current behavior of a series of multiple-quantum wells (MQW) GaAsBi/GaAs p-i-n diodes are investigated at various temperature from 25° C until 120° C. The temperature-dependent measurement is conducted by having a similar approach as described before. The purpose of this measurement is to investigate how the current mechanism dominated in the GaAsBi MQW devices. Furthermore, it is to observe the dark current performance in the MQW as compared with bulk devices.

Table 4.3 shows the saturation dark current density, J_0 for All MQW series at room temperature. This J_0 data was extracted from the dark current performance shown in the previous record [22]. It can be seen that the dark current for the relaxed device increases by two orders of magnitude. Thus, the high dark current in QW 54 and QW63 indicated that these devices undergo dislocation generation during the relaxation. The same work demonstrates that QW 20 and QW 40 have enough strain balancing to undergo dislocation propagation and no forming of dislocation generation was found in QW05 [22]. The dark current for MQW series at room temperature are shown in Appendix D.

Table 4.4: Saturation current density, J_0 with respect to quantum well series at room temperature

MQW series	Barrier thickness (nm)	Saturation current density, J_O (mA/cm^2)
QW05	97	1.60×10^{-6}
QW20	22	2.40×10^{-5}
QW40	7.3	3.87×10^{-5}
QW54	3.4	1.30×10^{-4}
QW63	1.8	5.21×10^{-4}

Next, the MQW series undergo dark current measurement at high temperature elevated from 20 °C to 1.86 at 120 °C. The experimental work procedures are similar during conducting high-temperature measurement for GaAsBi bulk pin series as discussed earlier. Only QW 54 is not involved in this measurement. It is because the QW54 suffering with a large series resistance start from forward bias 0.4 V. It seems that the device not just affected by dislocation generation in relaxation after growth but also the quality defect during device fabrication. Similar results were obtained for the MQW devices, as illustrated in Figure **Error! Reference source not found.**4.7. All devices are showing rectifying diode behavior at temperature from 20 °C to 120 °C. Forward dark current in each device shown increment relationship when temperatures rise. In addition, it also increases significantly as the number of quantum well become higher.

The fitting approach is conducted base on Equation 1 by applying a similar approach where the -1 and JL terms are negligible. Both GaAsBi MQW and bulk series adequately estimated with Shockey diode ratification as described in Equation 1. The ideality factor of all devices is within a range from 1.50 until 1.98. Several dark current data at low bias are not well agreed with the fitting line. It is probably due to the influence exhibit from shunt resistances effect.

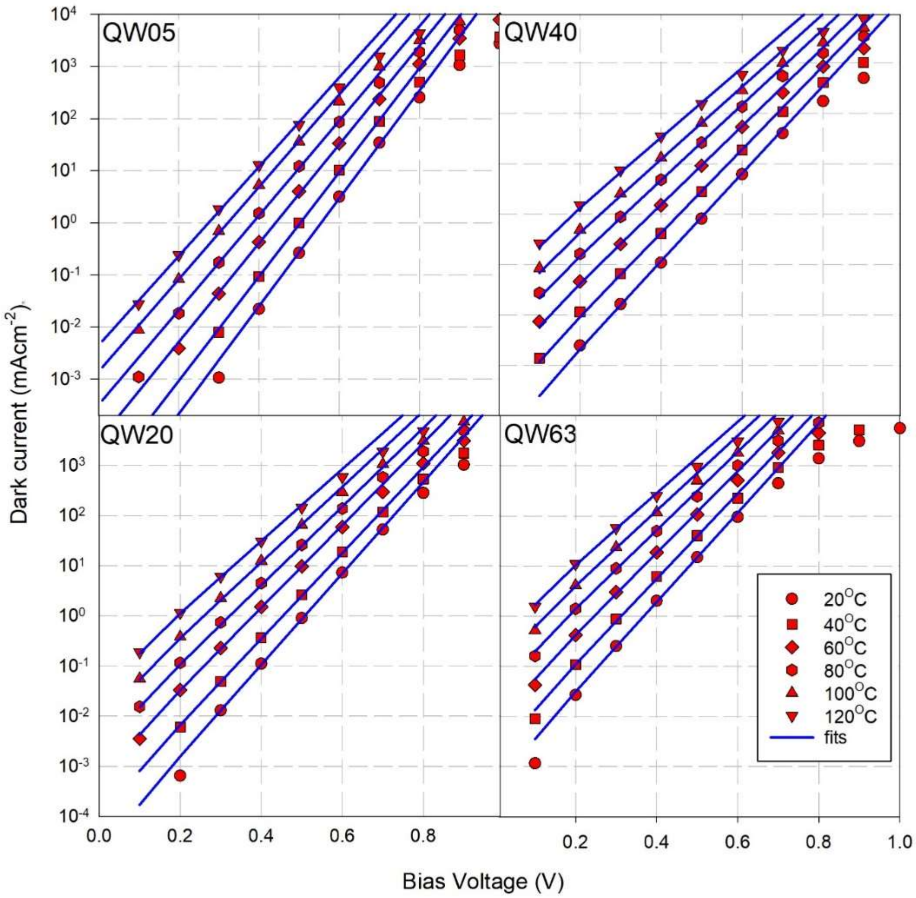

Figure 4.7:J-V data MQW series pin diode at temperatures between 20 °C and 120 °C (by increments of 20 °C).

Shunt resistance plays a significant role in controlling the magnitude of the dark current. In an ideal solar cell with infinite shunt resistance, no leakage current would flow through alternative paths, and the dark current would only be determined by the diode characteristics. However, when Rsh is low, parasitic currents increase the overall dark current, reducing the cell's performance, especially at elevated temperatures.

Shunt resistance tends to decrease with increasing temperature due to enhanced carrier mobility and the activation of more leakage paths. Imperfections in the device structure, such as strain defects and the dislocation of the bismide atom in the lattice-mismatched growth, become more conductive at higher temperatures, allowing more current to bypass the junction. As the shunt resistance decreases, the additional leakage current increases the total dark current, further degrading the solar cell's performance. Furthermore, at high bias significantly around 0.6 V and above, the dark current results are affected by the series resistance.

Figure 4.8 shows the J_0 temperature dependence for the MQW devices. In most cases, the temperature dependence data is well fitted by applying Equation 4. For this analysis, the energy band gap of the devices is fixed at room temperature. The value is obtained from previous literature [21]. However, the ideality is not fixed to two as has been applied during estimating the J_0 of bulk p-i-n diode series.

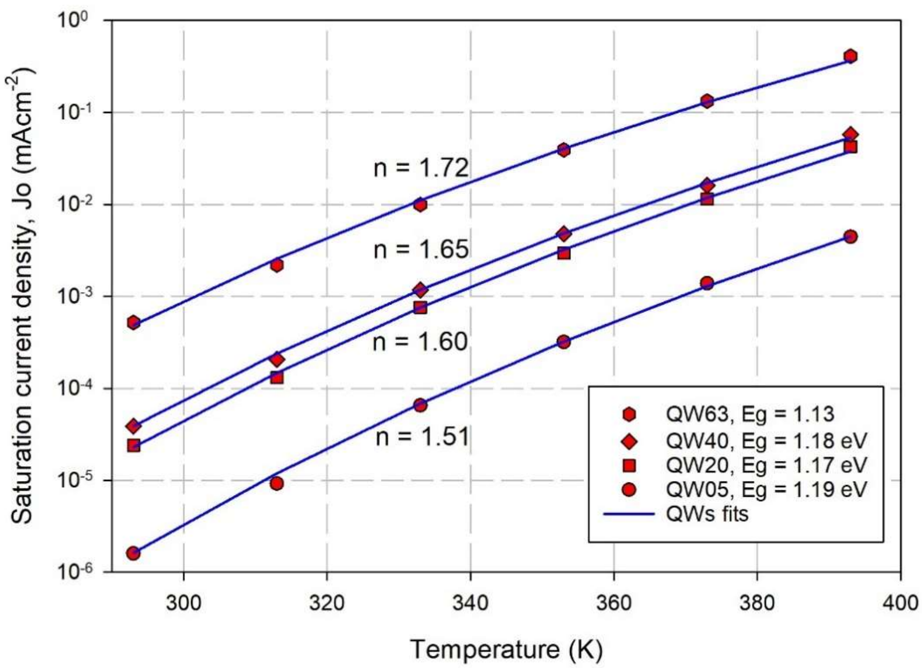

Figure 4.8: Temperature dependence of J_0 for each of the MQW devices. The fitting curves assume not purely dominating by recombination current.

It is found that, to fit J_0 temperature data for MQW devices, ideality factor must be allowed to be estimated. As demonstrated in Figure 4.8, the ideality factor varies between 1.51 to 1.72. This finding indicates that the J_0 for MQW is not purely assumed as recombination mechanism. The MQW saturation current density is less dominated by recombination current compare with the bulk p-i-n series. In the case of QW05, a slightly lower ideality factor suggests that strain devices having less defect and dislocation generation effect than strain-balancing and relaxed devices.

Moreover, it is also found that as the temperature rises from 25°C to 120°C, the saturation dark current density increases about three orders magnitude. The saturation dark currents of MQW devices are not exhibit very much dominated by recombination current mechanism. Hence, verifies the performance of MQW devices are significantly better than both bulk p-i-n series and have a good potential for solar cell analysis under light illumination.

A full temperature-dependent forward dark current for bias from 0.1 V to 0.6 V for MQW devices is represented in Arrhenius plot as shown in Figure 4.9. The ideality factor for each device is estimated and implemented to fit all dark current data. From the Arrhenius representation, it can be seen that each diode exhibits a good consistent dark current and well agreement with the Arrhenius fitting line. Similar with findings in bulk p-i-n series, most intermediate voltages range from 0.2 V until 0.5 V achieve satisfactory accurate approximation.

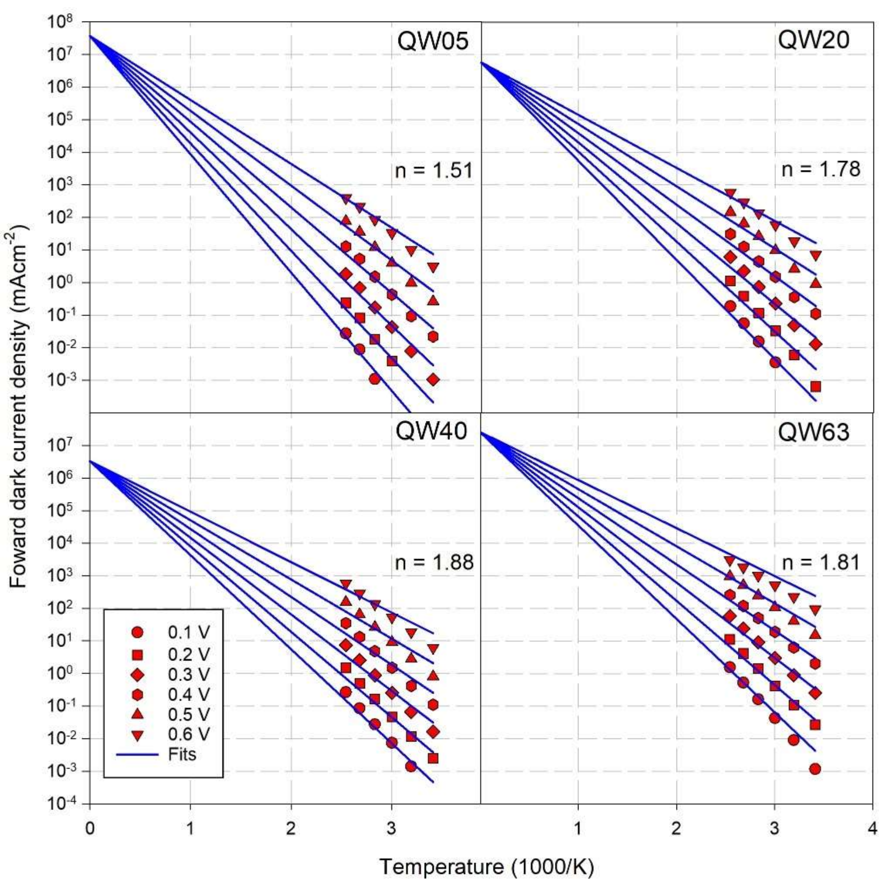

Figure 4.9: Arrhenius plot for MQW forward dark current. Equation 4 is applied to approximate the fitting line by using fix energy band gap and single value ideality factor.

The estimation for low bias voltage which below 0.3 V and high bias above 0.5V, may be affected by the influence of shunt resistance and series resistance respectively. Moreover, in this approach each diode is fitted using a fix ideality factor between 1.51 to 1.88. It is quite close with ideality factor estimated during J0 fitting. Thus, verify that the forward dark current data for MQW devices are completely not pure dominated by recombination current mechanism. As a results, it is clearly agreed that although the temperature increases, the MQW GaAsBi devices are not only limited by recombination mechanism but also can be fitted well using single ideality factor.

4.7 A brief summary for MQW GaAsBi devices' dark current

The key findings in the MQW devices' dark current indicate that the dark current increases by about three orders of magnitude as the temperature increases from room temperature to 120 °C**.** At high temperatures, electrons and holes can escape from the quantum well into the barrier layer, introducing additional paths for non-radiative recombination. This leads to a decrease in the device's dark current performance.

The analysis also reveals that the recombination dark current dominates the dark current for strain-relaxation devices (QW63) with an ideality factor of 1.72. On the other hand, strain-balancing devices like QW20 and QW40 exhibit a lower ideality factor, indicating less dominance by the recombination current mechanism.

An analysis of QW05 demonstrates an even lower ideality factor of 1.51, suggesting less influence from the recombination current mechanism. In addition, it is found that an increase in the number of quantum wells leads to thinner barrier thickness modulation, resulting in a higher dark current dominated by non-radiative recombination. The device QW05 with a thicker barrier shows reduced influence from the recombination current mechanism. The study also suggests that increasing the barrier thickness to around 10–20 nm helps reduce strain accumulation and improves carrier confinement by mitigating strain-related dislocations. This ultimately leads to fewer defects and improved device quality (Jang et al., 2017).

4.8 Summary

This chapter presents essential findings regarding the temperature-dependent dark current in bulk and MQW GaAsBi devices. The bulk p-i-n devices comprise two different series named Tgrw and FBi. At the same time, the MQW series is categorized based on the number of quantum well structures. The initial finding is that all devices demonstrate strong diode rectifying behavior during temperature-dependent measurements. The dark current for each device increases about three order magnitudes as the temperature increases from 20 °C to 120 °C (with 20 °C increment). These dark currents can be accurately modeled using the standard Shockey diode equation.

The second significant result shows that the recombination current mechanism dominates the saturation dark current in all bulk devices. All the J_0 for both bulk series agree excellently with approximating a fixed ideality factor set at two and a constant energy band gap during the temperature-dependent analysis. However, the MQW devices are only partially dominated by recombination current. While fitting the saturation current, the ideality factor for MQW devices is below two and even less than 1.7 for a strain device compared with the relaxed devices.

The dark current result in both structures indicates that the MQW pin diodes provide better carrier confinement due to the thicker barrier layer and are less dominant by the recombination current mechanism. However, a strain-relaxation device with a thinner barrier, nominally around 1.8 nm, has a higher dark current due to the strain defect in the quantum well structure. Proper strain management is essential, as quantum wells can experience strain resulting from the lattice mismatch between the well and barrier materials, leading to defects and dislocations.

The third finding is that dark currents dramatically increase when the growth temperature of bulk pin devices decreases to achieve a higher Bismide composition. Lower growth temperatures result in higher dark current densities, mainly because of a decrease in the lifespan of minority carriers. Therefore, it is essential to keep the growth temperature constant and adjust the Bismide flux to achieve a specific Bismide composition during growth conditions, as this significantly affects their dark current properties.

Moreover, the growth temperature for all MQW devices is maintained at 380 °C, which could be another reason that enables the development of GaAsBi with less dislocation defect during the growth process and prevents the MQW devices from the rapid increase of dark current at high temperatures. This indicates that growth temperature is a crucial factor for growing GaAsBi devices either for bulk or MQW structures. Utilizing optimized growth temperature produces the best state of career lifetimes and excellent dark current performance, making this research highly relevant and applicable to the field of semiconductor materials and device fabrication.

Reference

[1] T. Thomas, A. Mellor, N.P Hylton, et al., "*Requirements for a GaAsBi 1eV sub-cell in a GaAs-based multi-junction solar cell*", Semiconductor Science and Technology, vol. 30, no. 9, 2015, p. 094010.

[2] Sweeney, S.J. and S.R. Jin, "*Bismide-nitride alloys: Promising for efficient light emitting devices in the near- and mid-infrared*", Journal of Applied Physics, vol. 111(4), 2013, p. 043110.

[3] Lewis, R.B., M. Masnadi-Shirazi, and T. Tiedje, "*Growth of high Bi concentration $GaAs_{1-x}Bi_x$ by molecular beam epitaxy*", Applied Physics Letters, vol. 101(8), 2012. 101(8): p. 082112-082114.

[4] Dagnelund, D., et al., "*Identification of an isolated arsenic antisite defect in GaAsBi*", Applied Physics Letters, vol.104(5), p. -.

[5] Tait, C.R., L. Yan, and J.M. Millunchick, "*Spontaneous nanostructure formation in GaAsBi alloys*", Journal of Crystal Growth, vol. 493, 2018, p. 20-24.

[6] Puustinen, J., et al., "*Variation of lattice constant and cluster formation in GaAsBi*", Journal of Applied Physics, vol. 114(24), 2013, p. -.

[7] V. Bahrami-Yekta, T. Tiedje, and M. Masnadi-Shirazi, "*MBE growth optimization for $GaAs_{1-x}Bi_x$ and dependence of photoluminescence on growth temperature*", Semiconductor Science and Technology, vol. 30, no. 9, 2015, p. 094007.

[8] Hunter, C.J., et al., Absorption Characteristics of $GaAs_{1-x}$ Bi_x/ GaAs Diodes in the Near-Infrared. IEEE Photonics Technology Letters, 2012. 24(23): p. 2191-2194.

[9] Rockett, T.B.O., et al., Influence of growth conditions on the structural and opto-electronic quality of GaAsBi. Journal of Crystal Growth, 2017. 477: p. 139-143.

[10] Hasegawa, S., et al., PEDOT:PSS/$GaAs_{1-x}$ Bi_x organic–inorganic solar cells. Japanese Journal of Applied Physics, 2019. 58(6): p. 060907.

[11] K akuyama, K., et al., Impact of a small change in growth temperature on the tail states of GaAsBi. Journal of Applied Physics, 2019. 126(4): p. 045702.

[12] D. A. Beaton, R. B. Lewis, M. Masnadi-Shirazi, and T. Tiedje, "Temperature dependence of hole mobility in GaAs1-xBix alloys," (in English), Journal of Applied Physics, Article vol. 108, no. 8, p. 4, Oct 2010, Art no. 083708, doi: 10.1063/1.3493734.

[13] S. Adachi, "OPTICAL DISPERSION-RELATIONS FOR GAP, GAAS, GASB, INP, INAS, INSB, ALXGA1-XAS, AND IN1-XGAXASYP1-Y," (in English), Journal of Applied Physics, Article vol. 66, no. 12, pp. 6030-6040, Dec 1989, doi: 10.1063/1.343580.ded

[14] Sandall, I.C., et al., Demonstration of InAsBi photoresponse beyond 3.5 μm. Applied Physics Letters, 2014. 104(17): p. 171109.

[15] Cao, Z., et al., Influence of annealing on the electrical characteristic of GaSbBi Schottky diodes. Journal of Applied Physics, 2019. 126(5): p. 053103.

[16] Gu, Y., et al., Nearly lattice-matched short-wave infrared InGaAsBi detectors on InP. Applied Physics Letters, 2016. 108(3): p. 032102

[17] Richards, R.D., et al., Molecular beam epitaxy growth of GaAsBi using As2 and As4. Journal of Crystal Growth, 2014. 390(0): p. 120-124.

[18] Muhammetgulyyev, A., et al., Characterization of a GaAs/GaAsBi pin solar cell. Semiconductor Science and Technology, 2019. 34(8): p. 085001.

[19] Sze, S.M., Physics of Semiconductor Devices. 2 ed. 1981: John Wiley & Sons, Inc.

[20] Pačebutas, V., et al., Characterization of low-temperature molecular-beam-epitaxy grown GaBiAs layers. Semiconductor Science and Technology, 2007. 22(7): p. 819.

[21] Richards, R.D., et al., MBE grown GaAsBi/GaAs multiple quantum well structures: Structural and optical characterization. Journal of Crystal Growth, 2015. 425: p. 237-240.

[22] Richards, R.D., et al., Photovoltaic characterisation of GaAsBi/GaAs multiple quantum well devices. Solar Energy Materials and Solar Cells, 2017. 172: p. 238-243.

[23] R.D. Richards, F. Harun, M.R.M Nawawi, Liu Y., et al, “Temperature and bandgap dependence of GaAsBi p-i-n diode current-voltage behavior”, Journal of physics. D, Applied physics, Vol.54(19) (2021) p.195102, IOP Publishing, doi: 10.1088/1361-6463/abe4ff

Chapter 5

Temperature-Dependent of Light Current-Voltage Characteristic and solar cell parameters for MQW GaAsBi p-i-n Devices

5.1 Introduction

Light absorption quality is essential for the efficiency of solar cell devices, significantly impacting the photocurrent, open-circuit voltage (Voc), and overall interaction with the material's band gap. Gallium Arsenide Bismide (GaAsBi) is an emerging material in solar cell applications due to its tunable band gap and enhanced absorption properties in the infrared (IR) region. This makes it a promising candidate for improving solar cell performance by absorbing a broader range of the solar spectrum than traditional materials like GaAs.

The open-circuit voltage (Voc) in solar cells is primarily determined by the difference between the quasi-Fermi levels of electrons and holes under illumination and its characteristic proportionally with the material's band gap. For GaAsBi, while the reduction in band gap enables more significant absorption of low-energy photons, thus increasing light-generated current within the infrared region, it can also lead to a reduction in Voc. The reduced band gap can limit the maximum achievable Voc compared to higher band gap materials like GaAs. Furthermore, the temperature-dependent of the device also affects the open circuit voltage. Since the saturation dark current increases with temperature, it will limit the open-circuit voltage.

On the other hand, implementing multiple quantum well structures can increase solar cell efficiency. Selecting an appropriate formation of quantum well and barrier width enables the effective band gap absorption modification to improve the photo-excited carrier extraction process. Besides, the open circuit voltage is determined by the quantum well's barrier region. Thus, when the configuration of the quantum well parameters is enhanced, it can optimize the short circuit current and open circuit voltage performance separately [1].

To date, there has been no investigation on the photo-generated current mechanism based on the i-region of GaAsBi devices at high temperatures. The study of the device's current performance when the temperature increases is significant for the GaAsBi solar cell to observe the contribution of bismide incorporation in increasing photo-absorption band edge and carrier extraction that will increase the short-circuit current performance under concentrator application. Therefore, this chapter focuses on determining the photo-generated current under the illumination of monochromatic light and estimating the solar cell parameters' performance. Next, the light from the solar simulator will illuminate the devices to study the overall short-circuit and open-circuit voltage performance. The second part of this chapter will investigate the effect of carrier trapping in the MQW p-i-n diode by introducing light-bias measurement at low temperatures.

5.2 Experimental setup

The experimental setup follows the photocurrent measurement setup explained earlier in Chapter 3, section 3.4. The MQWs device is heated from 25◦C until 120◦C, and the device's temperature is monitored during the experiment. Then, the device is illuminated by the light source coupled with a monochromator. Photocurrent response spectra for slight forward bias voltage are recorded at different temperatures. The photo-generated current from the illumination will be calculated for each bias voltage and temperature. These results will allow us to determine the short-circuit current and estimate the open-circuit voltage for different devices for each bias voltage and temperature.

5.3 Analysis for Photo-generated Current Mechanism in GaAsBi MQWs p-i-n diodes

5.3.1 Photocurrent response in GaAsBi MQWs p-i-n diodes

In previous work, a novel approach was taken to measure the photocurrent and external quantum efficiency at room temperature. The measurement was conducted at zero bias voltage and slightly forward bias voltage. An un-doped GaAs wafer was then used in an innovative way to filter any light wavelength below 870nm, preventing carrier excitation from occurring in the AlGaAs cladding region and well’s barrier. This filter is particularly crucial as the band gap of GaAs is about 1.42 eV, corresponding to the wavelength of around 870 nm.

Furthermore, the GaAs filter's ability to remove any monochromatic light below 870 nm that carries photons above the energy band gap of GaAs is crucial. This procedure allows us to apply a specific light spectrum range, leading to significant photon absorption near the band edge of the GaAsBi. Importantly, it also enables only evaluating the carrier excitation process in the quantum wells region [2] as a critical aspect of this study. This section presents the measurement results from the QW 20 device to explain the process of determining the photo-generated current mechanism. The exact process and procedures are also applied to other MQW pin devices. Figure 5.1 illustrates the forward bias photocurrent response for QW 20 at different temperatures.

The photocurrent response for all different temperatures shows similar behavior from 0V bias and at small forward bias voltage. The photocurrent at zero bias appears to have the highest magnitude, then decreases as the forward bias increases. When a forward bias is applied, the total current behavior starts dominated by diffusion current, preventing photocurrent generation in the i-region. Based on Shockey's diode principle, it is likely that diffusion current will rise exponentially during forward bias, especially after leaving the built-in potential voltage. This majority diffusion current will dominate in the solar cell condition after the open-circuit voltage. The reduction of the photocurrent above 0V bias is expected due to the limitation of collecting photo-generated carriers as the forward bias increases.

Furthermore, higher temperatures also influence the performance of photocurrent. The graphs show that the photocurrent values for every temperature are pretty much the same except from 80°C until 120°C has a slightly lower photocurrent. For example, the photocurrent of 0.4V bias at 100°C and 120°C are two times lower than the photocurrent at room temperature. A similar trend is observed for the 0.2V bias. At around 910 nm, a shoulder peak can be seen at temperature 80°C and above. This is like the appearance of GaAs peak probably from the QW's well barrier as the spectrum shifts when temperature increases. However, the GaAs substrate that acts as the filter stays at room temperature during the device is heated. For further observation, the photocurrent from QW20 is compared with InGaAs/GaAs MQW p-i-n diode and the result is shown in Figure 5.2.

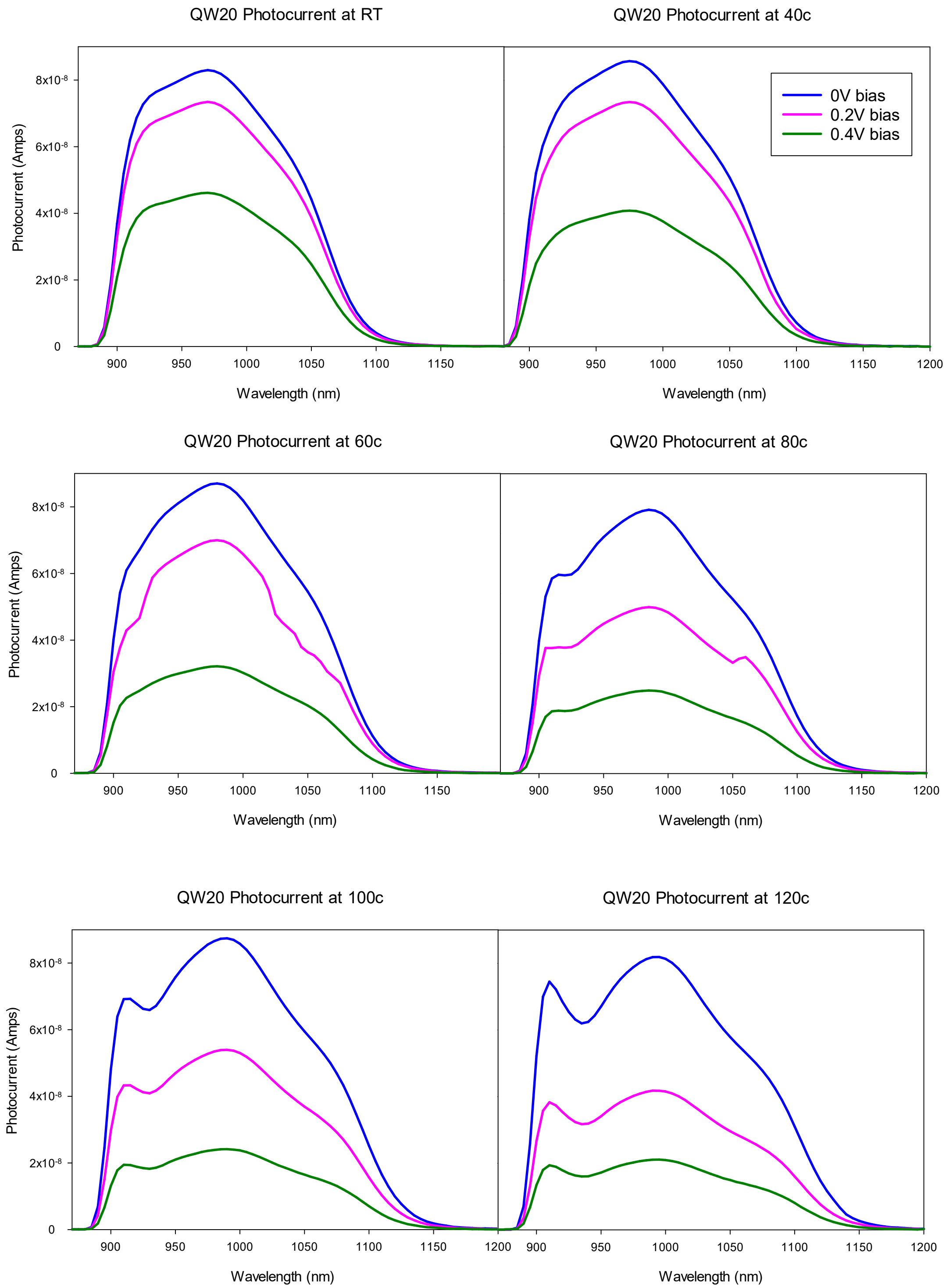

Figure 5.1: Photocurrent response of QW 20 measured for slight forward bias voltage at different temperatures.

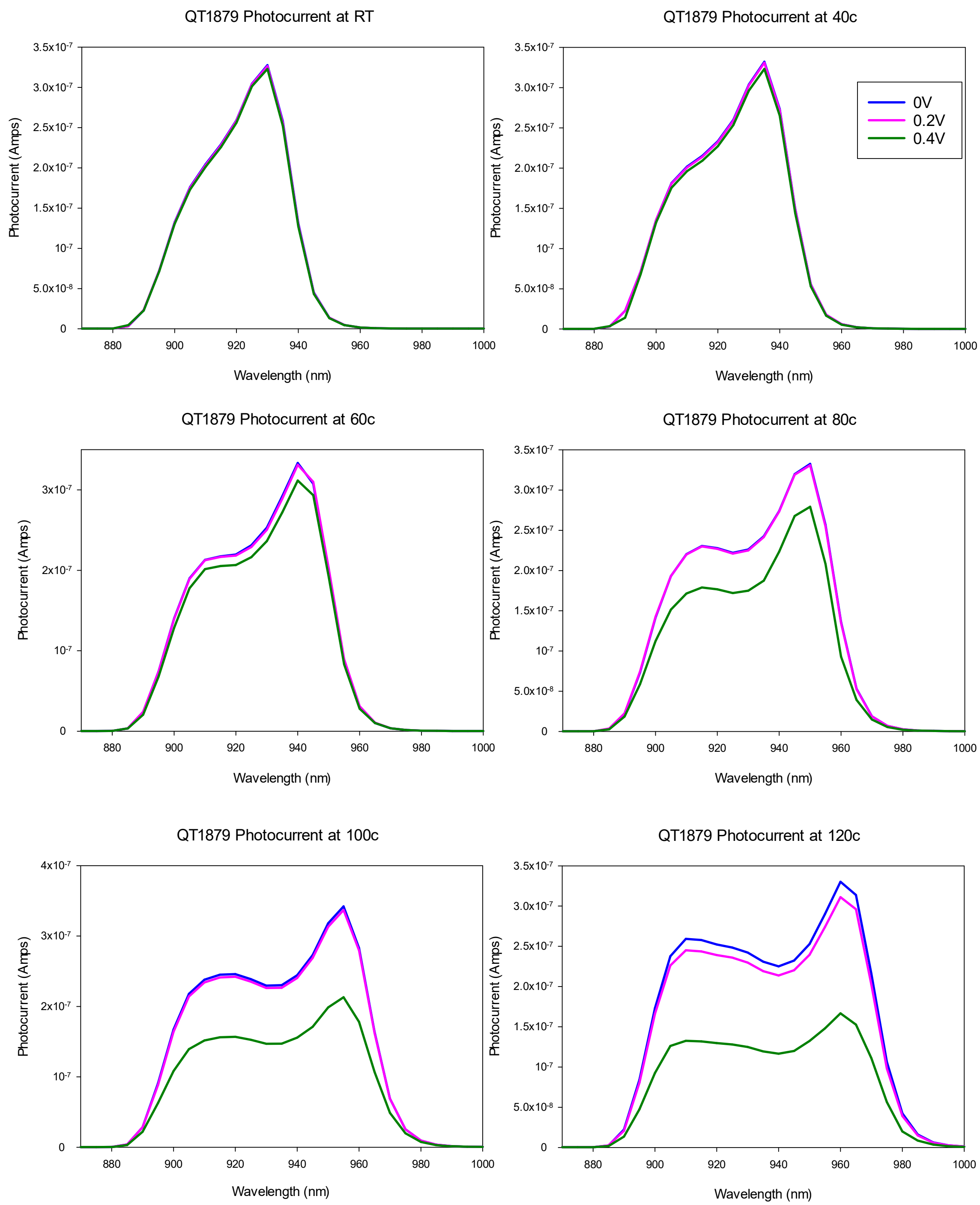

Figure 5.2: Photocurrent response of QT1879 measured for slight forward bias voltage at different temperatures.

The photocurrent measurement for InGaAs/GaAs MQW pin diode, known as QT1879, is also conducted to compare the photocurrent response with QW 20. The measurement uses a similar procedure applied on the QW20 GaAsBi p-i-n diode. The results are illustrated in Figure 5.2. The photocurrent operation in the InGaAs p-i-n diode is similar to the QW20 device. The critical difference is that the photocurrent region is shorter than the GaAsBi device. Although the peak of the photocurrent is much higher than QW20, the generated photocurrent region is only until wavelength 960nm. At 0.2V bias, the photocurrent response maintains a similar peak with the 0V bias except at temperature 120c, where the 0.2V photocurrent started decreasing. This phenomenon is significantly due to dark current performance in QT1879. The dark current performance of the QT1879 sample is lower than MQW GaAsBi p-i-n diodes at forward bias. As the dark current is small, it will generate a constant photocurrent at the forward bias region. QT1879 has the high-quality property of a strain-balanced MQW device compared to the QW20. The 0.4V photocurrent reduces when the temperature is higher than 60◦C. It is relatively similar to GaAsBi's behavior at a higher temperature. In addition, the device also has GaAs peak at high temperatures.

5.3.2 External Quantum efficiency for photocurrent Mechanism in GaAsBi MQWs p-i-n diodes

The following finding is to observe the external quantum efficiency produced by the devices. It is essential to estimate the photo-generated current created. The actual power landing on the device is determined by measuring the photocurrent of the commercial photodiode named FDGA05 (InGaAs-photodetector), which is measured at 0V bias. The output power density from the monochromator setup is estimated using the photocurrent result and the interpolated responsivity data from the provided datasheet. This power density is corrected to determine the actual power landing on the MQW device. Figure 5.3 depicts the estimation power from a monochromatic setup, as mentioned earlier in Section 3.5

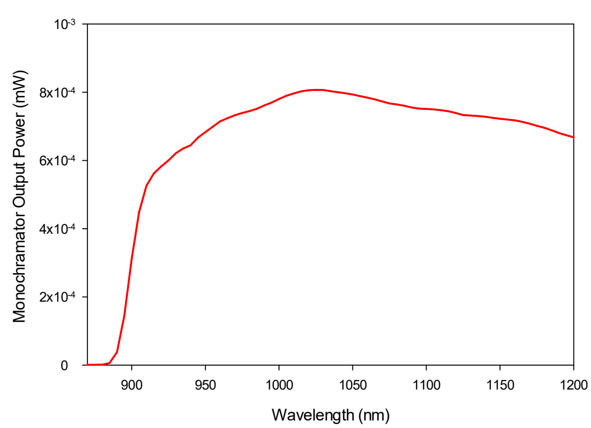

Figure 5.3: Output power from monochromatic setup that received by the measured devices

Then, the devices' external quantum efficiency (EQE) is determined based on the photocurrent of the MQW device, together with the calculated power landing on the device. External Quantum efficiency is the ratio of the total charge carrier generated concerning the total incident photon on the device, as shown in Equation 5.1. Figure 5.4 portrays the calculated temperature-dependent EQE for QW 20 device.

$$EQE(\lambda) = \frac{charg\ \ /s}{photon/s} \tag{5.1}$$

The EQE spectra explain the effective region of photon absorption and generation of charge carriers in the i-region upon the incident of light. During temperature changes from room temperature until 120◦C, QW 20 has a nearly flat region around 900 nm until 1060nm for all 0V, 0.2V, and 0.4V forward biases. However, at 1000nm, the photo-generated carrier starts to decrease and rapidly decreases after 1060 nm. At room temperature studies, 1060nm is identified as the energy band gap for the QW20 GaAsBi p-i-n diode [3]. The roll-off after 1060 nm is considered the absorption band edge of the device.

Moreover, when temperatures increase, the roll-off band edge for each response has small red-shifting and is wider compared to the response at room temperature. This happens because the bandgap of GaAsBi changes with temperature. Besides, the number of generated carriers at forward bias decreases as the temperature rises, particularly above 80°C. This reduction limits the current generated by light and affects the solar cell parameter calculation, such as short-circuit current and open-circuit voltage.

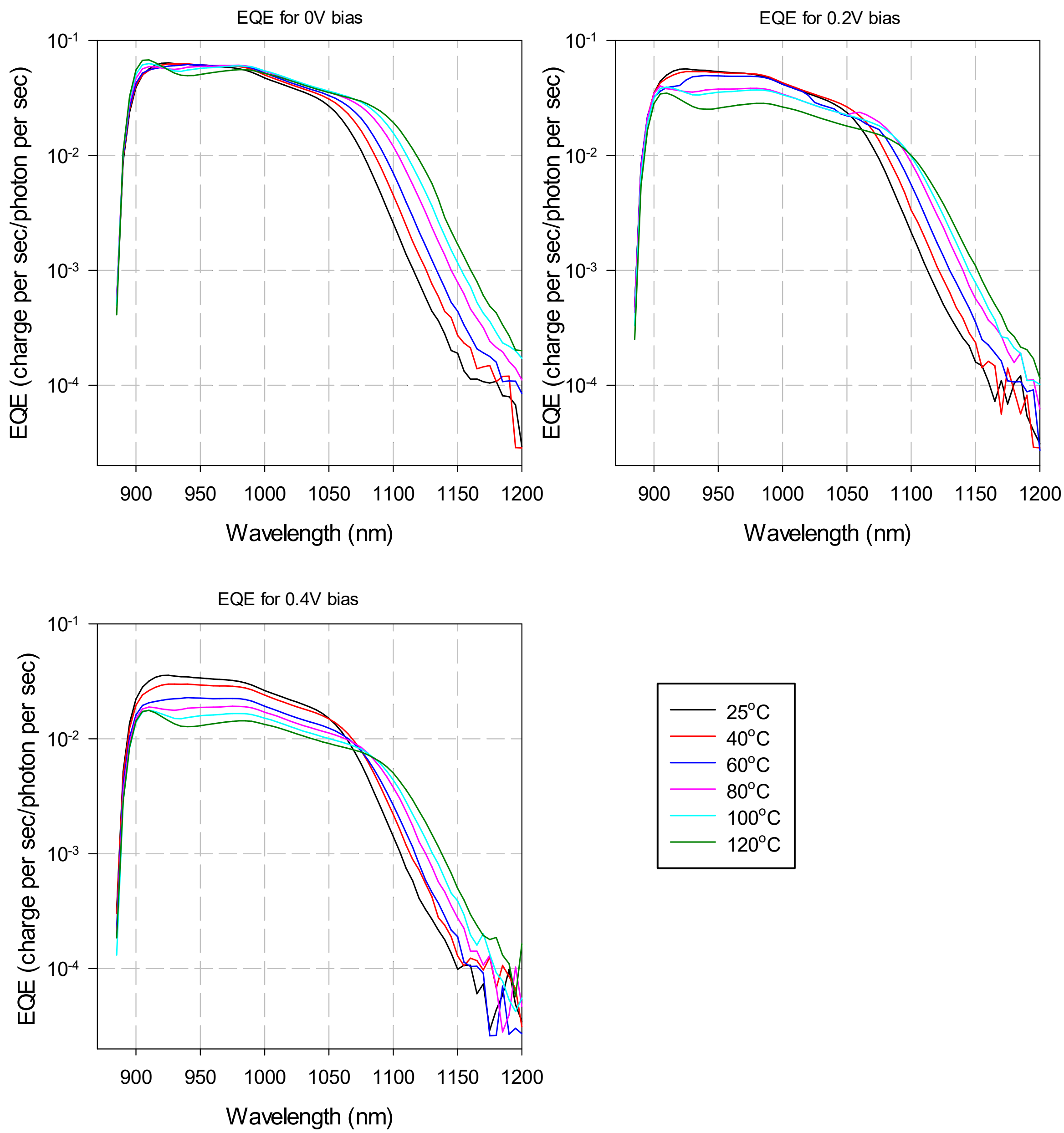

Figure 5.4: Calculated EQE for QW 20 device at different temperatures

5.3.3 Light-generated current Mechanism in GaAsBi MQWs p-i-n diodes

Next, the total light-generated current based on the illumination of incident power from the solar spectrum on the device is calculated by integrating the external quantum efficiency with the complete reference AM 1.5 solar power spectrum as described in Equation 5.2. In this case, the AM 1.5 solar power spectrum is an interpolated spectrum that only considers wavelengths from 850 nm to 1200 nm. The AM 1.5 spectrum is shown in Figure 5.5. This small spectrum range is selected because we want to investigate the performance of the GaAsBi MQW P-i-N devices concerning the fraction of the solar spectrum absorbed at the middle junction of the multi-junction solar cell.

$$light\ generated\ current, J_L = \int_{\lambda_{850nm}}^{1200nm} \left(EQE * Power_{AM\ 1.5\ reference}\right) d\lambda \tag{5.2}$$

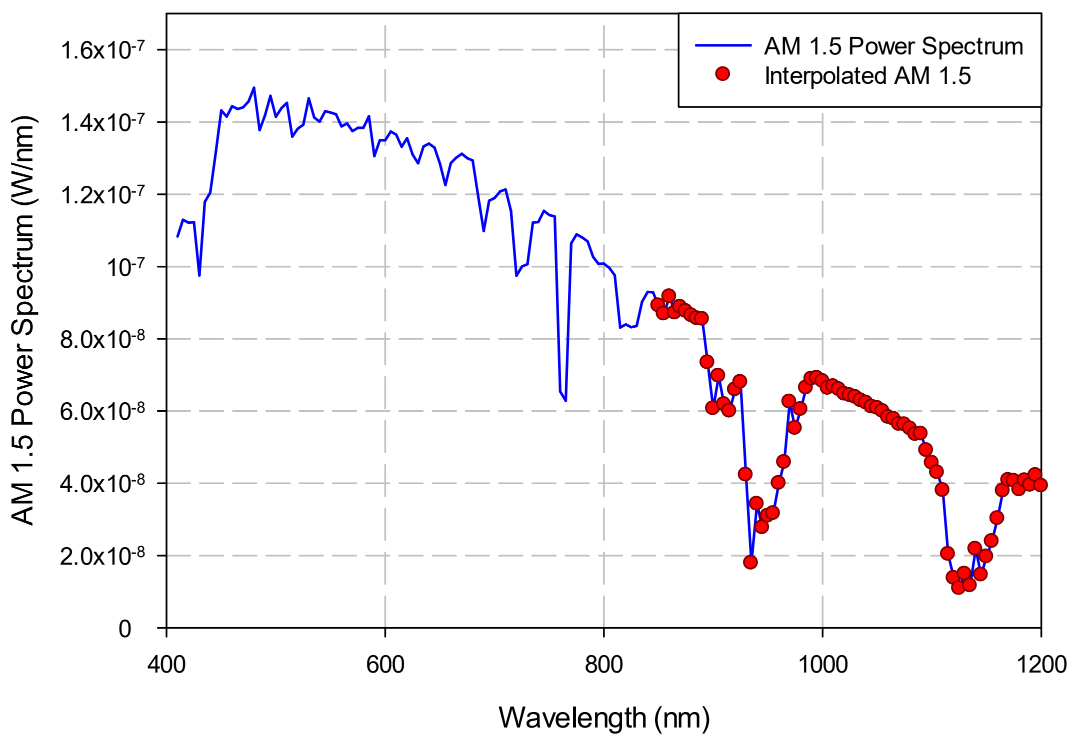

Figure 5.5: The interpolated AM 1.5 was used to estimate the light-generated current using EQE obtained from photocurrent measurement

Besides, the power spectrum higher than the band gap of the GaAs has already been filtered out by the GaAs filter during the photocurrent measurement. Furthermore, the photocurrent response not seeing any signal after 1200 nm. The light-generated current (J_{IL}) is calculated based on the given equation. This value will be used to calculate the total current mechanism and determine the short-circuit current for the series of quantum well devices. The calculated light-generated current for QW20 is shown in Table 5.1.

Table 5.1: The calculated temperature-dependent light-generated current for MQW 20 device using Equation 5.2 based on EQE results from forward bias 0V, 0.2V and 0.4V

QW20 - Temperature-dependent Current Density, J_{IL} each bias (mA/cm2)						
Temperature (C)	25◦C	40◦C	60◦C	80◦C	100◦C	120◦C
0V	0.402828	0.427758	0.445046	0.46896	0.48156	0.474611
0.2V	0.355344	0.365193	0.340133	0.306615	0.298511	0.243096
0.4V	0.224713	0.204902	0.164993	0.148091	0.133463	0.122575

The light-generated currents for slight forward bias are obtained for different temperatures as shown in Table 5.1. The current is expected to reduce as the bias increases and decrease more at high temperatures. It is significantly consistent with the photocurrent response and EQE trend. However, this result is still not yet considered as the short-circuit current. The total external current of the solar cells model is determined by applying a typical superposition model for solar cells [1], where the total current is shown in Equation 5.3. The results from applying this equation are shown in Table 5.2, and plotted in Figure 5.6

$$J = J_d - J_{IL} \tag{5.3}$$

Where; J_d is the dark current (in this calculation the dark current value is using the measured dark current obtained in Chapter 4), J_{IL} is the light-generated current from the photocurrent measurement using Equation 5.2 and the value is shown in Table 5.1.

Table 5.2: The calculated temperature-dependent light generated current for MQW devices

QW20 - Temperature-dependent Current Density, J_{IL} each bias (mA/cm2)						
Temperature (C)	25◦C	40◦C	60◦C	80◦C	100◦C	120◦C
0V	-0.40411	-0.42912	-0.44629	-0.4702	-0.48273	-0.4753
0.2V	-0.3547	-0.35915	-0.30692	-0.19061	0.081899	0.904263
0.4V	-0.11364	0.156731	1.345191	4.332336	12.39041	30.76539

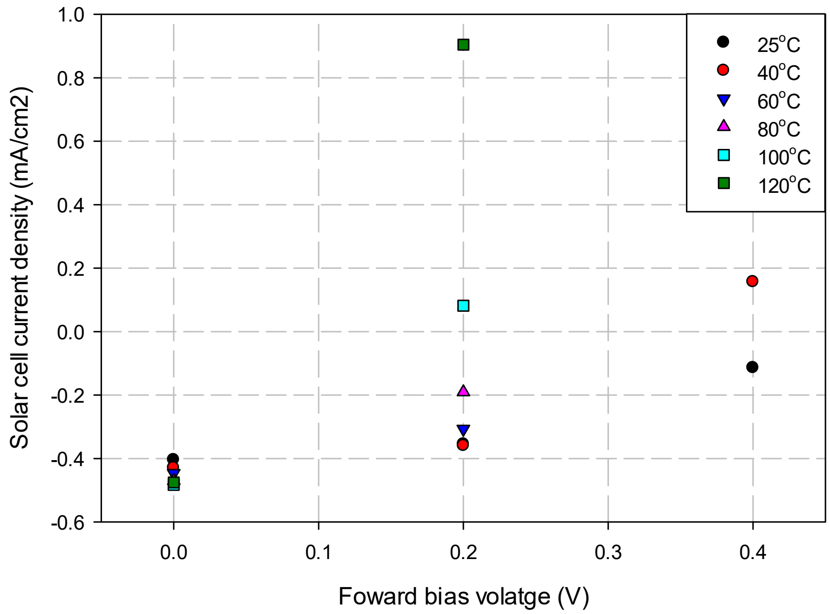

Figure 5.6: Temperature-dependent solar cell current density based on standard superposition model of solar cell.

Based on Figure 5.6, the total current of the device moderately increases as the temperature rises from room temperature to 80°C. However, the current amount decreases at a temperature of 120 °C. One of the factors is that, the dark current condition is very high at a temperature of 120 ºC. As discussed in section 4.6, most GaAsBi MQWs devices suffer a three-order increment of dark current when the device's temperature reaches 120 °C. The results from Figure 5.6 indicate the position of short-circuit current, but it is still challenging to identify the best position for open-circuit voltage. Therefore, the solar cell current density at each temperature is fitted with the Shockey diode equation in (5.4) to estimate the open-circuit voltage. The fitting results data are illustrated in Figure 5.7.

$$J = J_o exp\left[\frac{q(V-JR_{se})}{nkT}\right] + \frac{V-JR_{se}}{R_{sh}} - J_{IL} \quad (5.4)$$

Where; J is total solar cell current density, J_o is saturation dark current density, q is charge parameter, R_{se} is series resistance, n is ideality factor, k is Boltzmann's constant, T is temperature, V is applied forward bias, R_{sh} is shunt resistance and, J_{IL} is the light generated current. The fitting parameter is shown in Table 5.3.

Table 5.3: The complete Shockey diode's parameters value based on Equation 5.4 used to estimate solar cell current model for QW 20 at different temperature

Temperature	25◦C	40◦C	60◦C	80◦C	100◦C	120◦C	
n	1.857864	1.922121	1.930072	1.918492	1.865452	1.872629	
T	293	313	333	353	373	393	K
R (series)	1.41E-04	8.19E-05	4.76E-05	3.35E-05	2.90E-05	2.25E-05	Ohmcm2
R (shunt)	4.31E+00	3.34E+00	2.08E+00	1.47E+00	1.45E+00	1.36E+00	Ohm cm2
I0	3.87E-05	2.07E-04	1.18E-03	4.77E-03	1.61E-02	5.74E-02	mA/cm2
IL	4.04E-01	4.29E-01	4.47E-01	4.76E-01	4.99E-01	5.33E-01	mA/cm2

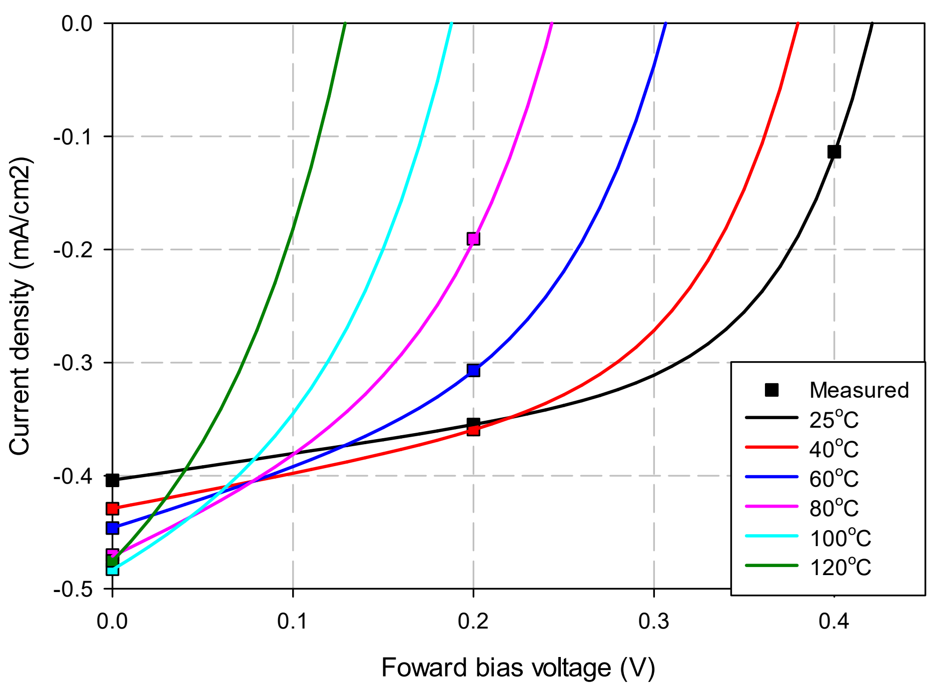

Figure 5.7: Measured and fitting results for solar cell current density based on Shockey diode equation for QW20 at different temperature.

It is found that the estimated total current mechanism under AM 1.5 illumination shows diode current behaviour and follows Shockey's diode equation. The short-circuit current increase until 100°C, then decrease at 120°C. The temperature-dependent strongly reduce the open-circuit voltage. Another parameter affected by temperature is the shunt resistor, which becomes very large about $1.5 \times 10^5 \Omega cm^2$, when approximating the dark current result. This value is applicable for all temperature-dependent fittings in all MQW devices. However, it reduces to a smaller value when fitting the illumination current. As a result, a low shunt resistor causes power loss in solar cells and a reduction of fill factor. This could be possible due to the internal defect in the GaAsBi devices during growth and fabrication. The measured and modelled illumination current in Figure 5.7 give significant advantage to determine the performance of solar cell parameters as described in Table 5.4.

Table 5.4: Solar cell parameters for the QW20 at different temperatures.

Temperature	25◦C	40◦C	60◦C	80◦C	100◦C	120◦C	
J_{SC}	0.404	0.429	0.446	0.472	0.482	0.4753	mA/cm2
V_{OC}	0.42	0.38	0.306	0.244	0.187	0.129	V
J_{MP}	0.294	0.310	0.294	0.293	0.297	0.276	mA/cm2
V_{MP}	0.32	0.27	0.21	0.16	0.12	0.08	V
FF	55.45	51.39	45.24	40.86	39.59	36.01	%

In this study, it is only significant to evaluate the performance of the MQW P-i-N device at nearly the GaAsBi band edge, which is between 900 nm to 1100 nm. This is because the GaAs filter in this measurement mostly filters out the light spectrum below 890 nm. Then at 1050 nm, the photocurrent started to decrease rapidly to zero.

5.4 Solar Simulator Current Behavior in GaAsBi MWQ p-i-n diodes

In this section, the MQWs devices are illuminated under a solar simulator without applying a GaAs filter. The solar simulator is the Newport LCS-100 9011A model. In order to meet the AM1.5 solar irradiances from the sun, AM 1.5G standard filter is coupled with the light source. This measurement is important to observe the overall performance of the MQWs GaAsBi pin diodes at high temperatures. Table 5.5 describes the solar cell's parameter performance.

Overall the short-circuit current increases and the open-circuit voltage decreases. Most short-circuit current is above 11 mA/cm2, whereas QW20 has a slightly lower short-circuit current than other devices as temperature increases. QW63 has the highest short-circuit current as temperature rises from room temperature to 120◦C. QT 1879 has the longest open-circuit voltage compared to the GaAsBi QW series. This high value of open-circuit voltage is due to the material's bandgap. Nevertheless, the fill factor achieved by QW05 is significantly close to the fill factor in the QT 1879 device. It is suggested that a strain device like QW05 has fewer defect and dislocation than other strain-balancing and relaxed devices.

Table 5.5: Solar cell parameters for MQWs GaAsBi devices and QT1879 under illumination of solar simulator at different temperatures.

QW05	I_{SC}	V_{OC}	I_{MP}	V_{MP}	P_{MP}	FF
25◦C	11.0606	0.61243	9.96211	0.500081	4.98186	73.54559
40◦C	11.0606	0.58188	9.27332	0.500153	4.63808	72.06525
60◦C	11.1014	0.52712	10.2571	0.400027	4.10311	70.11741
80◦C	11.3383	0.4768	10.4198	0.350142	3.64842	67.48706
100◦C	11.2971	0.42183	10.2165	0.300201	3.067	64.3591
120◦C	11.4171	0.37128	8.51148	0.300162	2.55482	60.27033

QW20	I_{SC}	V_{OC}	I_{MP}	V_{MP}	P_{MP}	FF
25◦C	9.95971	0.58056	8.15538	0.450235	3.67184	63.50233
40◦C	10.032	0.54864	7.52657	0.450229	3.38868	61.56808
60◦C	10.1043	0.48612	8.49818	0.350089	2.97512	60.56959
80◦C	10.2866	0.4278	8.6149	0.300163	2.58587	58.76176
100◦C	10.3589	0.3708	8.62924	0.250254	2.1595	56.22119
120◦C	10.4689	0.3148	8.71211	0.200038	1.74275	52.88105

QW40	I_{SC}	V_{OC}	I_{MP}	V_{MP}	P_{MP}	FF
25◦C	11.8114	0.5736	8.27553	0.450117	3.72496	54.98079
40◦C	12.0269	0.53086	8.77382	0.399942	3.50902	54.9607
60◦C	12.2386	0.4734	9.02847	0.350055	3.16046	54.54952
80◦C	12.6286	0.4167	9.26871	0.300114	2.78167	52.85991
100◦C	12.86	0.35744	9.38629	0.250199	2.34844	51.08999
120◦C	13.232	0.35152	9.883	0.199998	1.97658	42.49515

QW63	I_{SC}	V_{OC}	I_{MP}	V_{MP}	P_{MP}	FF
25◦C	12.768	0.41877	9.56416	0.300158	2.87076	53.69055
40◦C	15.0674	0.39307	10.146	0.300203	3.04587	21.71972
60◦C	15.8391	0.33376	10.6663	0.250293	2.6697	50.50079
80◦C	16.3543	0.28056	11.3214	0.199849	2.26257	49.31112
100◦C	16.8943	0.22745	12.1579	0.149897	1.82243	47.42682
120◦C	17.1874	0.17776	13.0732	0.100035	1.30779	42.8048

QT1879	I_{SC}	V_{OC}	I_{MP}	V_{MP}	P_{MP}	FF
25◦C	12.3277	0.8126	11.5272	0.650003	7.49274	74.79658
40◦C	12.904	0.76848	11.3667	0.650042	7.38883	74.51072
60◦C	13.044	0.72225	11.517	0.60018	6.9123	73.37095
80◦C	13.18	0.67088	11.4533	0.549867	6.2978	71.22433
100◦C	13.228	0.61542	11.2692	0.49993	5.63379	69.20465
120◦C	13.228	0.56388	10.9389	0.450057	4.92312	66.00236

5.5 The performance of open-circuit voltage for MQW GaAsBi pin diode

Figure 5.8 illustrates the temperature-dependent open-circuit voltage (Voc) for MQW pin diodes and the QT 1879 devices. The trend reveals a general decrease in all open-circuit voltage values as the temperature rises, indicating the significant influence of temperature changes on the Voc, particularly at higher temperatures. QW63 exhibits the lowest voltage among the devices, while the other three GaAsBi QW series are closely clustered between 0.6V to 0.3V. However, the open-circuit voltage for the GaAsBi MQW series is moderately lower than the InGaAs/GaAs sample. One reason for this is that the QT sample's quality structure has fewer defects than the GaAsBi series. Based on the standard solar cell model the equation for open-circuit voltage can be described as Equation 5.5.

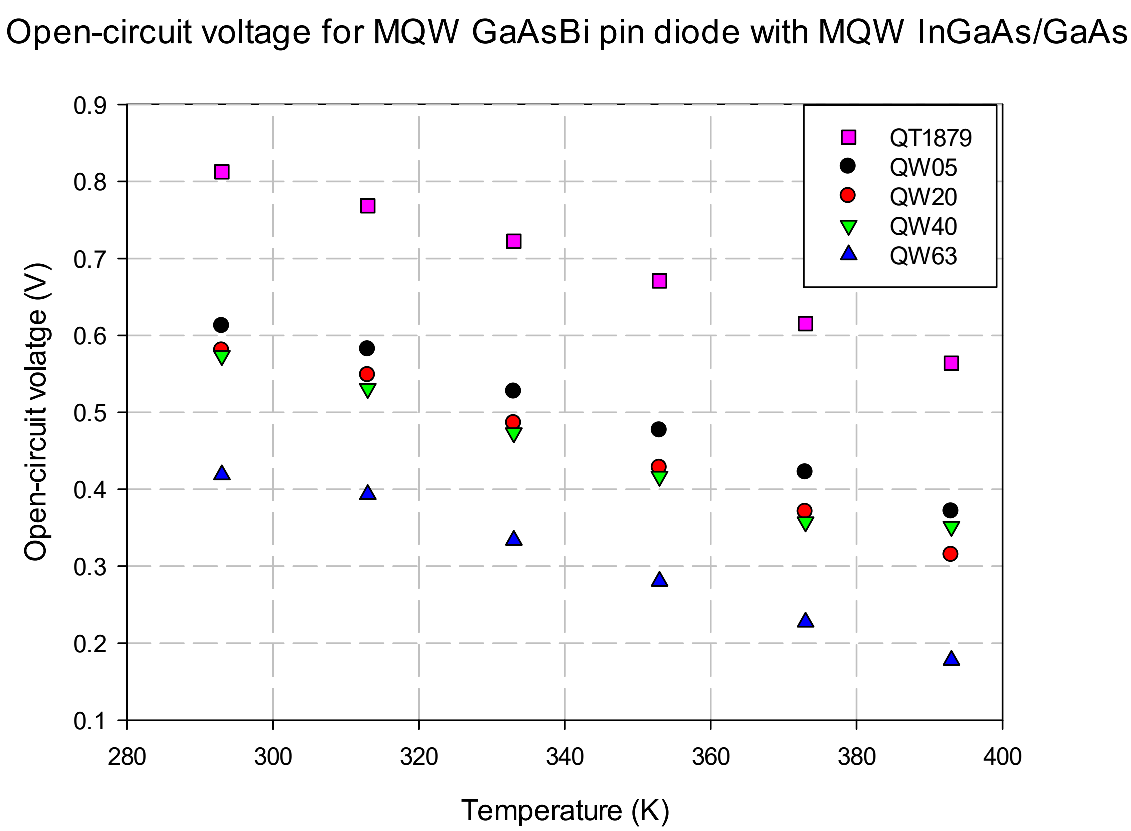

Figure 5.8: Temperature-dependent open-circuit voltage for MQW pin diodes and MQW InGaAs/GaAs.

$$Voc = \frac{nkT}{q}\ln(\frac{I_L}{I_o} + 1) \quad (5.5)$$

Where; n is ideality factor, q is charge parameter, k is Boltzmann's constant, T is temperature, I_o is saturation dark current and, I_L is the light generated current.

From Equation 5.5, the Voc appears to have a linear relationship with temperature. However, the saturation current dark current increases dramatically with temperature-dependent due to the characteristic of intrinsic carrier concentration, *ni,* as explained previously in Chapter 4, Equation 4.3 and 4.4. In contrast, the change in the light-generated current I_L is relatively small compared to the saturation dark current. This is because the characteristic of I_L is related to the doping concentration parameter, which is not rapidly influenced by temperature changes. Conversely, the increased intrinsic carrier concentration with higher temperature will strongly affect the open-circuit voltage. In addition, from the previous dark current results in Chapter 4, it is clearly shown that most MQW devices have an ideality factor above 1.6, which indicates the device is dominated by non-radiative recombination at high temperatures.

The device structure for QW63 is identified as strain-relaxed. This means that the relaxation effect significantly causes the Voc of the QW63 to be much lower than that of other devices. The formation of dislocations and impurities in the structure layer creates a recombination center, facilitating a non-radiative recombination mechanism and increasing the dark current. The strain effect also modifies the band structure of the device, decreasing the band gap and making it easier for the thermal excitation of the charge carrier, which contributes to a higher dark current. Additionally, as the strain decreases the band gap and enhances recombination, it diminishes the separation between quasi-Fermi levels, thus lowering the open-circuit voltage performance.

5.6 The Fill Factor, FF of MQW GaAsBi pin diode

Figure 5.9 shows the fill factor (FF) performance of a multiple quantum well (MQW) GaAsBi p-i-n diode with varying temperatures alongside multiple MQW InGaAs/GaAs configurations (labeled QT1879). The fill factor, a critical parameter in photovoltaic devices, represents the ratio of the maximum power point to the product of open-circuit voltage (Voc) and short-circuit current (Isc). It gives insight into the quality of the device's power conversion efficiency. In this graph, the fill factor (FF) generally decreases with increasing temperature for all the quantum well (QW) configurations. This trend can be explained by the effect of temperature on various internal processes within the diode, such as an increase in carrier recombination, reduction of open-circuit voltage, and series resistance effect.

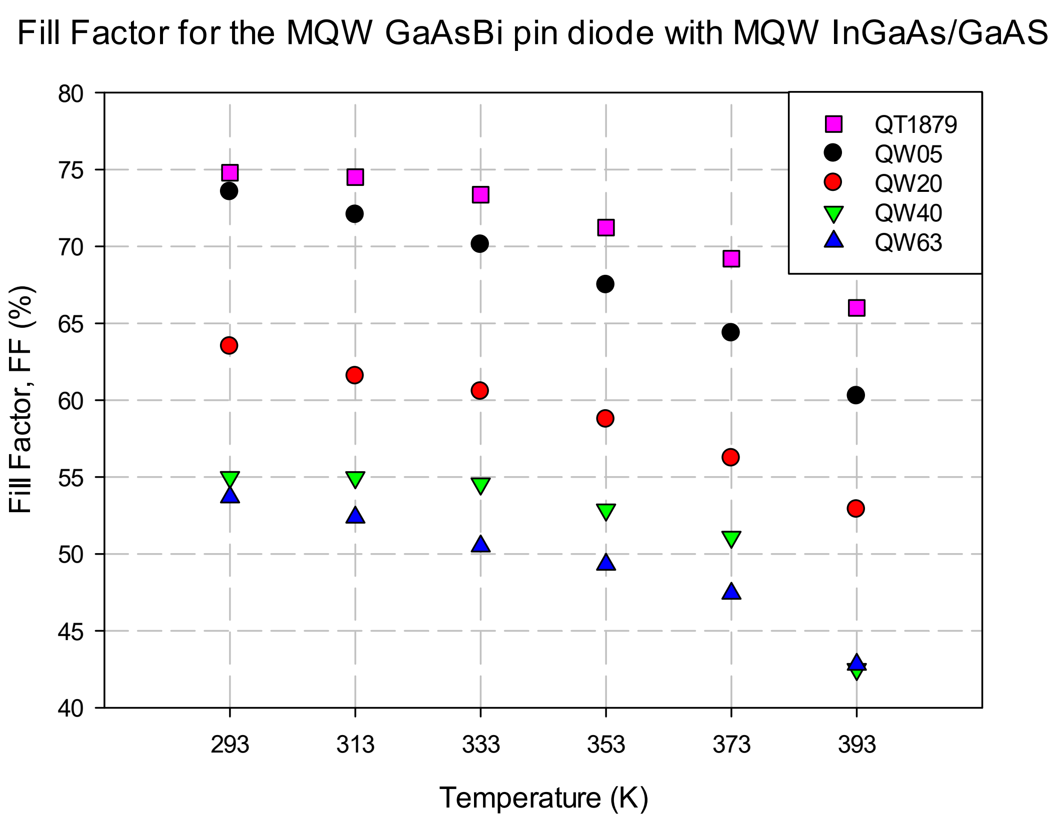

Figure 5.9: Temperature-dependent Fill Factor for MQW pin diodes and MQW InGaAs/GaAs.

The QT1879 device reaches the highest fill factor across all temperature ranges, starting from around 75% at 293 K and dropping to around 60% at 393 K. The higher FF suggests that this structure has better material quality or less strain, leading to fewer recombination centers and lower resistive losses, even at elevated temperatures. The higher performance of QT1879 suggests it has a more optimized design or material properties that minimize the impact of these degrading factors.

In contrast, the configuration of GaAsBi devices portrays lower FFs across the temperature spectrum compared to QT1879, with QW63 performing the poorest, dropping below 50% at 393 K. The difference in performance between these structures could be due to varying levels of strain relaxation or defects in the quantum well layers, leading to higher recombination rates or increased series resistance as temperature rises.

However, the FF result for QW05 has a higher fill factor than the rest of the GaAsBi devices and is relatively close to the InGaAs/GaAs device. It is suggested that the devices have a lower strain effect than other GaAsBi devices, which balance short-circuit current and open-circuit voltage performance. Besides, the barrier structure layer for QW05 is much thicker than the rest of the devices, significantly facilitating a better carrier confinement mechanism in the quantum well. When the barrier is thicker, it helps isolate the quantum wells more effectively, reducing carrier diffusion into the barriers. This condition improves charge separation efficiency, which enhances both the photocurrent and the open-circuit voltage, improving the fill factor.

The GaAsBi device has great potential to become an ideal 1 eV band gap material for multi-junction solar cell applications. Despite their advantages, GaAsBi solar cells face significant weaknesses and limitations, requiring an efficient strategy to develop a quality solar cell device ready for commercial viability. Introducing bismuth (Bi) into the GaAs lattice causes strain and increases the likelihood of defects such as dislocations and non-radiative recombination centers. When epitaxial layers with lattice mismatches are grown, GaAsBi material tends to have a high density of threading dislocations. These growth defects reduce carrier lifetime and increase the recombination mechanism, which influences the device's current mechanism behavior and decreases the solar cell's efficiency.

The optimal growth temperature for GaAs is typically around 600°C to establish good material quality with relatively minimum defects. However, this temperature is too high for Bi incorporation, as Bi desorbs from the surface. This growth temperature issue creates a fundamental trade-off in the GaAsBi solar cell design process. Lowering the growth temperature will increase the Bi content incorporation to achieve the required band gap reduction but degrade material quality. In contrast, increasing the temperature will improve material quality; however, it will reduce Bi content, thus limiting the ability to achieve the desired 1 eV band gap. The growth temperature of GaAsBi solar cells for developing a 1 eV band gap demonstrates a complex challenge due to the competing factors of material quality and Bi incorporation. Maintaining a temperature that is significantly low enough to incorporate Bi without introducing excessive defects is the key to establishing the high performance of solar cells.

The current implementation for developing MQW GaAsBi pin devices shows relatively low open-circuit voltage, maximum power, and fill factor. The fill factor from the strain-balanced GaAsBi series is below 65%, and it decreases to less than 65% when the number of quantum wells increases to 63. In contrast, the strain-balanced InGaAs/GaAs quantum well (QT1879) demonstrates a higher fill factor of about 75% at room temperature. This achievement is close to the InGaAs/GaAsP MQW model by S. Kotamraju et al., which achieved an 85% fill factor [10]. This model also aligns with the fill factor based on strain-balanced MQW GaAsP/InGaAs demonstrated by N.J. Ekins-Daukes et al [11]. However, K. Toprasertpong et al. demonstrated that as the number of quantum wells increased, for example, with a 70-period quantum well, the fill factor for InGaAs/GaAsP quantum well decreased to 65%. This result suggests that the device has lower crystal quality and significant growth defects in the i-region due to the large strain in the quantum well structure [12]. Additionally, A. Gonzalo et al. suggest that a rapid thermal annealing strategy on type-II GaAsSb/GaAs superlattice devices significantly enhances solar cell performance, achieving a fill factor of about 64% [13].

Further improvement on the growth temperature window to balance Bismide incorporation and material quality requires a new strategy of growth temperature and advanced technology. This approach could minimize defect formation while allowing sufficient Bismide incorporation to maintain the desired 1 eV band gap. In addition, incorporating other lattice-mismatched alloy materials that can moderately grow with a GaAsBi structure may allow for a broader range of growth temperatures and compromise material quality.

Leveraging optimized growth windows, strain-compensation strategies, alternative epitaxial methods, and surface passivation can elevate the performance levels of MQW GaAsBi solar cells than other multi-quantum well (MQW) solar cell technologies. These alternative approaches for designing GaAsBi devices can enhance solar cell performance parameters such as short-circuit current, open-circuit voltage, and fill factor.

5.7 Carrier Trapping Effect at Low Temperatures

Recently, the photovoltaic performance of a series of GaAsBi/GaAs MQW p–i–n diodes was investigated [4]. The results showed that strained GaAsBi MQWs could provide a comparable absorption edge to state-of-the-art, strain-balanced, interlayered InGaAs/GaAsP [4] devices. However, two issues were observed with the GaAsBi devices: firstly, the onset of spectral absorption was gradual, limiting the voltage of the devices; secondly, the quantum efficiency of the GaAsBi above the absorption edge was lower than expected, despite dark capacitance-voltage measurements indicating near full depletion of the device's i-regions.

The carrier trapping effect is possibly caused by poor carrier extraction, as demonstrated in GaInAsN and InGaAs MQW [5,6]. Since depositing Bi, the energy bandgap of GaAs decreases due to the increasing valence band offset. Thus, holes that trap in QWs affect the generation of charge carriers in QW and the GaAs barrier. In this experiment, the current-voltage (I-V) was measured in the dark and during illumination at room temperature down to 15 Kelvins. The measurement is conducted on QW20 only. The experimental setup and procedure have been explained in section 3.6.

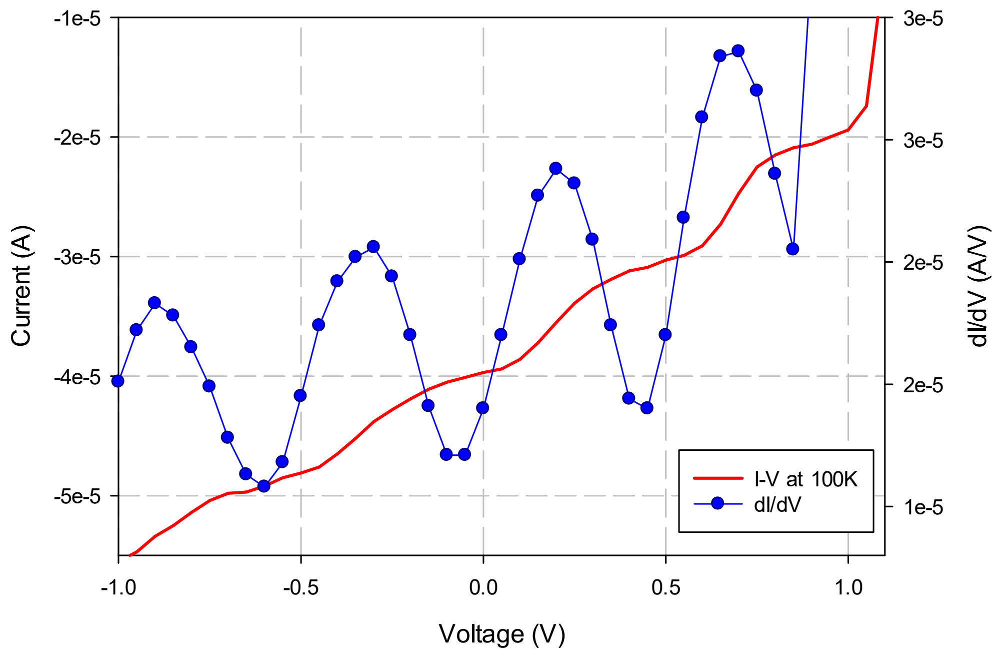

Figure 5.10: The low temperature I-V curve during illumination and differential of I-V curve [9].

The red line in Figure 5.8 illustrates the low-temperature I-V curve for QW20 at 100 Kelvin under illumination by 660nm red led. The blue dot represents the differential of low I-V concerning the applied bias voltage (dI/dV). The I-V curve shows a stairs-like behaviour below 1V bias voltage. The slope region corresponds to the peak of the sinusoidal differential I-V curve. This phenomenon is merely a similar finding observed by Khalil et al. [5,7,8].

In the case of QW GaAsBi, the carrier thermal escape time of the hole in the valence band becomes longer than the electron in the conduction band due to the large valence band offset in the GaAsBi materials. This asymmetric carrier escape time condition explains that electrons can escape from the quantum well while the holes (with no electron to recombine) get trapped and accumulate in the valence band offset. As a result, holes trapping in the large valence band edge during illumination will screen the built-in electric field and reduce depletion width in the intrinsic region of the quantum well device. This can be seen during the flat area of the low I-V curve. The disparity of escape rate between these two photo-excited carriers has become obvious as the temperature is reduced [9]. The thermal escape time behaviour is shown in Figure 5.9. The hole carriers' thermal escape time is likely four orders of magnitude compared to the electron carrier.

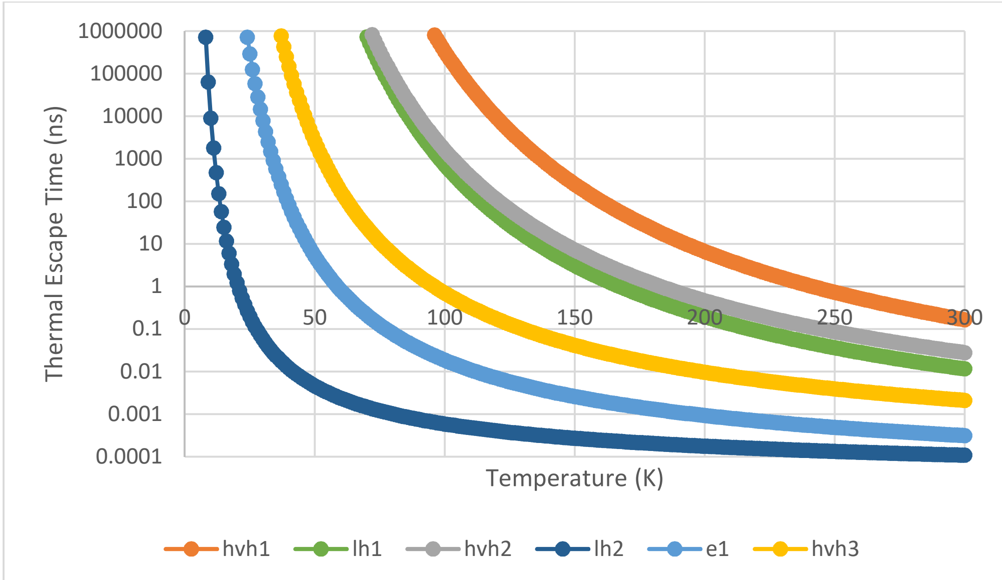

Figure 5.11: Thermal escape time for holes and electron carrier for QW20 [9].

5.8 Summary

Early findings from this chapter are to study the behavior of photocurrent response as temperature increases from room temperature to 120◦C. The reduction of photocurrent response is observed when the temperature increase started at 80◦C and was seen at 120◦C. Temperature dependence does not affect zero bias and slight forward bias compared to the photocurrent response at 0.4V bias. The second significant result is to estimate and model the solar cell parameters based on photocurrent response illuminated under monochromatic light. Then, the devices are tested under the LCS-100 Newport solar simulator. Both findings agree with the photocurrent response—most MQWs GaAsBi devices have low open-circuit voltage and smaller fill factor than InGaAs QT1879. The third observation is associated with thermal carrier escape time. It is found that the thermal escape time for a hole carrier is four orders of magnitude higher than an electron.

Reference

[1] K. W. J. Barnham, G. Duggan, “A new approach to high-efficiency multi-band-gap solar cells”, Journal of Applied Physics, Vol. 67 no. 7, (1990), pp. 3490-3493, doi: 10.1063/1.345339

[2] F. Harun, "Characterisation of GaAsBi/GaAs Multiple Quantum Wells for Photovoltaic Applications," ed: University of Sheffield; 2020, 2013.

[3] Richards, R.D., et al., MBE grown GaAsBi/GaAs multiple quantum well structures: Structural and optical characterization. Journal of Crystal Growth, 2015. 425: p. 237-240.

[4] Richards, R.D., et al., Photovoltaic characterisation of GaAsBi/GaAs multiple quantum well devices. Solar Energy Materials and Solar Cells, 2017. 172: p. 238-243.

[5] Khalil, H.M., Royall, B., Mazzucato, S. et al. Photoconductivity and photoluminescence under bias in GaInNAs/GaAs MQW p-i-n structures. Nanoscale Res Lett 7, 539 (2012). https://doi.org/10.1186/1556-276X-7-539

[6] Y. Yazawa, T. Kitatani, J. Minemura, K. Tamura and T. Warabisako, Carrier generation and transport in InGaAs/GaAs multiple quantum well solar cells, in IEEE 1st World Conference on Photovoltaic Energy Conversion - WCPEC, Waikoloa, HI, USA, 1994.

[7] H.M. Khalil, S. Mazzucato, S. Ardali, O. Celik, et al, “Temperature and magnetic field effect on oscillations observed in GaInNAs/GaAs multiple quantum wells structures”, Materials Science and Engineering: B, Vol.177 (10), 2012, pp. 729-733, doi.org/10.1016/j.mseb.2011.12.022

[8] Khalil, H.M., Balkan, N. Carrier trapping and escape times in p-i-n GaInNAs MQW structures. Nanoscale Res Lett 9, 21 (2014). https://doi.org/10.1186/1556-276X-9-21

[9] R.D. Richards, T.B.O. Rockett, M.R.M Nawawi, F. Harun, et al, “Light-biased IV characteristics of a GaAsBi/GaAs multiple quantum well pin diode at low temperature”, Semiconductor Science Technology, Vol.33 (2018) 094008, IOP Publishing, doi: 10.1088/1361-6641/aad72a

[10] Siva Kotamraju, M. Sukeerthi, Suresh E. Puthanveettil, “Modeling of InGaP/InGaAs-GaAsP/Ge multiple quantum well solar cell to improve efficiency for space applications”, Solar Energy, vol. 186, 2019, pp. 328-334, doi.org/10.1016/j.solener.2019.05.015.

[11] N. J. Ekins-Daukes, J.M Barnes, K.W.J. Barnham et al., "Strained and Strain-Balanced Quantum Well Devices for High-Efficiency Tandem Solar Cells,", Solar Energy Materials and Solar Cells, Article vol. 68, no. 1, pp. 71-87, Apr 2001, doi: 10.1016/s0927-0248(00)00346-9

[12] K.Toprasertpong, H. Fujii, T. Thomos et. al, "Absorption threshold extended to 1.15eV using InGaAs/GaAsP quantum wells for over-50%-efficient lattice-matched quad-junction solar cells",29th EU PVSEC, Amsterdam 2014, Progress in Photovoltaics Research and Application, vol.24, no. 4, pp.533-542, 2016, doi.org/10.1002/pip.2585.

[13] A. Gonzalo, L. Stanojević, D. Fuertes Marrón, A. Guzman, A. Hierro, J.M. Ulloa, "1 eV GaAsSbN–based solar cells for efficient multi-junction design: Enhanced solar cell performance upon annealing", Solar Energy, vol. 221, 2021, pp.307-313, https://doi.org/10.1016/j.solener.2021.04.041.

Chapter 6

Conclusion

This research focuses on the temperature-dependent characteristic of the MQW GaAsBi p-i-n diode. The motivation for investigating the behavior of the devices at high temperature is to provide a useful study for the devices to work under high solar concentrators. At higher temperatures, the device's bandgap properties will be affected, and this condition is theoretically altering the photovoltaic effect performance and solar cell parameters, especially the open circuit voltage. Therefore, further study and experimental measurement are required to investigate the behavior of the MQW GaAsBi p-i-n diode to evaluate the solar cell parameter performance at a higher temperature.

The first key finding is the behaviour of dark temperature current for both GaAsBi p-i-n device structures that are bulk and multiple quanta well. The bulk series are growth based on two strategies: varying the bismuth flux and changing growth temperature. For MQW, p-i-n diodes are categorized into three different strain conditions. It is a strain, strain-balanced and relaxed device. Dark currents in all devices fitted well with classical Shockey's diode equation. The dark current of the MQW series is much better than the bulk series. The ideality factor obtained is more than one but less than two, showing that recombination current relatively occurred. However, the dark current is fitted well for bulk series with an ideality factor equal to two, making the series merely dominant by recombination current. The saturation current from the fitting analysis is also high, especially for higher bismuth concentrations. The growth series by temperature varying is suggested to be better than the flux control approach. Therefore, the optimum and careful selection of growth temperature is recommended as the main parameter for producing a high-quality GaAsBi device.

The second objective of this study is to assess the performance of the GaAsBi MQW pin diode as a solar cell at high temperatures. The performance evaluation is based on photocurrent measurements under monochromatic light, estimation of the standard reference AM 1.5 power spectrum, and measurements under illumination from a solar simulator. A significant part of our study is dedicated to the process for determining the short-circuit current, open circuit voltage, and fill factor, which is thoroughly discussed in the thesis. The short-circuit current increases as the temperature rises but begins to decrease at 80°C and above. One contributing factor is the high dark current at forward bias, which limits the production of photo-generated carriers. It is expected that the open circuit voltage will decrease with changes in temperature. The solar cell parameters based on photocurrent measurements are relatively less accurate but can still be used to provide a preliminary performance estimation. It is recommended to conduct photocurrent measurements using a solar simulator setup.

The third finding is to investigate the carrier trapping effect on the MQW pin diode. This experiment is only conducted on QW20 due to technical limitations. In this experiment, the current-voltage (I-V) was measured in the dark and during illumination from room temperature down to 15 Kelvins. The device was placed in a close-cycle He-cryostat held under vacuum and illuminated by a 660 nm LED. In the case of QW GaAsBi, the carrier thermal escape time of the hole in the valence band is longer than the electron in the conduction band due to the bandgap reduction in GaAsBi is caused by large valence band offset in the GaAsBi materials. This asymmetric carrier escape time condition explains that electrons can escape from the quantum well while the holes (with no electron to recombine) get trapped and accumulate in the valence band offset. The calculated carrier thermal escape time for the hole (heavy hole) is four orders higher than an electron.

At the moment, depending on the current work and our MBE growth technology for developing GaAsBi, these devices could be better, and their performance for solar cell devices is moderately lower compared with other devices such as InGaAs and dilute nitride. The defects in GaAsBi solar cells, particularly those targeting a 1 eV junction, are significantly influenced by the growth temperature, which directly affects material quality and device performance; several types of defects emerge during the growth process and can drastically reduce the solar cell's performance. The importance of producing good quality GaAsBi devices for 1eV junction solar cells is to achieve a balance between incorporating sufficient bismuth (Bi) for a lower band gap and minimizing defects to maintain the high efficiency of solar cell application

The research on growth at low temperatures (around 300°C–400°C) is necessary to incorporate sufficient Bi into the GaAs matrix to achieve a 1 eV band gap. However, low-temperature growth creates limitations where atoms on the surface during growth do not have enough energy to find optimal lattice sites, resulting in an increased density of point defects, such as vacancies, dislocation, and antisite defects (where the Ga atom positions on As sites). In addition, low-temperature growth often results in lattice strain between the GaAs and GaAsBi layers due to lattice mismatch caused by Bi's larger atomic radius than Ga or As. These growth defects influence the generation of more non-radiative recombination, reducing the carrier lifetime and limiting the solar cell's open-circuit voltage (VOC) and fill factor (FF). Non-radiative recombination phenomena cause energy loss in the form of heat, which diminishes the efficiency of the solar cell. Furthermore, Bi atoms aggregate at low temperatures, forming Bi clusters, which leads to phase separation results in a non-uniform distribution of Bi in the GaAsBi alloy, causing localized regions with different band gaps. The inhomogeneity also causes current mismatch and degradation of the photocurrent response of the solar cell.

Conversely, a different limitation emerges when growth temperatures of GaAsBi exceed approximately 400°C. The bismide atom begins to desorb from the surface, leading to incomplete Bismide incorporation. Thus, it produces higher band gap energies above the desired 1 eV junction, reducing the sub-cells ability to absorb longer-wavelength photons and decreasing the short-circuit current. Further work is needed to solve this issue, as it directly impacts the performance of GaAsBi solar cells.

It is vital to optimize the growth temperature and other process parameters for future work to balance Bi incorporation and crystal quality. This approach will help to minimize defects and improve the performance of GaAsBi solar cells with a 1 eV junction. An effective growth temperature window can balance the Bismide incorporation and device quality. The lower temperatures enable Bi incorporation but require a strategy to mitigate defect formation. One approach to achieve this condition is to use modulated temperature profiles during growth, where higher temperatures are used to grow the GaAs layer, and suitable lower temperatures are applied for Bi incorporation. This method could reduce defects without compromising Bi incorporation.

Thus, this optimization process can reduce growth defect densities, enhance carrier lifetime, and improve open-circuit voltage and fill factor.

In addition, thermal annealing processes can help improve the quality of materials and reduce defects that occur during low-temperature growth, such as point defects and dislocations. Applying convenient low-temperature annealing methods can improve the uniformity of bismuth without causing it to desorb, which can further minimize issues related to phase separation. Therefore, optimizing annealing temperatures can enhance the design process of GaAsBi device structures.

Incorporating strain-compensating layers, such as indium gallium arsenide (InGaAs), dilute nitride, antimonite (Sb) or other III-V semiconductor materials, could mitigate the lattice mismatch between GaAs and GaAsBi. Such layers could improve the solar cell's performance by minimizing strain-induced defects. Applying these compensating layers in a multi-quantum well (MQW) structure may further improve absorption and charge carrier separation, enhancing both the short-circuit current and the fill factor.

To further enhance control over defect formation, alternative epitaxial growth techniques like MOVPE could offer more precise control over the incorporation of Bi at different temperatures. These techniques can potentially enable the deposition of GaAsBi layers with fewer defects by maintaining high crystal quality at lower growth temperatures, thereby improving Voc, Jsc, and FF. The MOVPE technology allows better control of gas-phase precursors and improves surface quality. Combined with advanced growth conditions, this could reduce phase separation and defect formation, enabling higher-performance GaAsBi solar cells.

Further research is recommended on the characteristics of GaAsBi as solar cell devices in the future. This includes conducting temperature-dependent capacitive-voltage measurements at low temperatures to study doping concentration properties and better understand the carrier trapping effect. Additionally, conducting temperature-dependent photocurrent measurements slightly further forward and reverse bias will help study the bandgap reduction effect in the MQW device structure, providing more information about carrier extraction and absorption band-edge due to the bandgap changes caused by temperature variations.

Appendices

Appendix A: Dark Current Measurement GaAsBi Bulk Series at Room Temperature

Dark current measurements for GaAsBi Bulk pin diodes at room temperature are shown in Appendix A. These dark currents are only for the Bismide Flux series (STG 3D, STG34, and STG39) and the Temperature growth series (STG 3C and STG 38). All measured data are fitted with Shockey diode's equation as described below. Table A shows all the relevant fitting parameters.

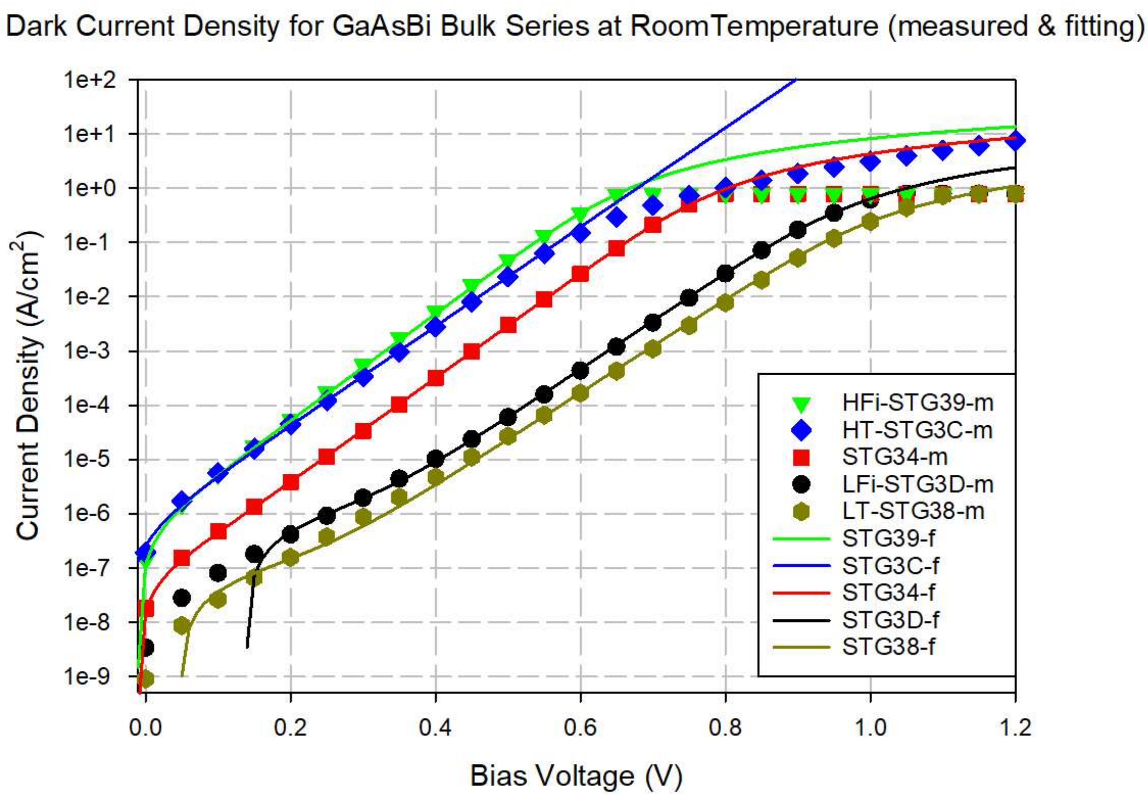

Table A: Dark current density fitting parameters for GaAsBi bulk pin diodes at room temperature.

Tgrow	Tgrow (◦C)	FBi (nA)	Eg (eV)	J0 (mAcm-2)	n	Rs (Ωcm^2)
STG3C	355	1.06	1.17	6.48E-04	1.88	1.05E-04
STG34	375	1.06	1.19	5.12E-05	1.81	2.67E-05
STG38	405	1.06	1.32	4.36E-07	1.93	5.19-05
STG3D	375	0.50	1.32	1.10E-06	1.85	3.88E-04
STG39	375	2.12	1.07	7.91E-04	1.75	1.54E-05

Appendix B: The Nomarski Microscopy Images for several GaAsBi p-i-n diodes.

These measurements were conducted by Dr. Thomas B.O. Rockett and reported in

"Growth of GaAsBi pin diodes using MBE", Doctoral Thesis University of Sheffield, April 2019

The purpose of this Normaski measurement is to observe the presence of defects and detect any strain relaxation on the device layer. The growth information about the devices is described in Table B.

Table B: Growth parameters fro STG 38, STG 3D, STG34 and STG3B

Series	**Tgrow (°C)**	**FBi (× 10-7 mBar)**	**[Bi] (%)**	**Eg (eV) inferred from [Bi] following [9]**
STG 38	405	1.06	1.37	1.31
STG 3D	375	0.50	1.3	1.31
STG 34	375	1.06	3.25	1.19
STG 3B	375	1.50	4.12	1.14

Figures 4.6 to 4.9 depict several droplet-like defects on the device surface. Notably, the device with a higher bismide concentration exhibited more defects than those with a lower concentration. The author also segmented the image and counted the number of droplet-like defects. The findings suggest that no significant correlation exists between the droplet density and bismide content for devices with less than 4% bismide incorporation. The defects are likely gallium droplets, possibly from the growth process, such as cell spitting or background impurities from the growth chamber.

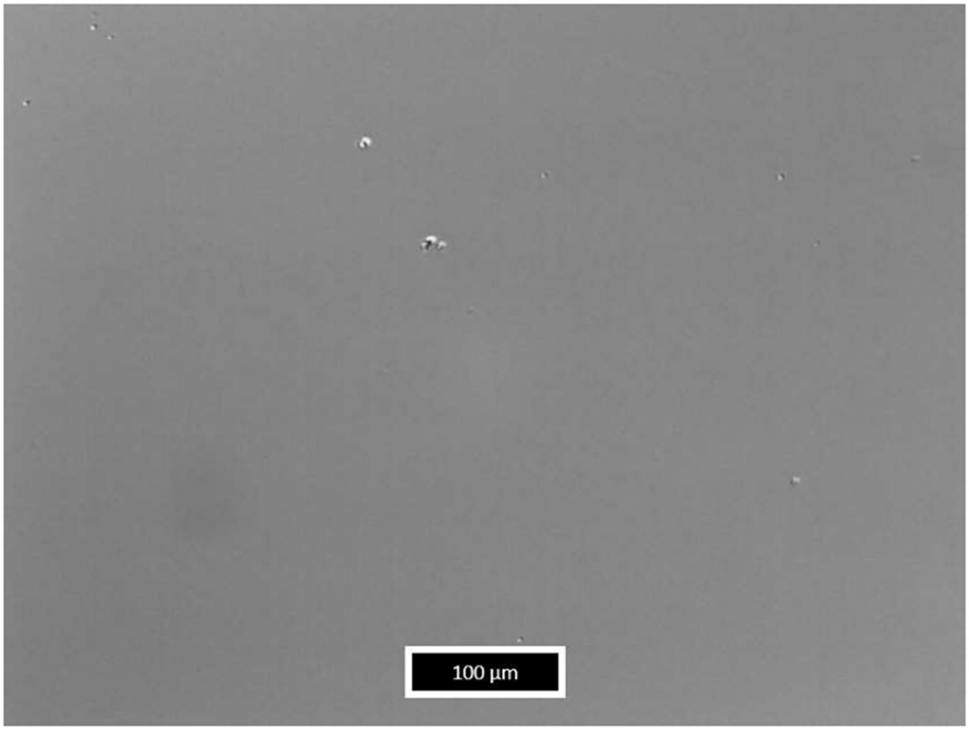

FIGURE 4.6: Nomarski image of STG-38 (1.37% Bi) at 10x magnification

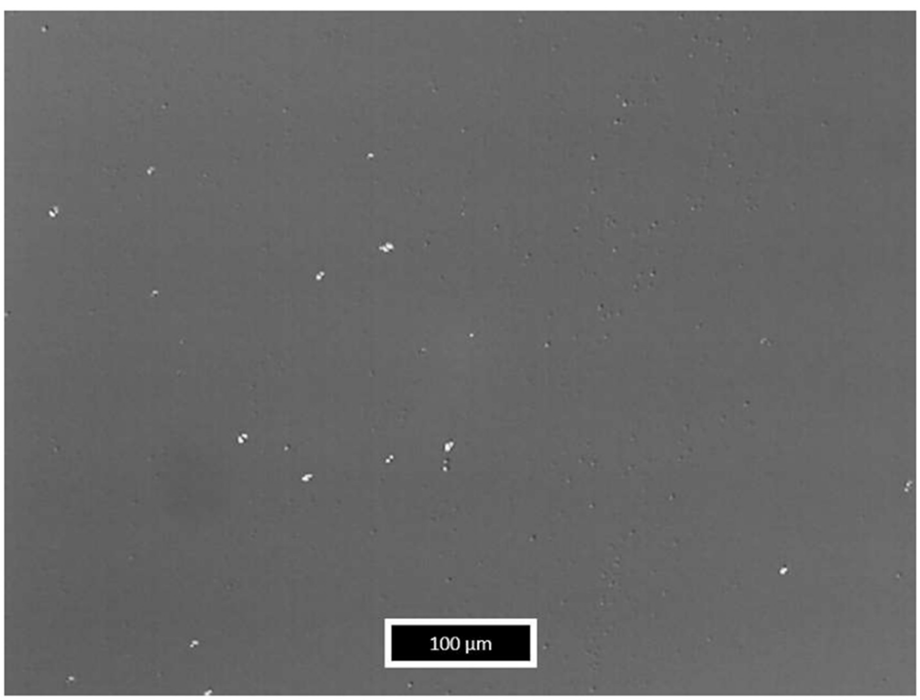

FIGURE 4.7: Nomarski image of STG-3D (1.31% Bi) at 10x magnification

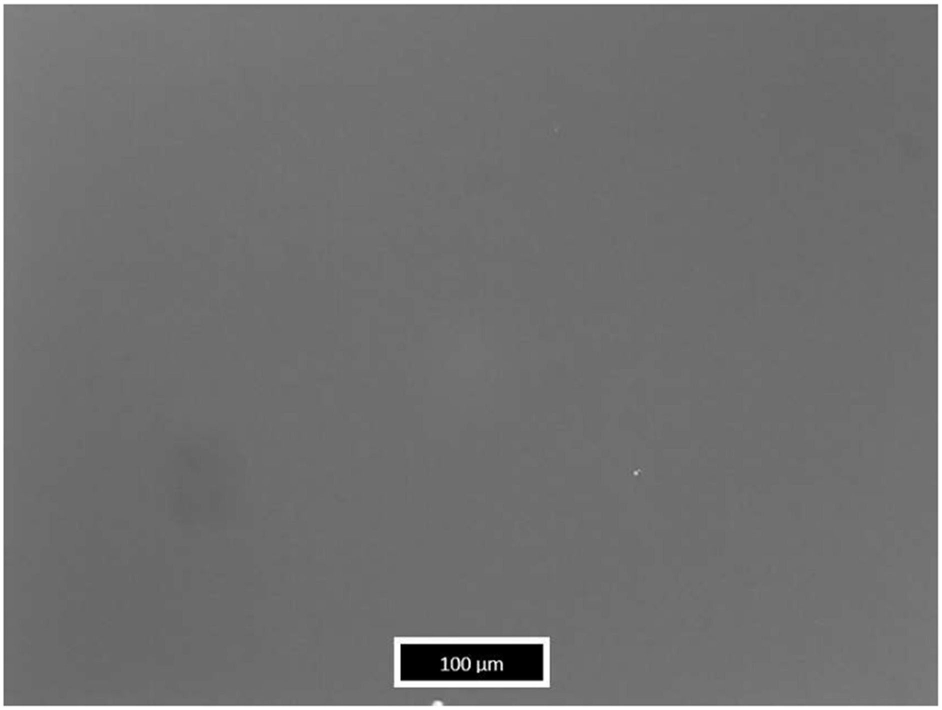

FIGURE 4.8: Nomarski image of STG-34 (3.25% Bi) at 10x magnification

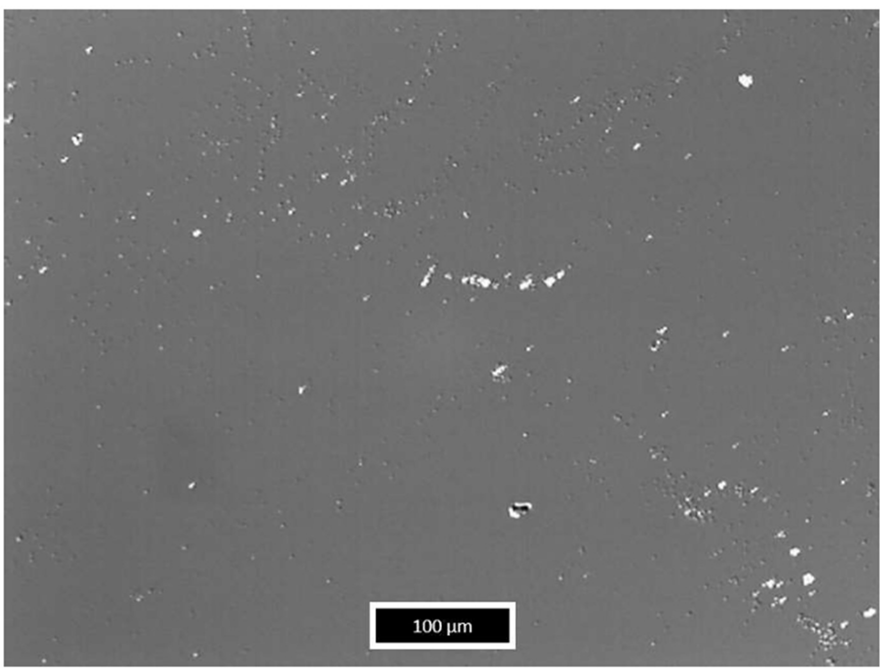

FIGURE 4.9: Nomarski image of STG-3B (4.12% Bi) at 10x magnification

From figures 4.6 to 4.9, the devices show a varying density of droplet-like defects.

Appendix C: The Nomarski Microscopy Images for several GaAsBi MQW p-i-n diodes.

These measurements were conducted by Dr. R.D Richards and reported in

"Molecular beam epitaxy growth and characterization of GaAsBi for photovoltaic applications", Doctoral Thesis University of Sheffield, September 2014

The purpose of this measurement is to observe the presence of defects and detect any strain relaxation on the device layer.

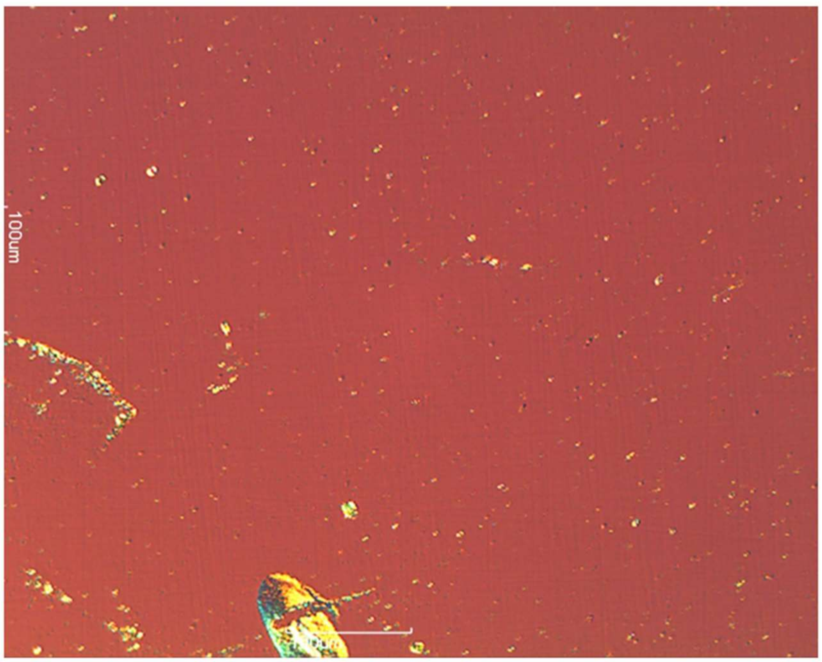

Figure 4.10: Nomarski image of sample 3K (5 wells).

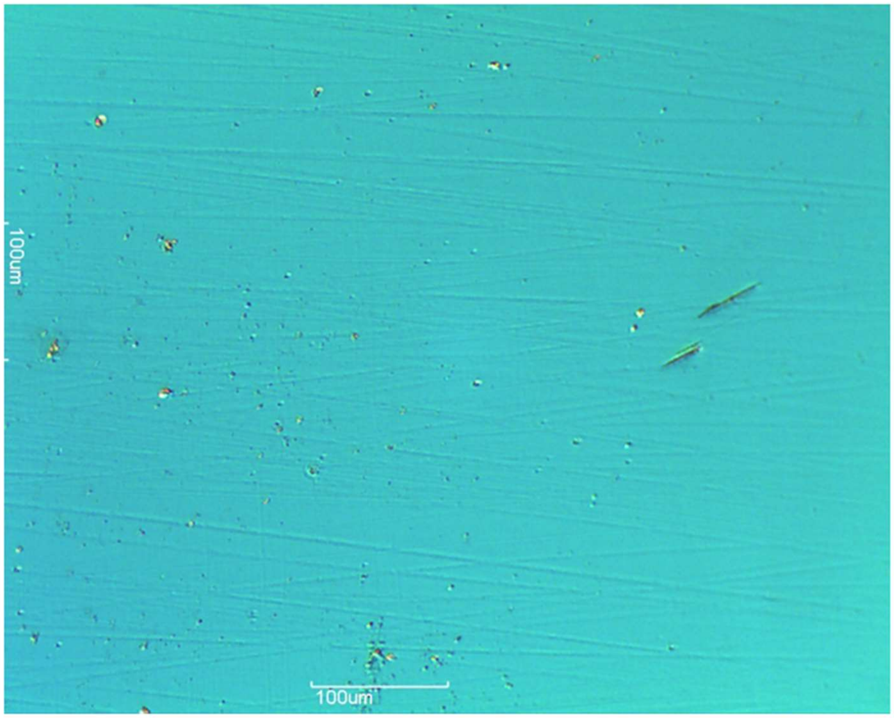

Figure 4.12: Nomarski image of sample 3L (20 wells).

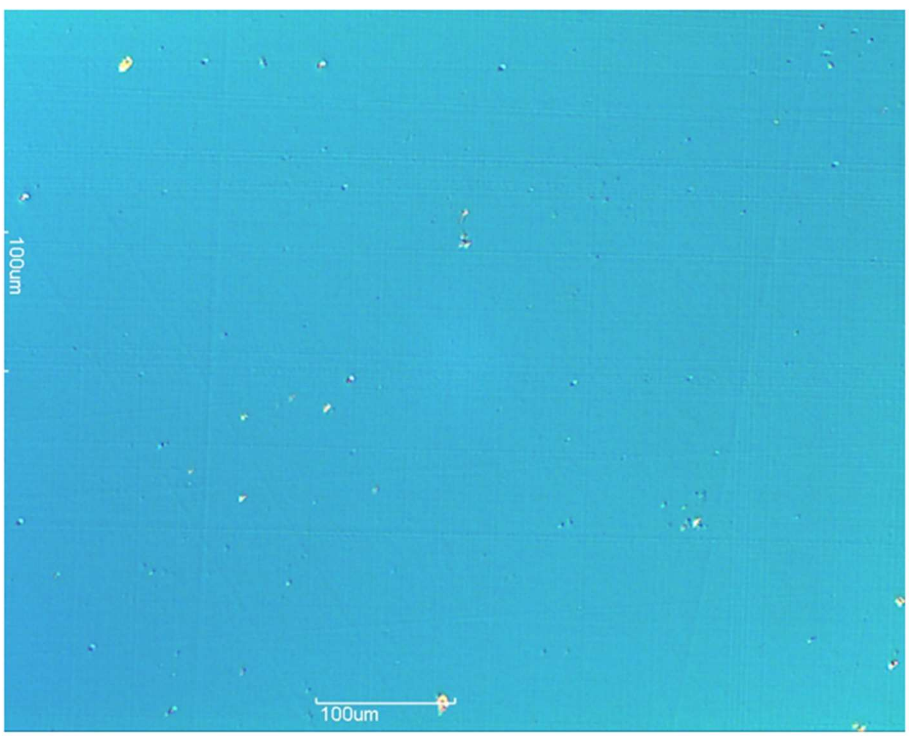

Figure 4.13: Nomarski image of sample 3N (40 wells).

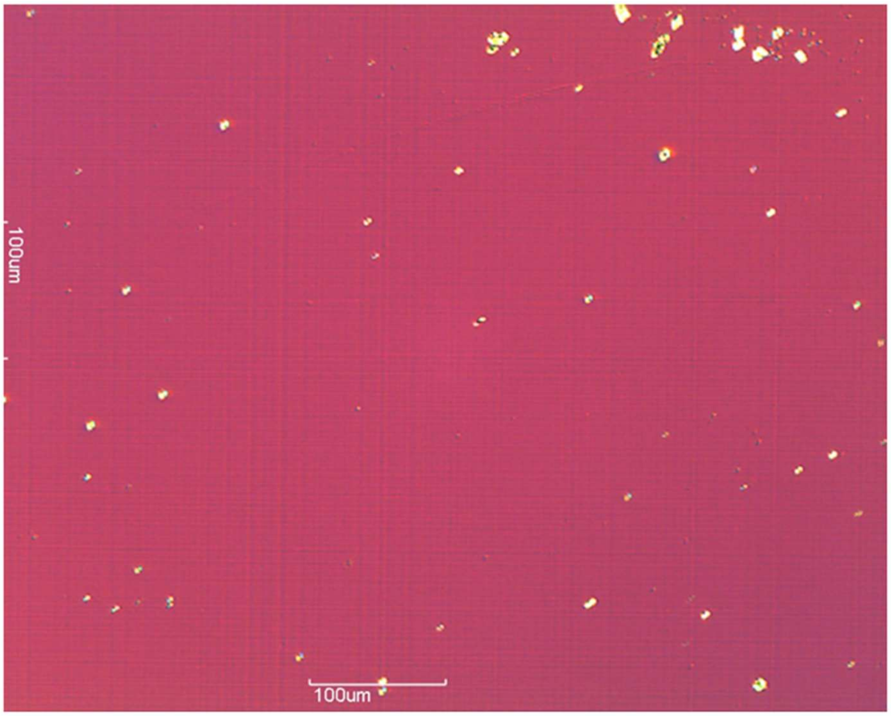

Figure 4.14: Nomarski image of sample 3O (54 wells).

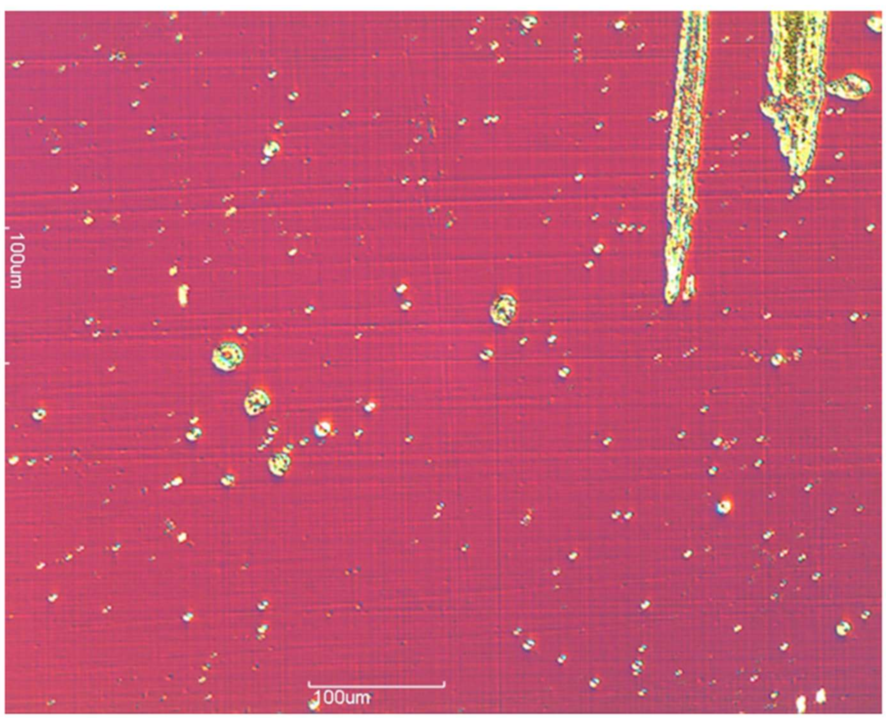

Figure 4.15: Nomarski image of sample 3R (63 wells).

Appendix D: Dark Current Measurement GaAsBi MQW Series at Room Temperature

Dark current measurements for GaAsBi MQW pin diodes at room temperature are shown in Appendix D. These dark currents are only for QW05, QW20, QW40, QW54 and QW63. All measured data are fitted with Shockey diode's equation as described below. Table D shows all the relevant fitting parameters.

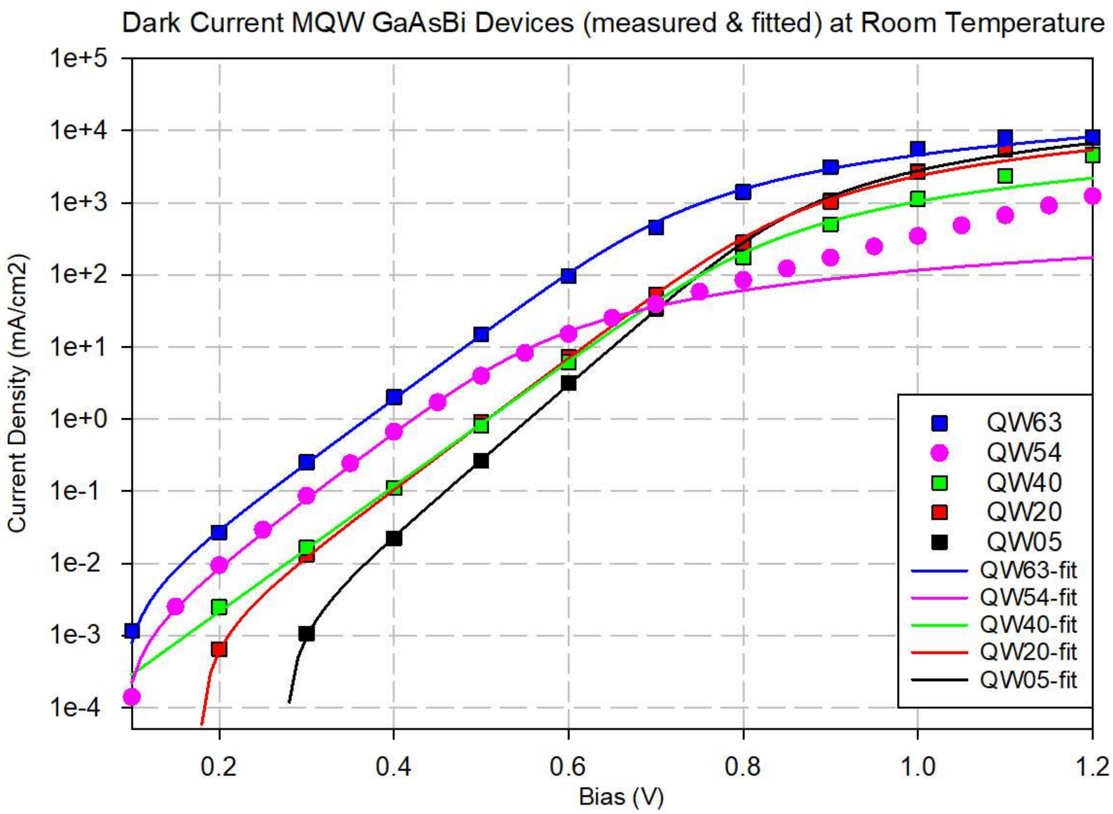

Table D: Dark current density fitting parameters for GaAsBi MQW pin diodes at room temperature.

MQW	J0 (mAcm-2)	n	Rs (Ohm.cm2)	Rsh (Ohm.cm2)
QW05	1.60E-06	1.65	4.19E-05	Large
QW20	2.40E-05	1.89	5.26E-05	Large
QW40	3.87E-05	1.98	1.41E-04	Large
QW54	1.30E-04	1.85	3.11E-03	Large
QW63	5.21E-04	1.93	4.82E-05	Large

Appendix E: The Transmission electron microscopy (TEM) Images for several GaAsBi MQW p-i-n diodes.

These TEM images measurements were conducted by Dr. Richard Beanland at warwick University and the results are reported by Dr. R.D Richards in

"Molecular beam epitaxy growth and characterization of GaAsBi for photovoltaic applications", Doctoral Thesis University of Sheffield, September 2014

Overall, the findings from TEM images indicate that the initial well layer thickness in every sample differs from the subsequent well layers. To address this inconsistency, a Bismide pre-layer implemented on the surface before growth could mitigate this dissimilarity in the thickness layer. The first well layer for most samples is consistently thicker than the following well layers. However, a peculiar condition is found in TEM images on sample QW63, where the first layer is thinner than the following well layer. The author attributes this anomaly in sample QW63 to potential issues with sample quality affecting TEM measurements. Alternatively, it is speculated that at higher numbers of quantum wells, the thin barrier may fail to efficiently eliminate excess Bismide elements from the surface, resulting in a potential Bismide layer forming at the beginning of the subsequent well layer.

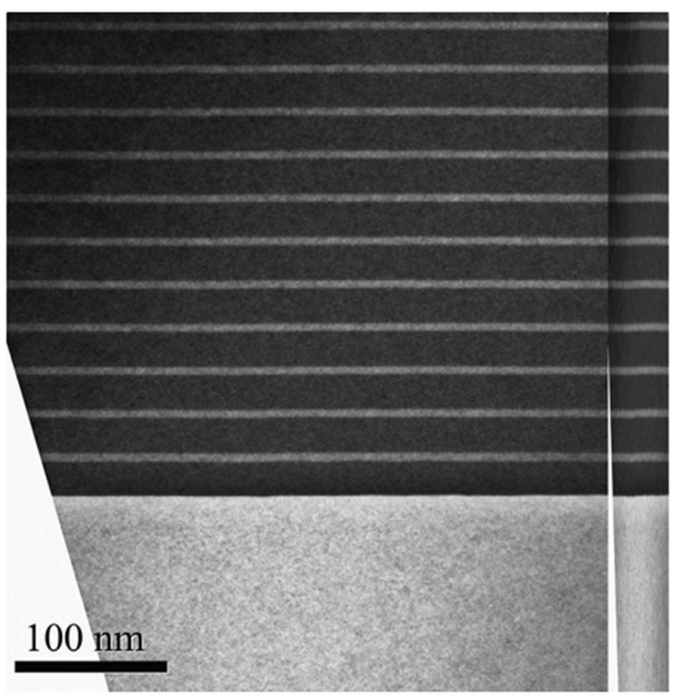

Fig. 5. Dark field TEM image of QW20.

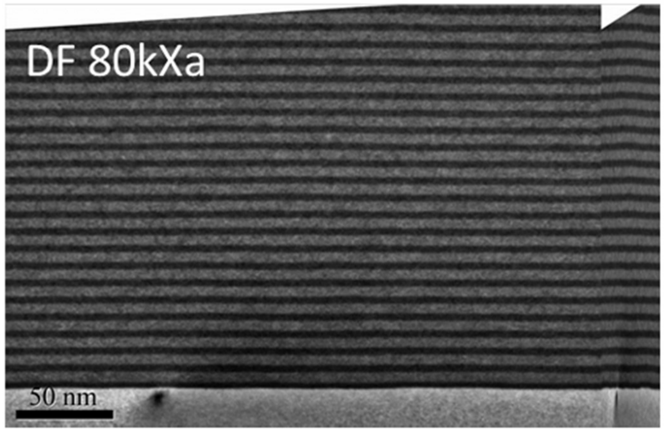
DF 80kXa
50 nm

Appendix E: Photocurrent for GaAsBi Devices at different temperature.

i. QW05

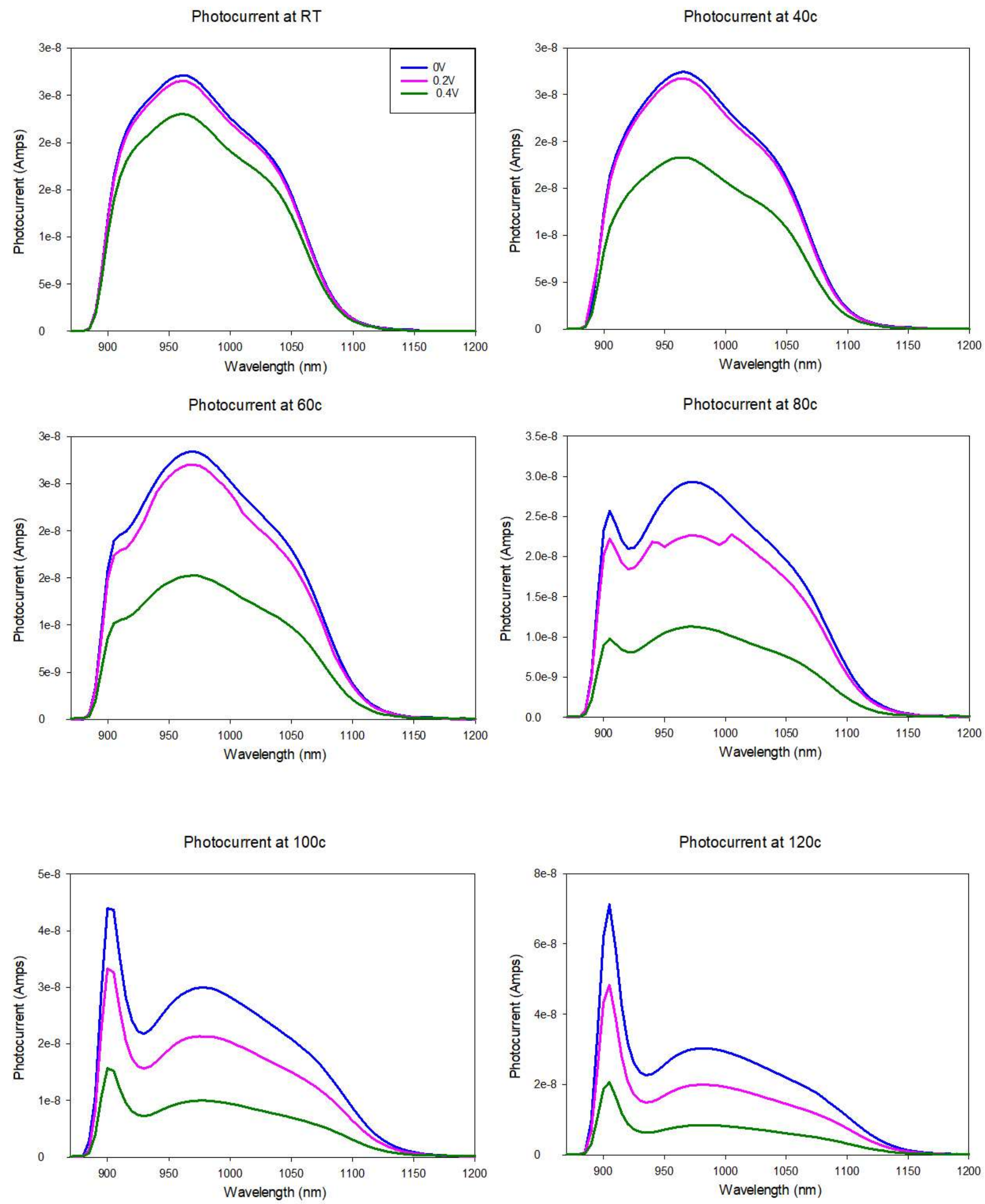

ii. QW20

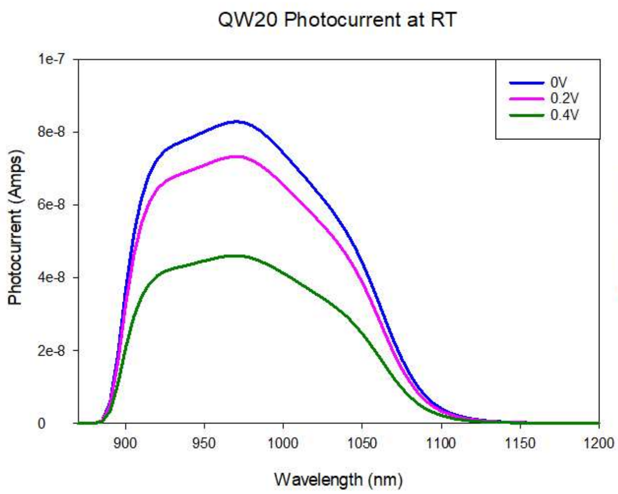
QW20 Photocurrent at RT
0V
0.2V
0.4V
Photocurrent (Amps)
1e-7
8e-8
6e-8
4e-8
2e-8
0
900 950 1000 1050 1100 1150 1200
Wavelength (nm)

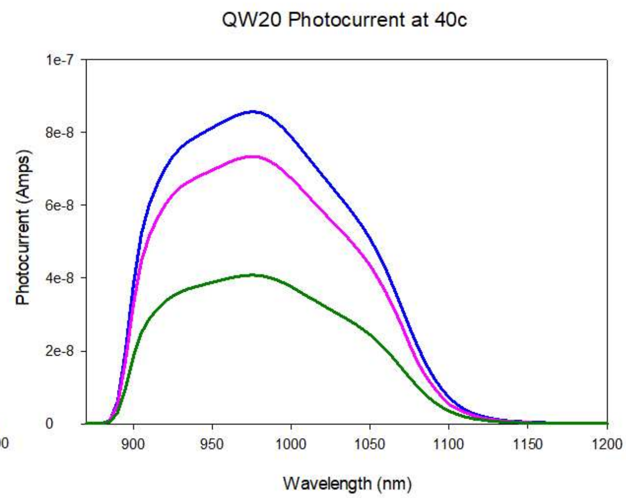
QW20 Photocurrent at 40c
Photocurrent (Amps)
1e-7
8e-8
6e-8
4e-8
2e-8
0
900 950 1000 1050 1100 1150 1200
Wavelength (nm)

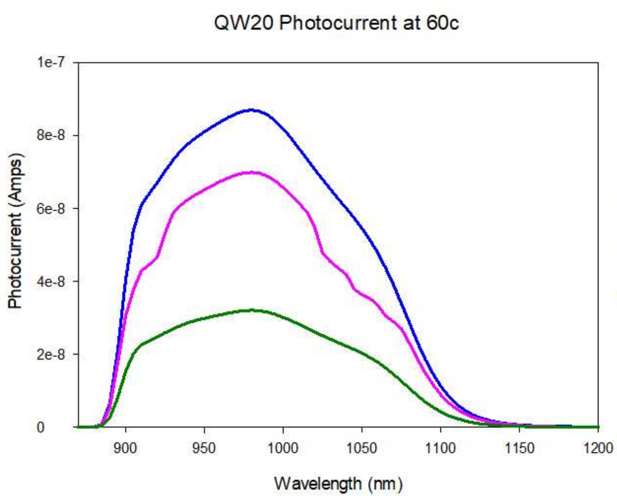
QW20 Photocurrent at 60c
Photocurrent (Amps)
1e-7
8e-8
6e-8
4e-8
2e-8
0
900 950 1000 1050 1100 1150 1200
Wavelength (nm)

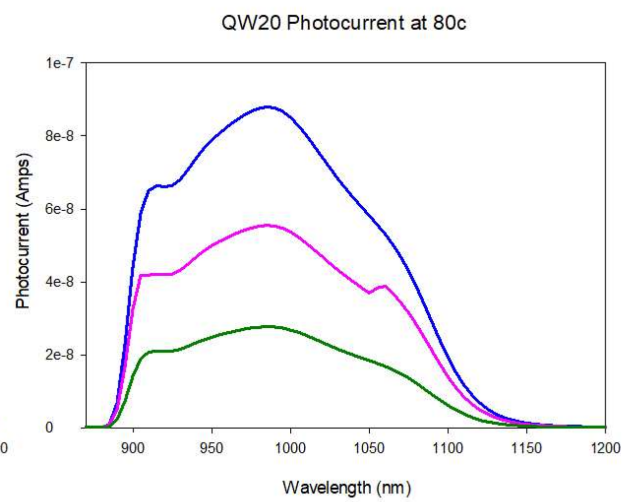
QW20 Photocurrent at 80c
Photocurrent (Amps)
1e-7
8e-8
6e-8
4e-8
2e-8
0
900 950 1000 1050 1100 1150 1200
Wavelength (nm)

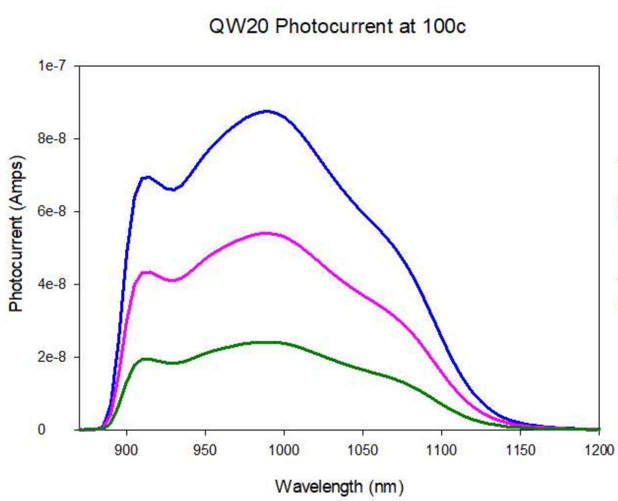
QW20 Photocurrent at 100c
Photocurrent (Amps)
1e-7
8e-8
6e-8
4e-8
2e-8
0
900 950 1000 1050 1100 1150 1200
Wavelength (nm)

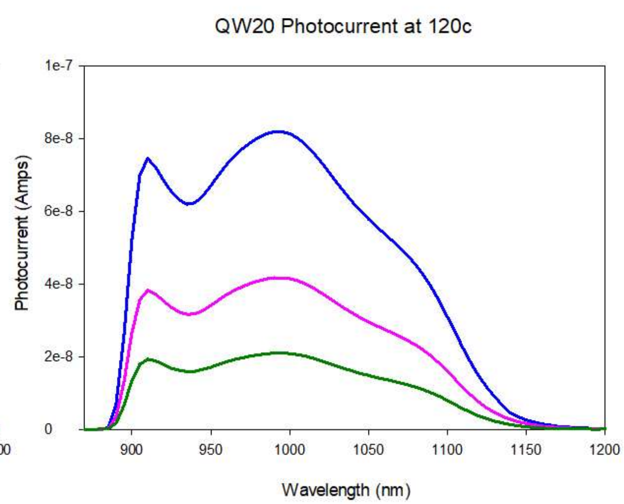
QW20 Photocurrent at 120c
Photocurrent (Amps)
1e-7
8e-8
6e-8
4e-8
2e-8
0
900 950 1000 1050 1100 1150 1200
Wavelength (nm)

iii. QW40

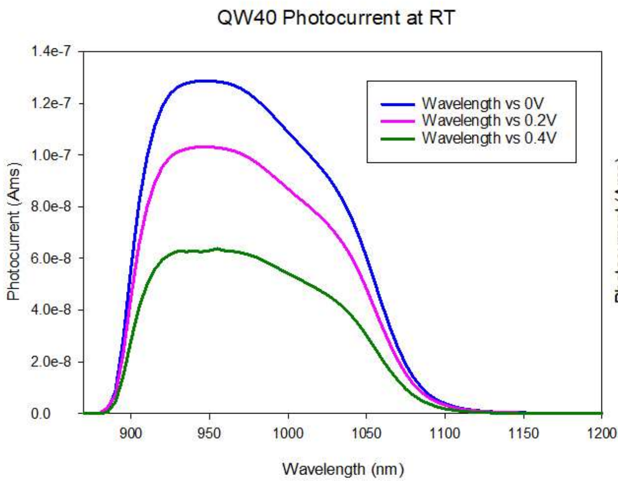
QW40 Photocurrent at RT
Wavelength vs 0V
Wavelength vs 0.2V
Wavelength vs 0.4V
Photocurrent (Ams)
Wavelength (nm)

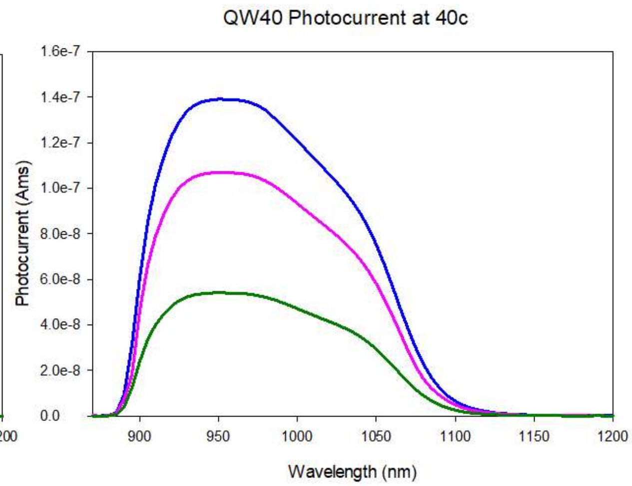
QW40 Photocurrent at 40c
Photocurrent (Ams)
Wavelength (nm)

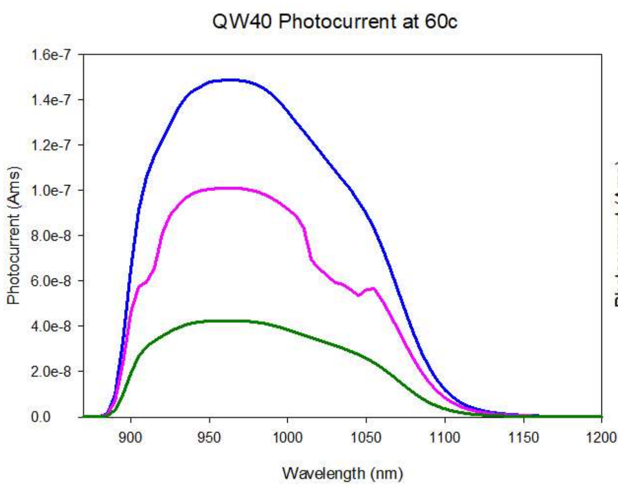
QW40 Photocurrent at 60c
Photocurrent (Ams)
Wavelength (nm)

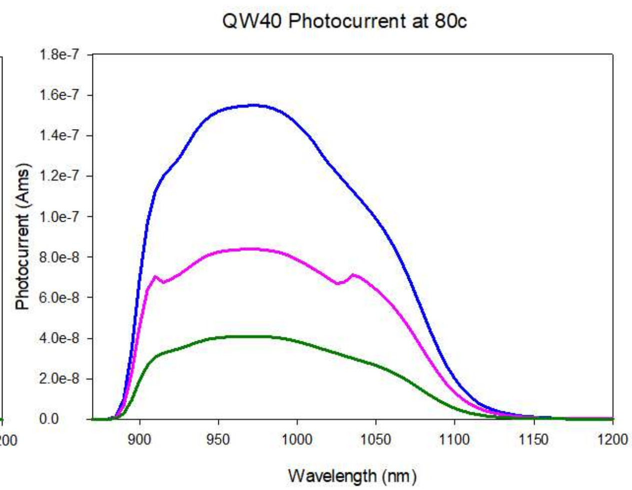
QW40 Photocurrent at 80c
Photocurrent (Ams)
Wavelength (nm)

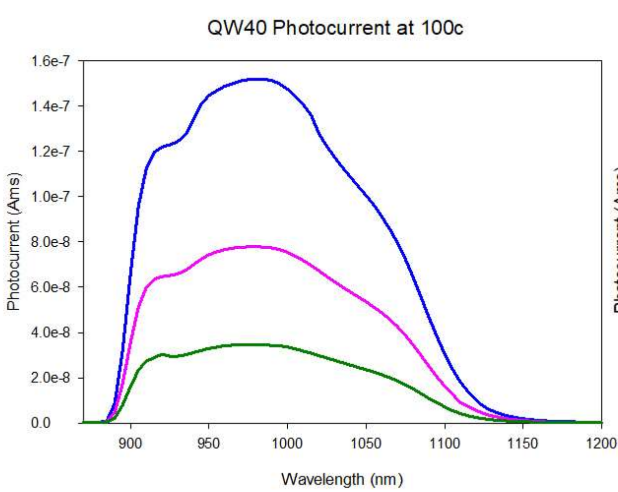
QW40 Photocurrent at 100c
Photocurrent (Ams)
Wavelength (nm)

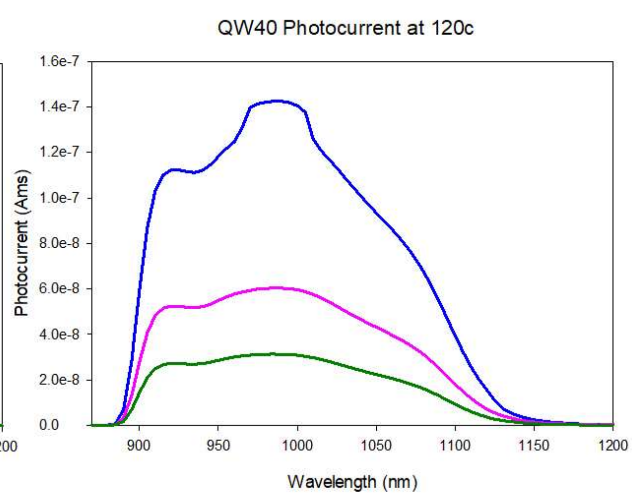
QW40 Photocurrent at 120c
Photocurrent (Ams)
Wavelength (nm)

iv. QW63

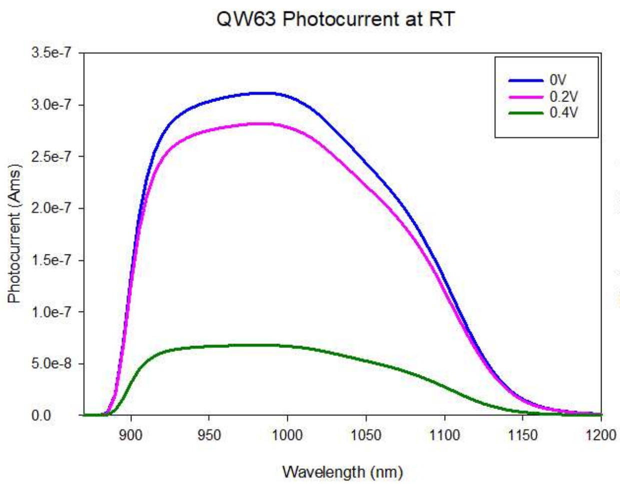
QW63 Photocurrent at RT
0V
0.2V
0.4V
Photocurrent (Ams)
Wavelength (nm)

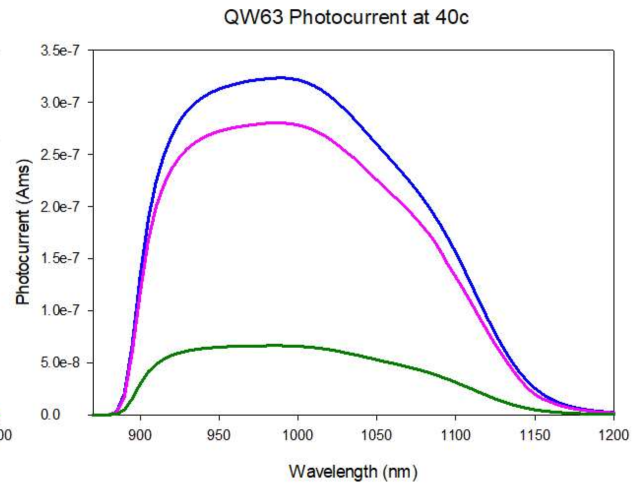
QW63 Photocurrent at 40c
Photocurrent (Ams)
Wavelength (nm)

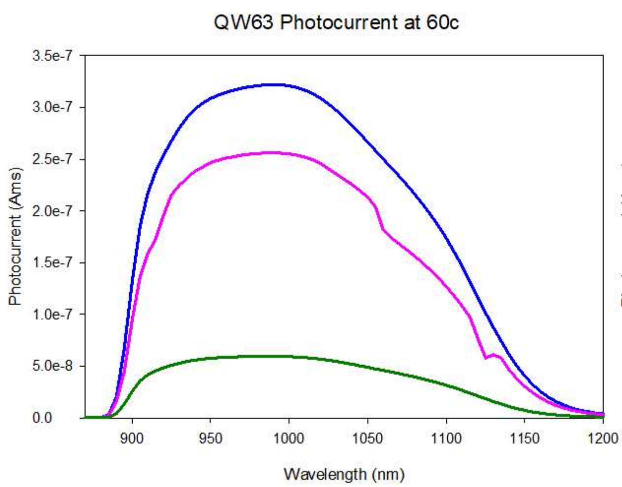
QW63 Photocurrent at 60c
Photocurrent (Ams)
Wavelength (nm)

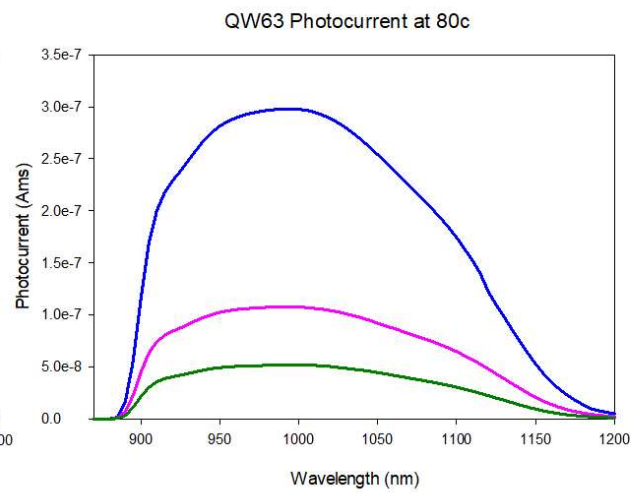
QW63 Photocurrent at 80c
Photocurrent (Ams)
Wavelength (nm)

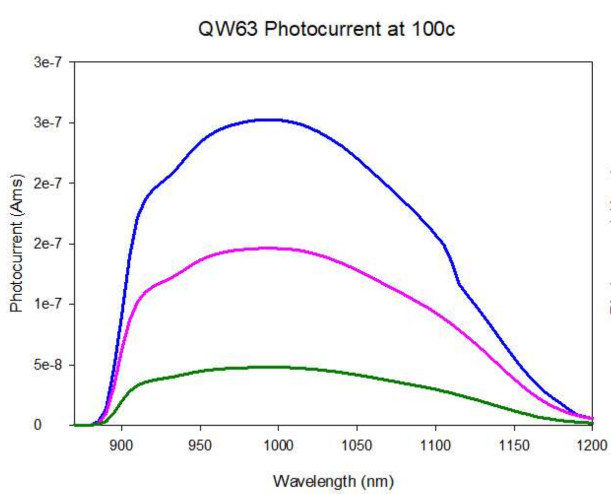
QW63 Photocurrent at 100c
Photocurrent (Ams)
Wavelength (nm)

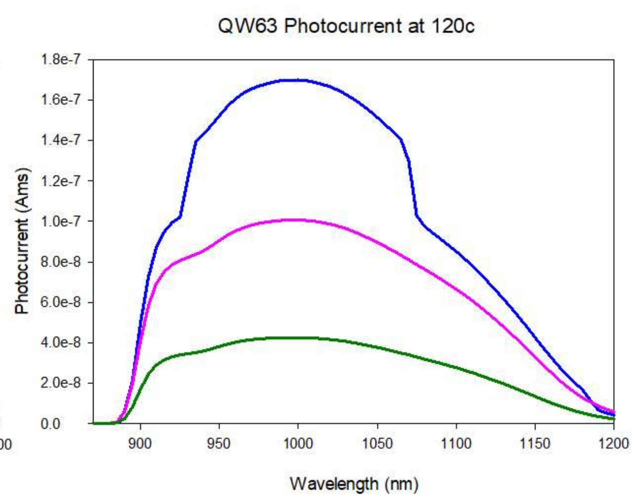
QW63 Photocurrent at 120c
Photocurrent (Ams)
Wavelength (nm)

v. QT1879

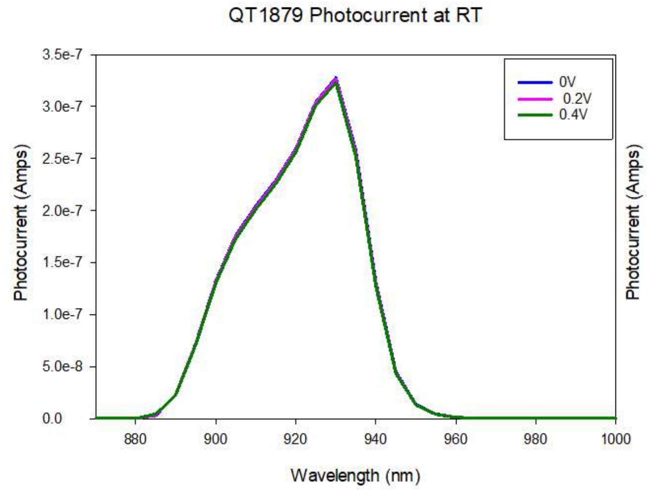
QT1879 Photocurrent at RT
Photocurrent (Amps)
Wavelength (nm)
0V
0.2V
0.4V
3.5e-7 3.0e-7 2.5e-7 2.0e-7 1.5e-7 1.0e-7 5.0e-8 0.0
880 900 920 940 960 980 1000

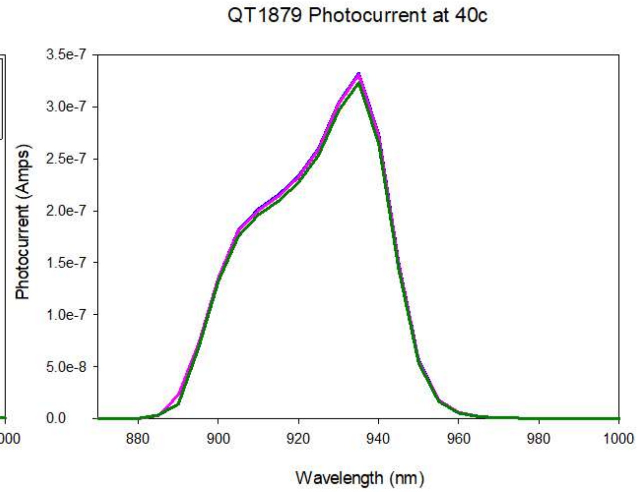
QT1879 Photocurrent at 40c
Photocurrent (Amps)
Wavelength (nm)
3.5e-7 3.0e-7 2.5e-7 2.0e-7 1.5e-7 1.0e-7 5.0e-8 0.0
880 900 920 940 960 980 1000

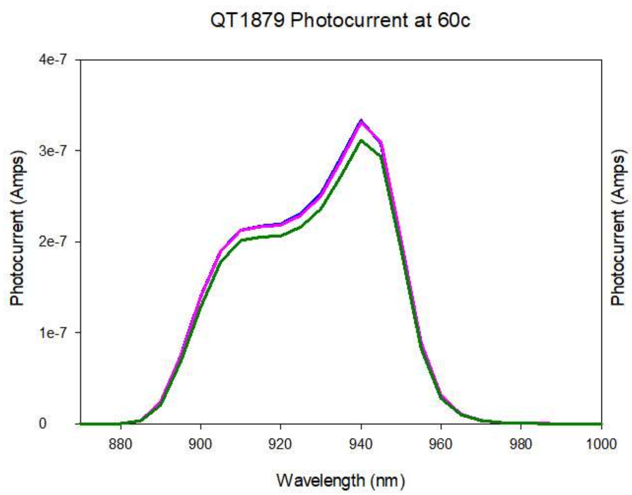
QT1879 Photocurrent at 60c
Photocurrent (Amps)
Wavelength (nm)
4e-7 3e-7 2e-7 1e-7 0
880 900 920 940 960 980 1000

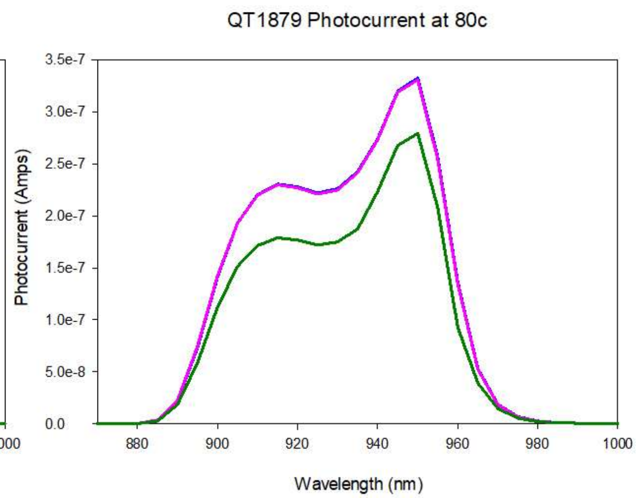
QT1879 Photocurrent at 80c
Photocurrent (Amps)
Wavelength (nm)
3.5e-7 3.0e-7 2.5e-7 2.0e-7 1.5e-7 1.0e-7 5.0e-8 0.0
880 900 920 940 960 980 1000

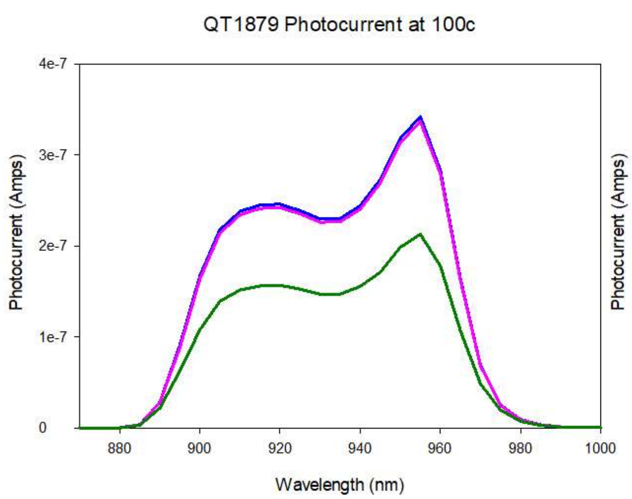
QT1879 Photocurrent at 100c
Photocurrent (Amps)
Wavelength (nm)
4e-7 3e-7 2e-7 1e-7 0
880 900 920 940 960 980 1000

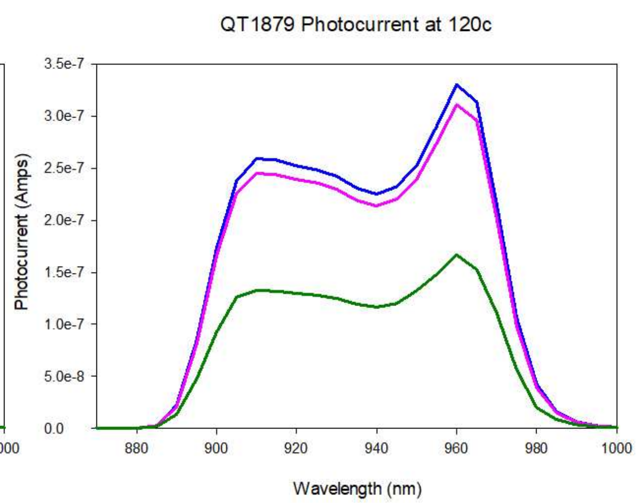
QT1879 Photocurrent at 120c
Photocurrent (Amps)
Wavelength (nm)
3.5e-7 3.0e-7 2.5e-7 2.0e-7 1.5e-7 1.0e-7 5.0e-8 0.0
880 900 920 940 960 980 1000

Appendix F: EQE for GaAsBi Devices at different temperature.

i. QW05

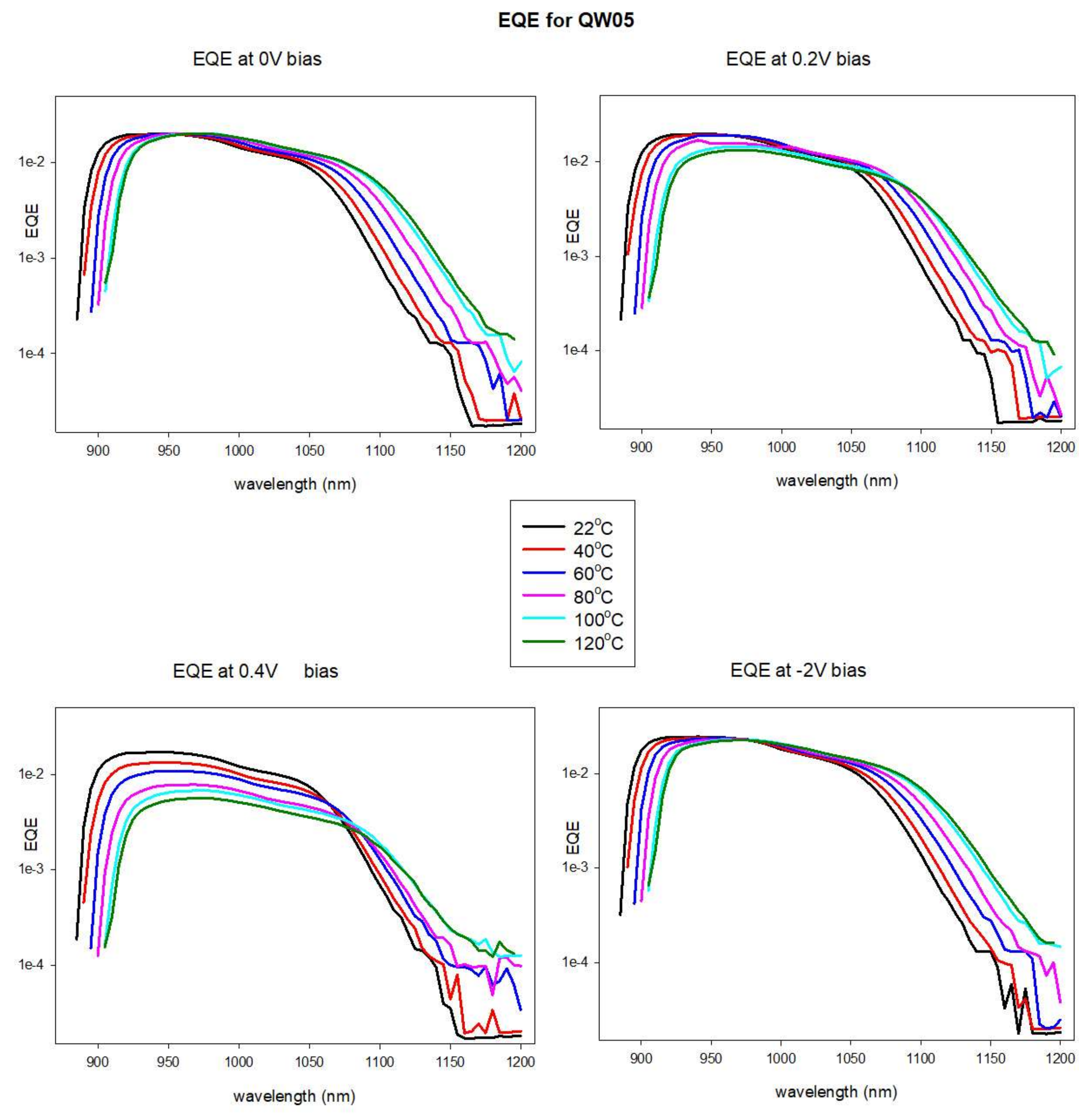

ii. QW20

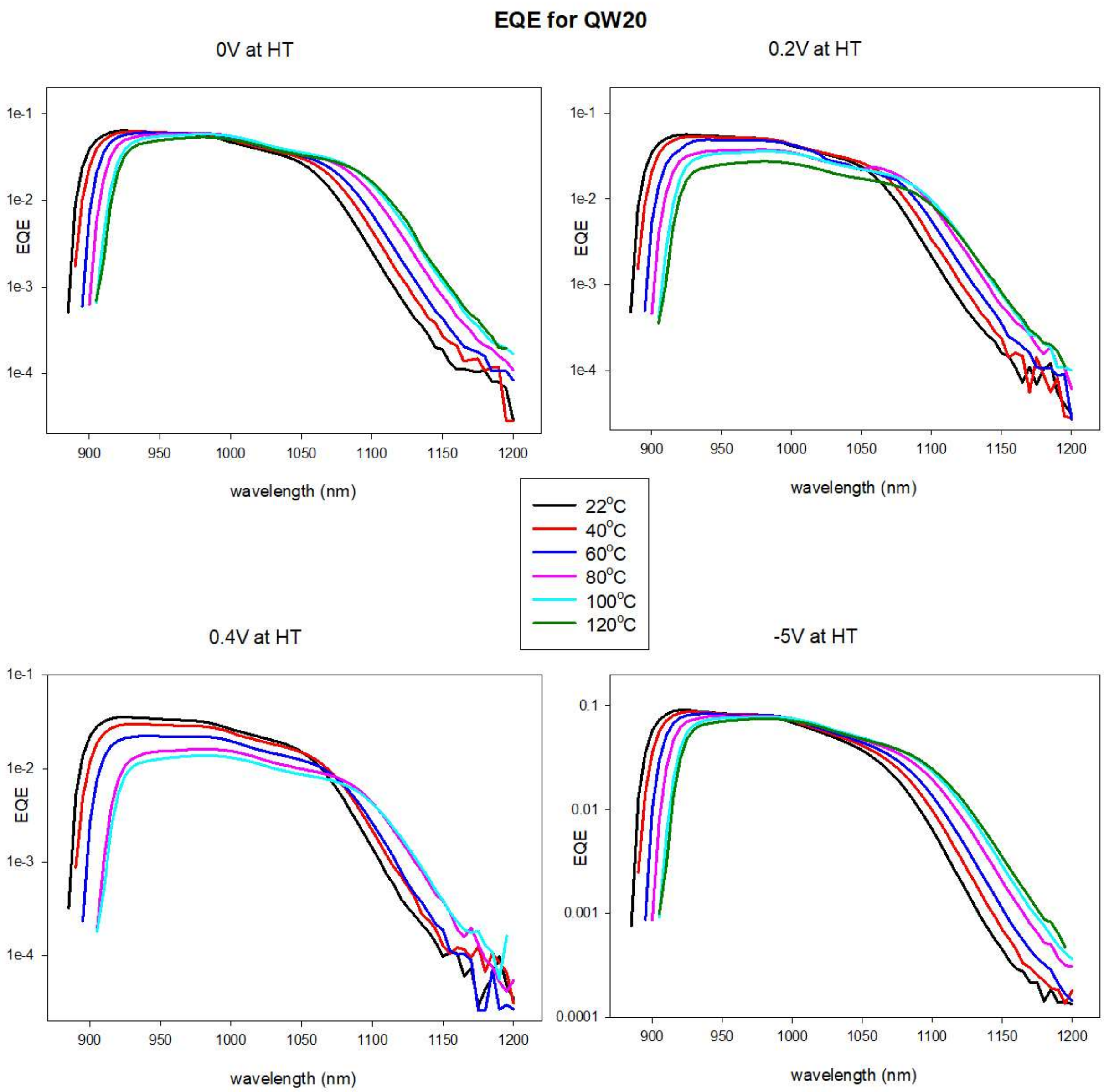

EQE for QW20
0V at HT
0.2V at HT
0.4V at HT
-5V at HT
EQE
wavelength (nm)
22°C
40°C
60°C
80°C
100°C
120°C

iii. QW40

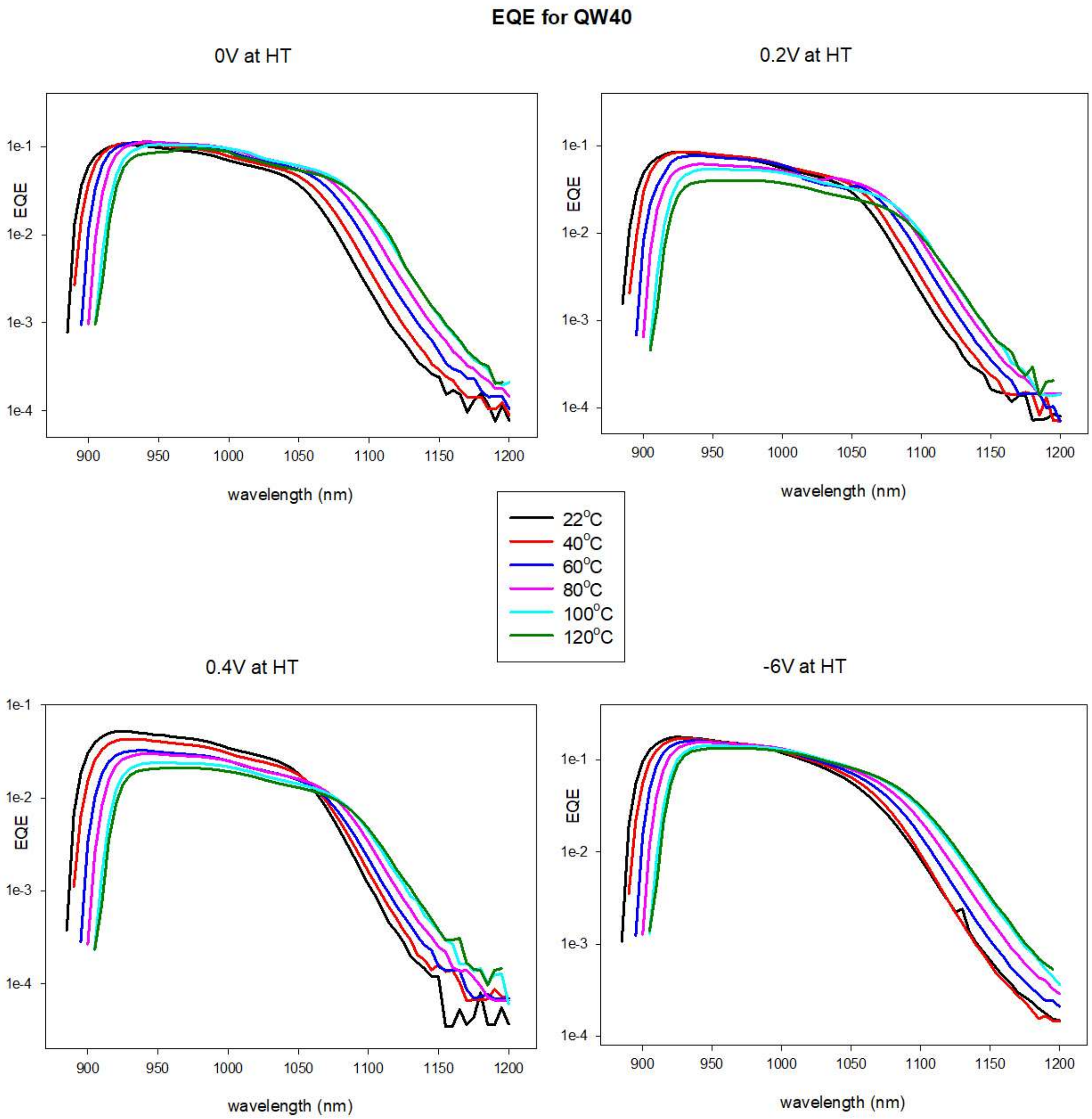

EQE for QW40
0V at HT
0.2V at HT
0.4V at HT
-6V at HT
EQE
1e-1
1e-2
1e-3
1e-4
900
950
1000
1050
1100
1150
1200
wavelength (nm)
22°C
40°C
60°C
80°C
100°C
120°C

iv. QW63

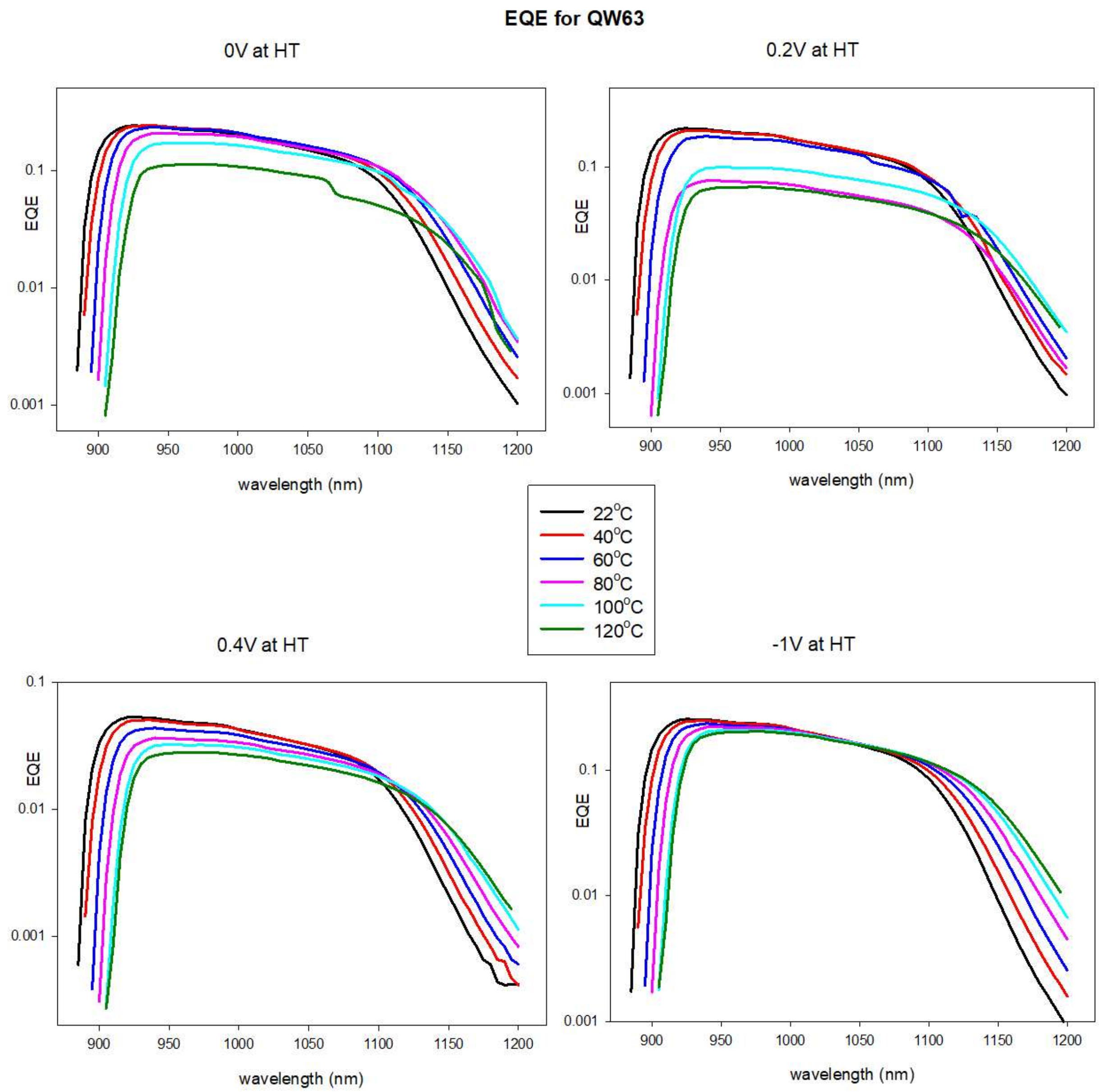

EQE for QW63
0V at HT
0.2V at HT
0.4V at HT
-1V at HT
EQE
wavelength (nm)
0.1
0.01
0.001
900
950
1000
1050
1100
1150
1200
22°C
40°C
60°C
80°C
100°C
120°C

v. **QT1879**

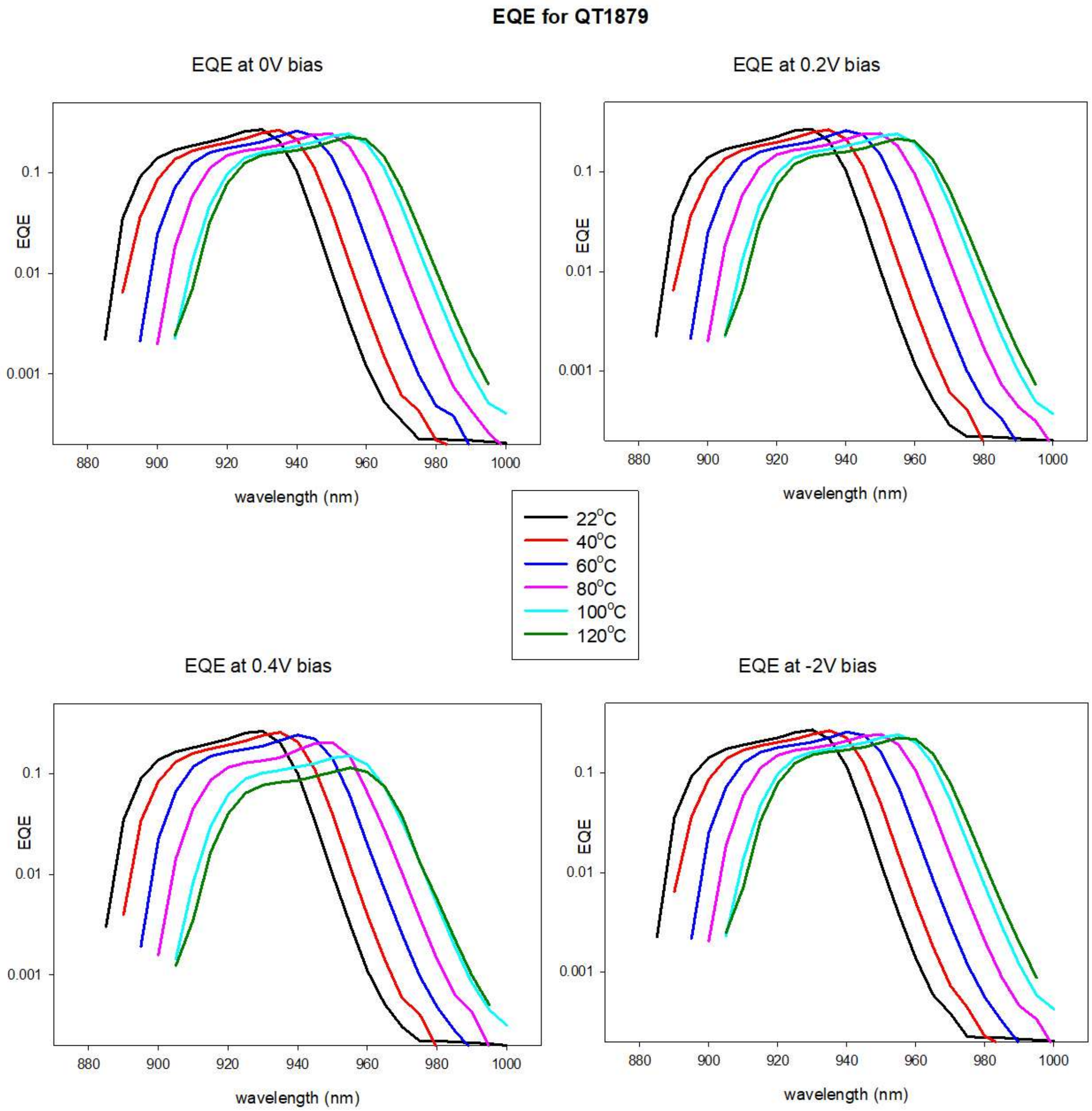
EQE for QT1879
EQE at 0V bias
EQE at 0.2V bias
EQE at 0.4V bias
EQE at -2V bias
EQE
0.1
0.01
0.001
880
900
920
940
960
980
1000
wavelength (nm)
22°C
40°C
60°C
80°C
100°C
120°C

Appendix F: The current-voltage and power-voltage characteristics for GaAsBi Devices at different temperature.

i. QW05

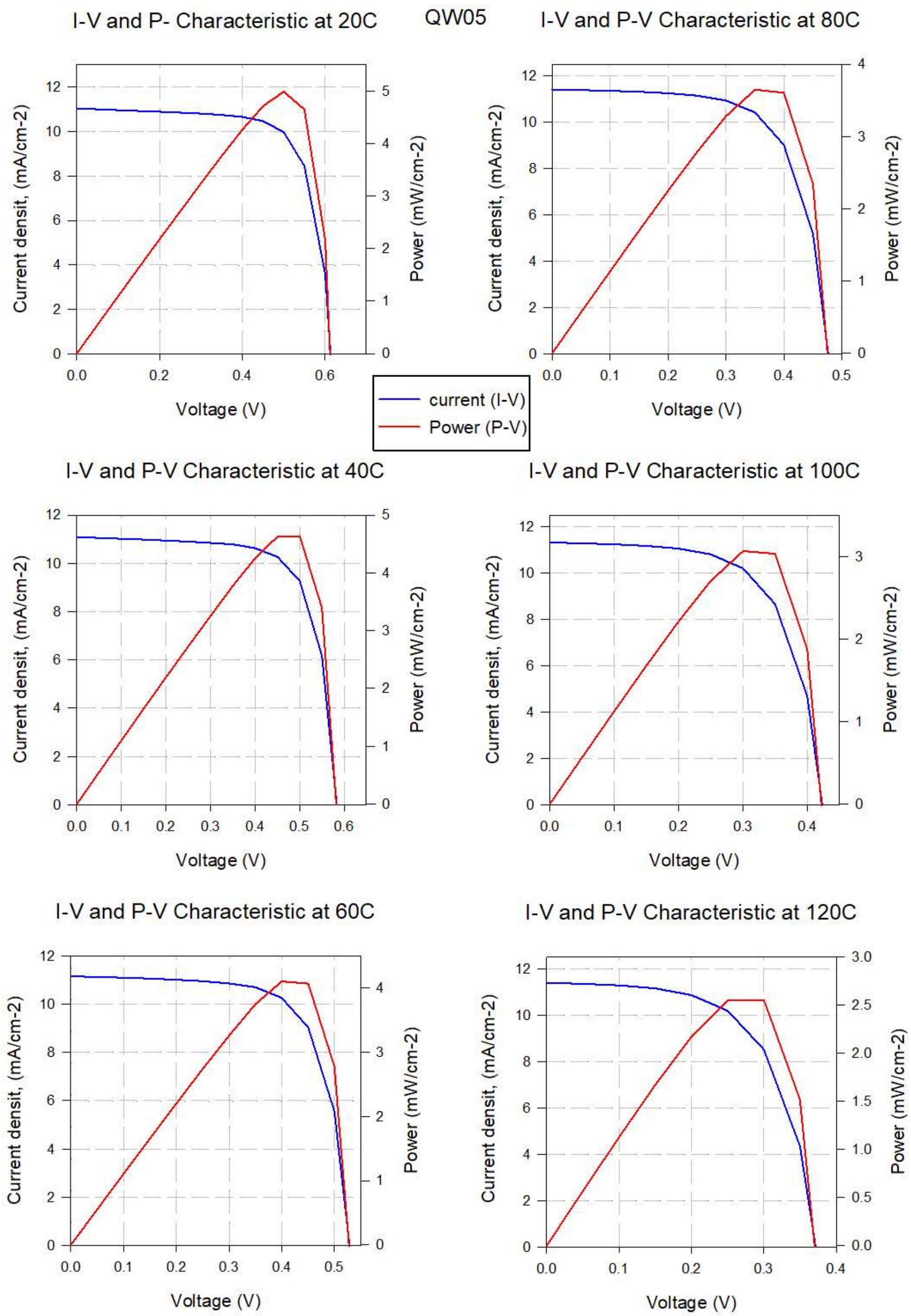

ii. QW20

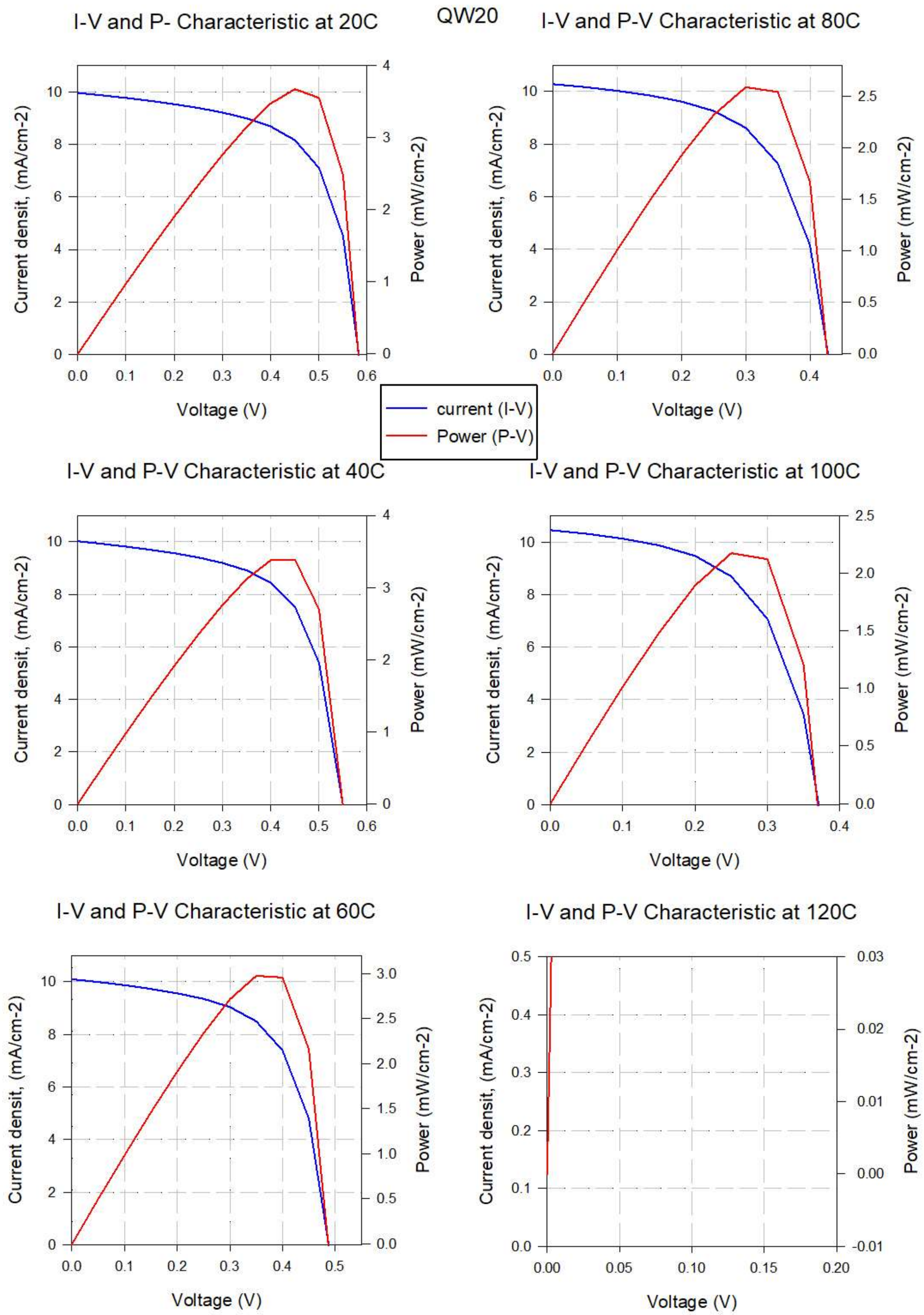
QW20
I-V and P- Characteristic at 20C
I-V and P-V Characteristic at 80C
I-V and P-V Characteristic at 40C
I-V and P-V Characteristic at 100C
I-V and P-V Characteristic at 60C
I-V and P-V Characteristic at 120C
Current densit, (mA/cm-2)
Power (mW/cm-2)
Voltage (V)
current (I-V)
Power (P-V)

iii. QW40

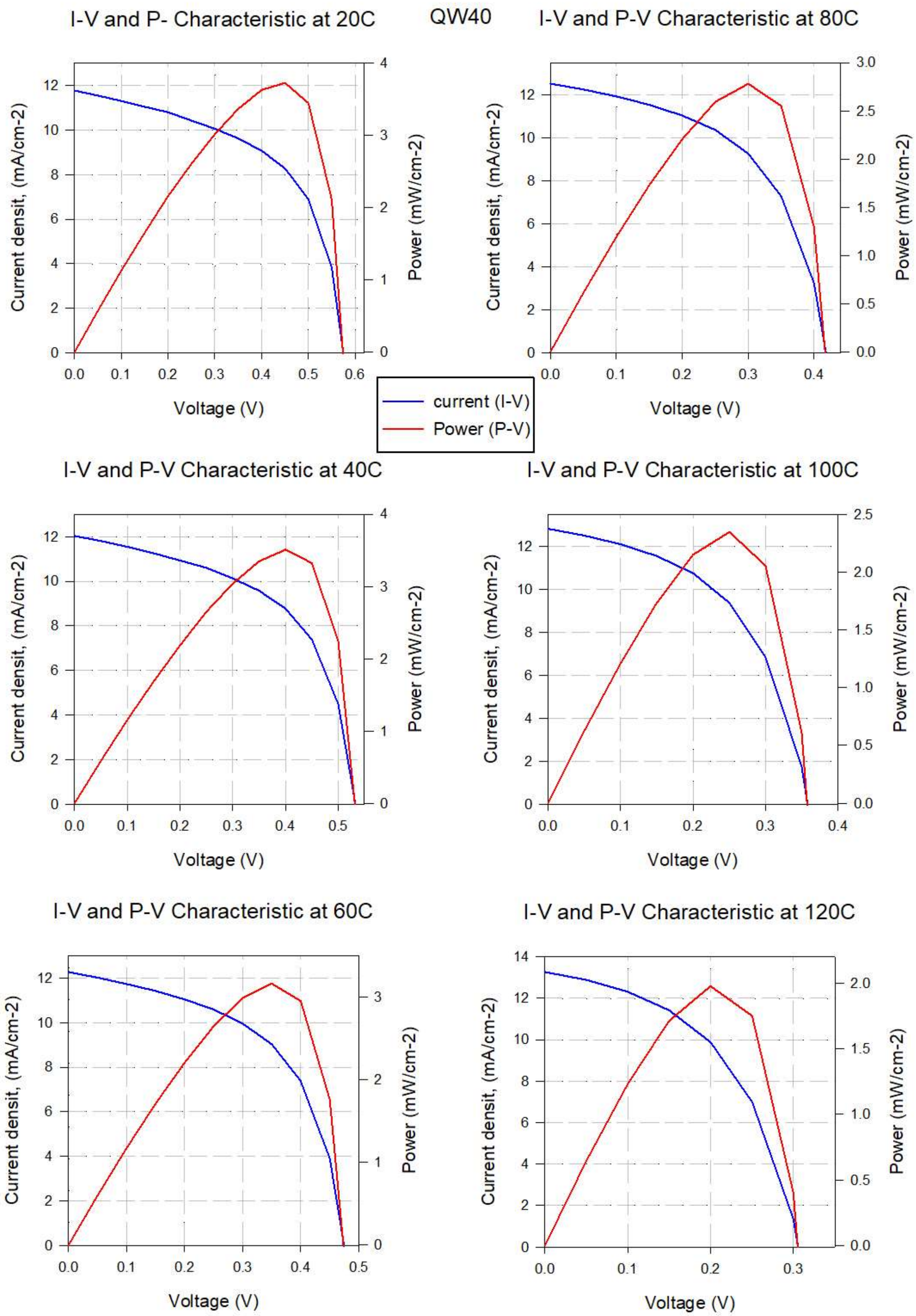

I-V and P- Characteristic at 20C
QW40
I-V and P-V Characteristic at 80C
I-V and P-V Characteristic at 40C
I-V and P-V Characteristic at 100C
I-V and P-V Characteristic at 60C
I-V and P-V Characteristic at 120C
Current densit, (mA/cm-2)
Power (mW/cm-2)
Voltage (V)
current (I-V)
Power (P-V)

iv. QW63

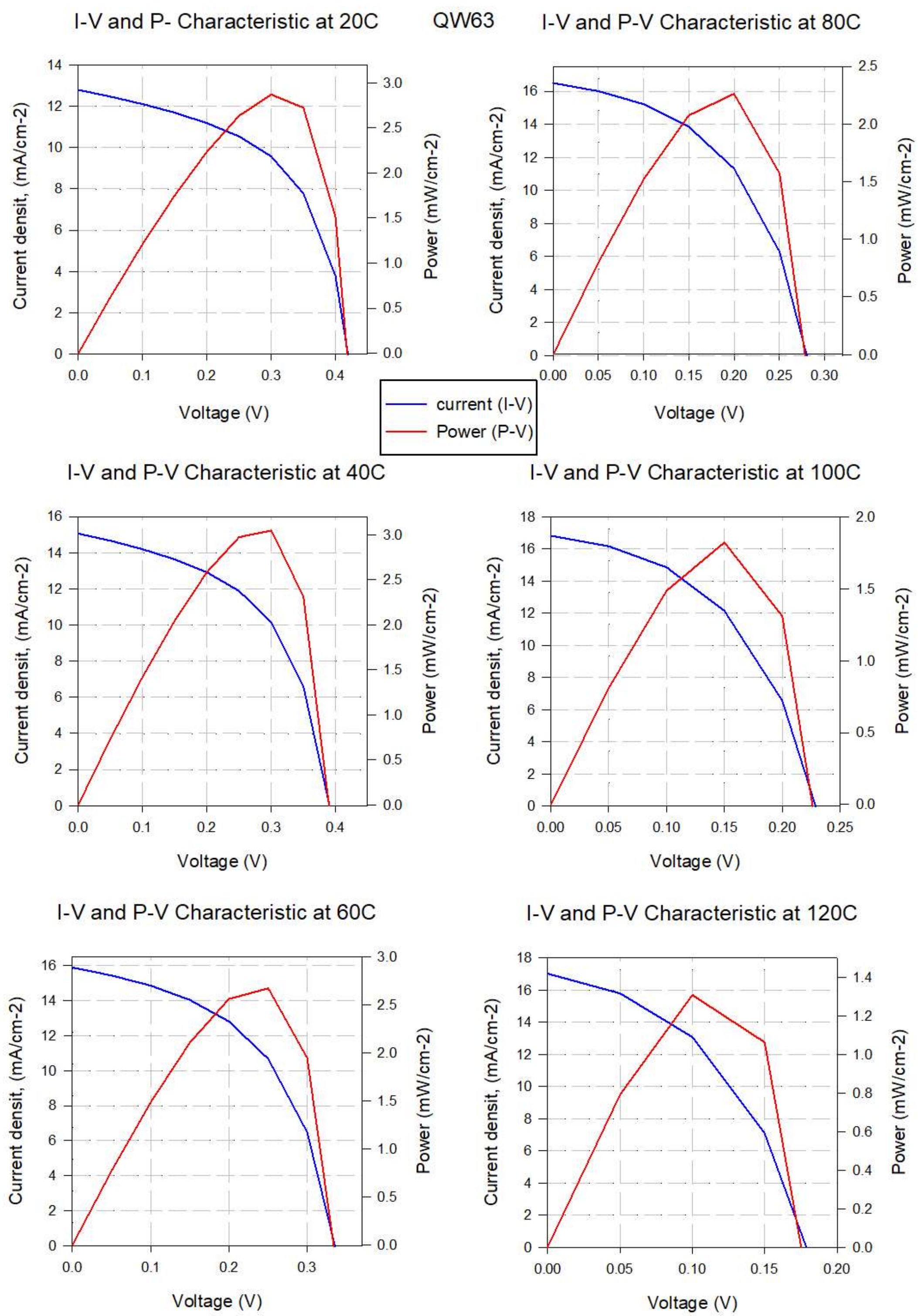

QW63
I-V and P- Characteristic at 20C
I-V and P-V Characteristic at 80C
I-V and P-V Characteristic at 40C
I-V and P-V Characteristic at 100C
I-V and P-V Characteristic at 60C
I-V and P-V Characteristic at 120C
Current densit, (mA/cm-2)
Power (mW/cm-2)
Voltage (V)
current (I-V)
Power (P-V)

v. QT1879

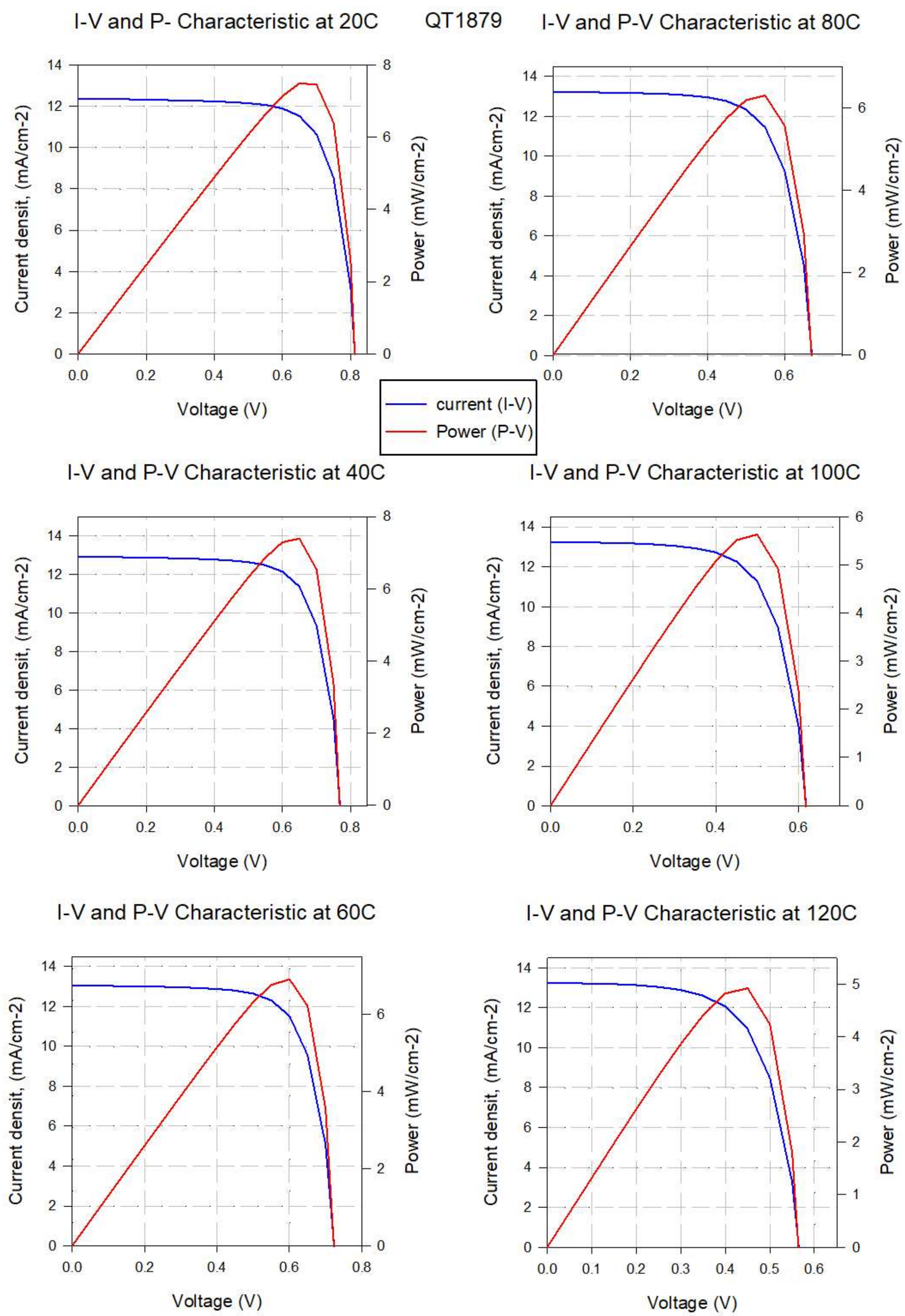

I-V and P- Characteristic at 20C
QT1879
I-V and P-V Characteristic at 80C
I-V and P-V Characteristic at 40C
I-V and P-V Characteristic at 100C
I-V and P-V Characteristic at 60C
I-V and P-V Characteristic at 120C
Current densit, (mA/cm-2)
Power (mW/cm-2)
Voltage (V)
current (I-V)
Power (P-V)